

OBSERVATIONS OF OSCILLATORY MOTIONS  
IN THE SOLAR ATMOSPHERE

Thesis by  
Robert Wilson Noyes

In Partial Fulfillment of the Requirements  
For the Degree of  
Doctor of Philosophy

California Institute of Technology  
Pasadena, California

1963

## ABSTRACT

This thesis presents observations of the macroscopic line-of-sight velocity field in the solar atmosphere. The observations were made at Mt. Wilson Observatory, primarily in 1960 and 1961. A quasi-periodic vertical oscillatory motion has been detected in the upper photosphere and low chromosphere. The "average period" of this oscillation has been determined with some accuracy to be about 300 sec.; there appears to be a slight decrease of period with increasing altitude. The mean life of a single oscillation is about 400 sec. The "velocity elements" which partake of the oscillation have an appearance very similar to the photospheric granulation of low levels, and are probably identical to it. The vertical velocity amplitude is about  $1/2$  km/sec at these levels, and increases with altitude. The horizontal component of velocity is nearly as large as the vertical at low levels, but decreases with altitude, until at higher levels the velocities are substantially vertical only. The mean diameter of the velocity elements is only slightly larger than the photospheric granulation at low levels, but increases to many times that size at higher levels.

We also report in this thesis on observations of macroscopic intensity fields, made concurrently with the velocity observations. A

correlation coefficient between intensity and velocity has been found which appears to decrease monotonically with altitude, from about +0.5 at the lowest elevations observed to about -0.2 at the highest observed elevations. An oscillatory behavior of the intensity field is found in the chromosphere, with roughly the same period as the velocity oscillation, and evidently coupled to it. This oscillation may be followed to considerable altitudes in the chromosphere. It is apparently absent in the upper photosphere, however, even though the velocity oscillation is quite strong there.

Also discussed are some possible interpretations of the observations and what they might imply about the structure of the solar atmosphere. We find that the observed period is close to the "critical period" separating propagating and standing acoustic waves in a gravitating atmosphere with the solar values for temperature and gravitational field. Several possible explanations for the decrease of period with altitude are suggested. The amplitude and phase of the temperature fluctuations accompanying a wave propagating in an atmosphere with radiative leakage are discussed; this leads to a possible explanation of the presence of an intensity oscillation at high levels and its absence at low levels, and of the reversal with altitude of the sign of the correlation coefficient between intensity and velocity.

Some observational problems are also discussed, both in the body of the thesis (Parts I and II) and in appendices.

## ACKNOWLEDGEMENTS

The author wishes to thank Professor R. B. Leighton, under whose supervision this work was performed, for his constant supply of encouragement and enthusiasm, and for his generous donation of physical and mechanical insight, without which this research would have explored many more blind alleys than it has. In addition, his understanding during some of the more discouraging moments of this research is most gratefully appreciated.

The author also wishes to acknowledge the help, encouragement, and optimism of Mr. George W. Simon in the observational program. His aid in some of the data analysis is also appreciated.

Grateful acknowledgement is made for continued financial and other assistance from the California Institute of Technology, the United States Navy Office of Naval Research, and the Mt. Wilson and Palomar Observatories.

Many of the illustrations used in this thesis were prepared by Professor Leighton for publication in an earlier article (2).

## TABLE OF CONTENTS

	Page
INTRODUCTION . . . . .	1
<b>PART I. THE SPECTROHELIOGRAPH . . . . .</b>	<b>3</b>
A. The Spectroheliograph . . . . .	3
B. Resolution of the Spectroheliograph . . . . .	7
C. Scattered Light . . . . .	11
<b>PART II. METHODS OF OBTAINING, REDUCING, AND ANALYZING DATA . . . . .</b>	<b>14</b>
A. The Collection and Reduction of Data . . . . .	14
B. The Analysis of Data: Autocorrelation and Cross Correlation Functions and their Interpretation . . . . .	20
C. Calibration . . . . .	30
D. Sensitivity and Errors . . . . .	31
<b>PART III. THE OBSERVATIONS . . . . .</b>	<b>37</b>
A. The Instantaneous Velocity Field . . . . .	39
B. Size of the Elements of the Velocity Field . . . . .	45
C. Variation of Line-of-Sight Velocity with Position on the Solar Disk . . . . .	47
D. Oscillatory Motions as Revealed by the Time Dependence of the Velocity Field . . . . .	55
E. Determination of the Average Period of the Oscillation and Its Variation with Altitude . . . . .	57
F. Lifetime of the Oscillation . . . . .	63
G. Relative Sizes of Oscillatory and Non-Oscillatory Components of the Velocity Field . . . . .	65
H. The Brightness-Velocity Correlation . . . . .	66
I. Oscillations in the Chromospheric Brightness Field . . . . .	74
J. Observations of the Phase Relation between the Velocity and Brightness Oscillations . . . . .	80
<b>PART IV. DISCUSSION . . . . .</b>	<b>82</b>
A. Introduction . . . . .	82
B. The Wave Equation . . . . .	85
C. Possible Mechanisms for the Decrease of Average Period of the Velocity Oscillation with Altitude . . . . .	94
D. The Variation of Opacity with Altitude and Its Possible Effects on the Oscillation . . . . .	99
E. The Thermal Properties of the Oscillation . . . . .	107
F. Conclusion . . . . .	116

TABLE OF CONTENTS (continued)	Page
<b>APPENDIX I. RESOLUTION OF THE SPECTROHELIOGRAPH</b>	<b>121</b>
A. Curvature of the Focal Surface of the Spectroheliograph . . . . .	121
B. Resolution Loss Due to Finite Slit Widths . . . . .	122
C. Loss of Resolution Due to the Gap between the Exit Slit of the Spectroheliograph and the Plate . . . . .	128
D. Resolution of the Lenses and Grating . . . . .	130
<b>APPENDIX II. GHOSTS AND SCATTERED LIGHT</b> . . . . .	<b>131</b>
A. Ghosts . . . . .	131
B. Light Scattered Parallel to the Spectrum . . . . .	131
C. Light Scattered Perpendicular to the Spectrum . . . . .	132
<b>APPENDIX III. ERROR ANALYSIS</b> . . . . .	<b>134</b>
A. Sources of Error . . . . .	134
B. Limits of Error . . . . .	144
<b>REFERENCES</b> . . . . .	<b>150</b>

## I. INTRODUCTION

In this thesis we wish to present some results of observations made at Mt. Wilson Observatory during the summers of 1960 and 1961 concerning the macroscopic velocity structure of the line-forming layers of the solar atmosphere .

Although observations of velocity fields in the solar atmosphere are by no means new, the techniques used in this investigation are somewhat novel. These techniques have in turn led to the observation of several new features of the velocity structure of the solar atmosphere. This thesis will treat in detail one aspect of these observations, namely the presence of oscillatory motions in the solar photosphere and low chromosphere, with a strongly predominant period of about five minutes.

The new technique just mentioned was originally developed by R. B. Leighton (1) in order to measure Zeeman splitting of Fraunhofer lines; it is easily adapted to the measurement of Doppler shifts as well. The principle of the method is as follows: two simultaneous spectroheliograms are taken, one on either wing of a spectral line. A Doppler shift of the line causes opposite effects on the intensity of the two images, whereas all other intensity effects are essentially the same on the two images. The difference between the density of the two images, which is obtained by a

photographic subtraction technique, is then proportional to the line-of-sight velocity at each point. In using such a technique, one pays the price of being able to observe Doppler shifts of only one line during each observation, whereas a normal spectrogram records an entire region of the spectrum for each point observed. However, in return one reaps the compensating reward of a two-dimensional picture of the velocity structure over an extended area. Measurements of the statistical properties of such "velocity spectroheliograms" and of the statistical time correlation properties of pairs of such "spectroheliograms," taken at different times, form the bulk of the data presented in this thesis.

This paper is divided into four parts. In Part I we shall discuss the spectroheliograph, its adaptations for the present work, and certain characteristics of the instrumental resolution and scattered light which have particular bearing on the present observations. In Part II we discuss the method of obtaining the data and reducing it in the laboratory. Part III contains a presentation of the data obtained to date concerning the macroscopic motions in the solar atmosphere, and part IV presents some possible interpretations of these results. A major part of the data presented here and some of the conclusions drawn have already been reported (2).

## PART I. THE SPECTROHELIOGRAPH

The observations described in this thesis were obtained with the thirteen foot spectroheliograph at the sixty foot solar tower telescope of the Mt. Wilson Observatory. We shall begin this section with a brief discussion of the spectroheliograph and its operation, and a description of the auxiliary apparatus which has been introduced, to a large extent in specific connection with the observations reported in this thesis. We shall then consider the problem of spatial and wavelength resolution in the spectroheliograph, followed by a discussion of scattered light in the instrument.

### A. The Spectroheliograph

Figure 1-1a is a schematic diagram of the optical path traversed by light in the spectroheliograph when set to record velocity fields. Several auxiliary pieces of apparatus have been introduced in addition to the normal components of a spectroheliograph. In the order in which they are encountered by the light beam, these are:

#### (1) Guider (not illustrated)

An unsilvered plate glass mirror situated several feet above the entrance slit deflects a small fraction of the incident light to a photoelectric guider, which keeps the south and west limbs of the solar image stationary to within less than 1 second of arc on days of good seeing.

Figure 1-1. (a) Schematic diagram of the optical system. A: vertical light-beam of the 65-foot tower telescope. B: optical glass beam splitter (moves with spectroheliograph). C, C': duplicate images. D: entrance slit (19.3 cm long). E: double-convex lens used to adjust the "tilt" of the spectral lines. F: double-concave lens used to adjust the "curvature" of the spectral lines. (E and F also act as a field lens for the spectrograph.) G: "split" light-beam proceeding toward the collimator lens. H: dispersed light-beam proceeding from the camera lens (V and R designate the violet and red directions along the spectrum). I, I': plane-parallel glass blocks, whose equal and opposite tilt serves to "shift" the spectra of the two images C, C' equally in opposite directions. J: exit slit. K, K': monochromatic image "strips" passed by exit slit. L: photographic plate. M, M': latent images on photographic plate, built up of successive "strips" by the motion of the spectroheliograph. (b) Diagram of the action of the line shifter, showing the displaced line profiles. The cross-hatched sections represent the portion of the line profiles admitted to the photographic plate L by the exit slit J.

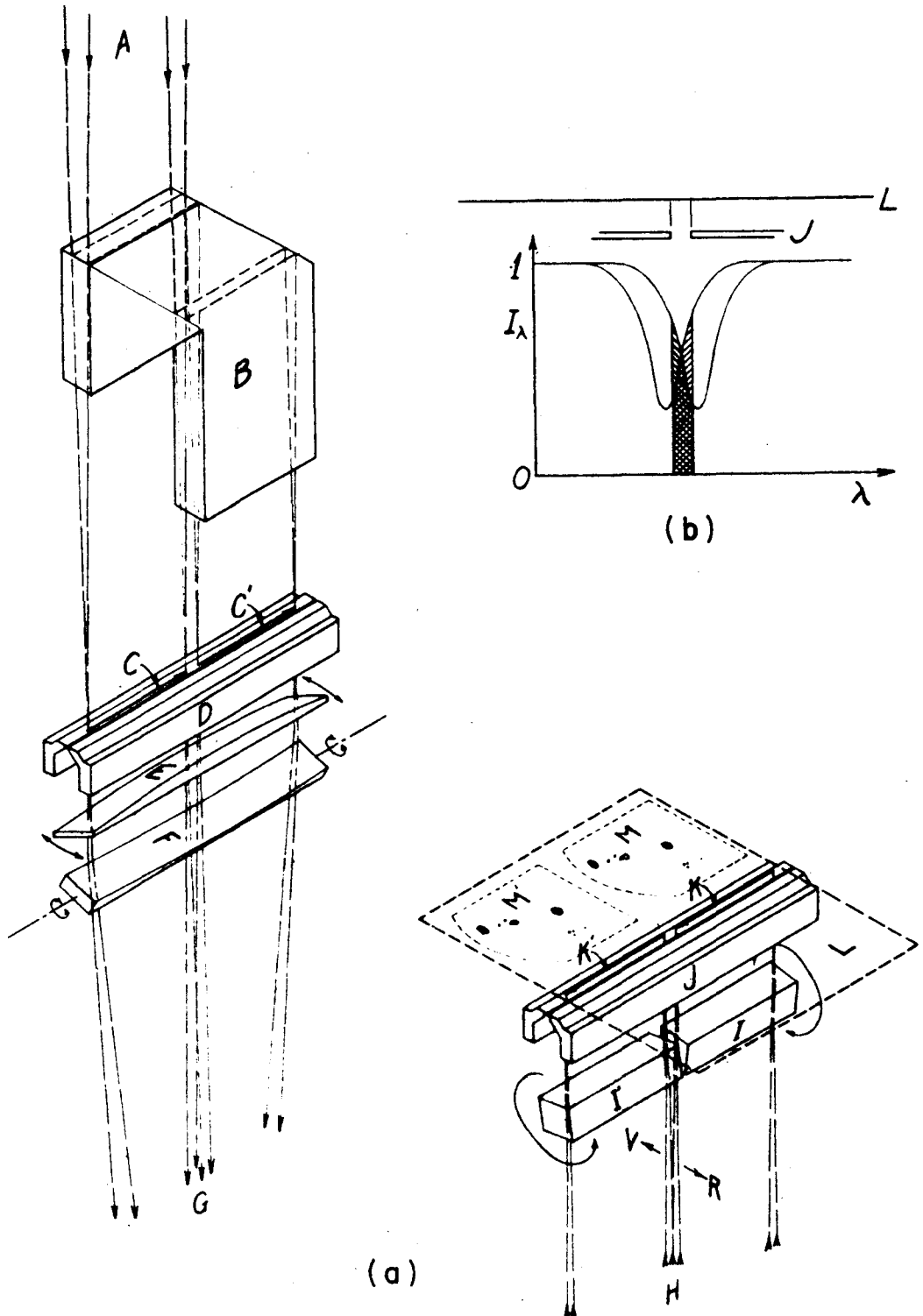


Figure 1-1

(Description on facing page (3a) )

(2) Beam Splitter (B in Fig. 1-1a)

This instrument, placed in the light path just ahead of the spectroheliograph entrance slit, creates two identical images side by side on the entrance slit. Variations in the splitting factor of the half-aluminized mirror in the splitter necessitate placing a neutral step wedge "compensating filter" in the more intense beam to equalize the intensities of the two images. Attached to the beam splitter is a shutter which can cut off the light to each image simultaneously, and which is actuated automatically at the end of each exposure. Finally, a "plate indexing circuit" causes a set of metal "fingers" to be inserted in the light path just above the slit, each finger blocking out the light over a small area of the image. The "registration marks" thus created on the photographic plate are in identical positions on each image and aid in placing the two images in register for photographic cancellation.

(3) Curvature and Tilt Correcting Lenses (E and F in Fig. 1-1a)

The double-convex "tilt" correcting lens and the double-concave "curvature" correcting lense are situated just below the entrance slit. These lenses introduce curvature and tilt to the spectral lines just sufficient to cancel out the curvature introduced by the grating and the combined tilt due to imperfect alignment of the grating system and to solar rotation. Such corrections are essential for making

velocity observations, due to the requirement of extremely precise positioning of the spectral line below the second slit.

(4) Line Shifter (I, I' in Fig. 1-1a)

The line shifter consists of two glass blocks, situated side by side below the exit slit. Each glass block transmits light from one of the two images created by the beam splitter. The blocks may be tilted equal amounts in opposite directions, thus shifting the spectral lines at the exit slit by equal and opposite amounts.

For velocity measurements the line shifter is used in conjunction with the beam splitter in the following way: With the blocks initially having no tilt, the slit is precisely centered on a spectral line having a symmetrical profile. The blocks are then tilted a prescribed amount, so that the wavelength of light passed by the slit corresponds to a position on the red wing of the line for one image, and an equidistant position on the violet wing for the other image (Fig. 1-1b). A Doppler shift of the line then moves the line core toward the slit for one image, and away from the slit for the other, thereby producing opposite small changes in the total light intensity passed by the slit to the photographic plate. Thus the contribution of Doppler shifts to the density of the developed plate at any point is the small "difference signal" between the much larger total densities of the two images at that point. This difference signal is later separated from the main density pattern by a photographic "subtraction" technique to be described later.

(5) Slit Drive Motor (not illustrated)

A slit drive motor has been provided which causes the second slit to be driven slowly across the profile of a spectral line of interest. It is coupled by a microswitch to the plate indexing circuit mentioned in (2) in such a way that the registration marks may be placed on the plate at the instant the second slit is at any desired predetermined place on the profile. The slit drive motor, coupled with the plate indexer, is used for velocity calibration purposes, to record the position of the slit on the profile during the actual observation and also the slope of the line profile at that point. We shall discuss the details of its use in the section on observational techniques in Part II.

(6) Microscope and Photometer (not illustrated)

In order to achieve accurate velocity measurements in the way just described, it is essential that the spectral line be straight and parallel to the slit, and that the position of its center be known to within about 0.01 mm. The spectral line may be aligned and positioned to this accuracy by means of a special microscope. This microscope has cylindrical optics which magnify the image of the slit in one direction and reduce it in the other. Thus the 19 cm slit, opened to 0.10 mm is imaged into a rectangle 15 mm by 0.5 mm. The image may be examined with a normal 28 mm eyepiece or deflected into another focusing system which reduces the image to a 10 mm by 0.2 mm rectangle.

imaged on a diffusing screen directly in front of the photocathode of a 1P21 PM tube. (A 7102 PM tube is substituted for use at wavelengths greater than  $7000 \text{ \AA}$ , especially the  $\lambda 8542$  line of Ca II.) The signal from the phototube is amplified and displayed on the meter of an Eldorado photometer, or may be recorded on a Varian chart recorder. A discussion of the use of the microscope and photometer in setting on a line and adjusting it to parallelism with the slit will be deferred to Part II.

### B. Resolution of the Spectroheliograph

Due to the non-zero width of the spectroheliograph slits, third-order aberrations of the collimating and camera lenses, and finite lens and grating resolution, the spectroheliograph degrades the spatial resolution of the solar image which the 60 foot telescope forms on the entrance slit. The wavelength resolution also is degraded to a value considerably below the theoretical resolution of the grating alone. It is of interest to obtain quantitative estimates of the effects of these influences, both in order to correct the measured data for resolution loss and in order to recognize and avoid possibilities of actual misinterpretation of the data.

Consequently, an experimental and theoretical investigation of the principal sources of resolution loss was undertaken. A detailed discussion of this somewhat complex problem is presented in Appendix

I. Here we shall summarize those results of the investigation which pertain to the techniques of observation and analysis described in Part II, to the data presented in Part III, and the interpretation of this data discussed in Part IV.

### 1. Loss of Resolution Due to Curvature of the Focal Surface of the Spectroheliograph

Due to the curvature of field produced by the collimating and camera lenses, the spectroheliograph focal surface at the center of the second slit is about 9 mm higher than at either end of the slit. To get the best compromise focus, the spectroheliograph is set so that the center of each image, located approximately  $1/4$  and  $3/4$  of the way along the slit (Fig. 1-1) is in focus while the edges of each image (located at the center and ends of the slit) are somewhat out of focus. The resulting loss of spatial resolution at the edge of each image is about 1-2 sec arc on the sun, or 7-1500 km. Aside from poor "seeing," this is the largest single source of spatial resolution loss. Accompanying the loss of spatial detail is loss of wavelength resolution at the ends of the slit, resulting in a broadening and smearing of spectral line profiles.

### 2. Resolution Loss Due to Finite Slit Widths

If the apertures of the first and second slits are equal, the "transmittance" of the spectroheliograph for spatial detail of various

sizes relative to the slit-widths has been calculated; the principal result is a sharp cut-off near sizes comparable to the slit width. Significant attenuation extends to sizes equal to two or three slit widths. Experimental measurements of both wavelengths and spatial resolution as a function of slit width are presented and discussed in Appendix I.

### 3. The Effect of Magnification of the Image of the First Slit Due to Grating Dispersion

A direct consequence of Bragg's law  $\frac{n\lambda}{D} = \sin \theta_i - \sin \theta_d$  (where  $n$  = spectrum order,  $D$  = dispersion,  $\theta_i, \theta_d$  = angles of incidence and diffraction) is that if the first slit subtends an angle  $d\theta_i$  at the grating, then its monochromatic image at the exit slit subtends an angle

$$d\theta_d = \frac{\cos \theta_i}{\cos \theta_d} d\theta_i = \beta(\lambda) d\theta_i. \quad \beta(\lambda) \text{ is plotted in Appendix I; for the spectral regions normally observed, } \beta \sim 1.5.$$

One important consequence of this magnification is that for a given exposure, determined by the product of the slit widths, the wavelength resolution of the spectroheliograph is best when the second slit width is the same as that of the magnified image of the first slit, i. e., when  $a_2 = \beta a_1$  where  $a_1$  and  $a_2$  are the apertures of the first and second slit. The best resolution of spatial detail, however, occurs when  $a_1 = a_2$ .

#### 4. Loss of Resolution Due to the Gap between Exit Slit and Plate

The exit slit of the spectroheliograph lies about 0.3 cm below the level of the photographic plate. The light from the grating converges to the slit, but diverges again after passing through the slit. Thus the width of the intensity distribution which strikes the plate at any instant is greater than the slit width. The width  $2\delta$  of the distribution is determined by the slit width and the focal ratio of the optical system. For 0.07 mm slits, and with the 17 cm solar image (the effective focal ratio is then that of the 60 ft telescope) we find the width to be  $2\delta = 0.12$  mm or 1.1 sec or arc, i. e., nearly twice the slit width.

As the slits are narrowed in an attempt to attain better spatial resolution, a width (about 0.04 mm) is reached below which the resolution actually worsens. This is due to the fact that as the first slit is narrowed, the diffraction pattern of the slit widens, until finally the central maximum of the pattern fills the entire collimating lens. Then the effective focal ratio is the ratio of the collimating lens aperture to its focal length, and is about half that of the 60 ft telescope.

We shall now briefly indicate how the results of the preceding discussion should affect the observational procedures and the analysis of data.

a) If one wishes to compare observations of different points on the sun to each other (e.g. velocities at the center of the disk and near the limb) care should be taken to place the two different areas over the same points on the slit, in order to eliminate spurious results due to changes of spatial and wavelength resolution along the slit. Otherwise one must correct for these resolution changes.

b) To obtain the best wavelength resolution for a given exposure ( $a_1 a_2 = \text{const.}$ ), the slit should be set such that  $\frac{a_2}{a_1} = \beta \sim 1.5$ . However, if one is interested only in spatial resolution, the slits should be set such that  $a_1 = a_2$ . In no case should  $a_1$  be less than about 0.04 mm, for loss of resolution due to the gap between the second slit and the plate will follow. (In addition, that portion of the incident light diffracted out of the collimating lens will be lost, thus decreasing the intensity passing through the second slit.)

c) In analyzing plates, one must be aware that the photographic image contains only solar detail above a certain size, of the order of the slit width, and that in addition there may be smearing of this detail due to the optical imperfections we have just discussed.

### C. Scattered Light

A precise knowledge of the scattered light in the spectroheliograph would be very helpful in connection with a number of observational problems. For instance:

1) It is interesting to know how solar intensity variations, i. e., temperature fluctuations, vary with height in the atmosphere. In principle this could be determined by analyzing density fluctuations in spectroheliograms taken in line cores. However, light from the nearby continuum is scattered into the center of the lines; this light, which is imaged, reflects intensity fluctuations in the continuum rather than the line cores, and such an effect should be allowed for.

2) Cross-correlation functions of plates taken simultaneously in the core of a spectral line and the nearby continuum yield a very large correlation coefficient. For a set of plates taken in the  $\text{Cr}^+$  4555 line on a day (7-1-61) of exceptional seeing, for instance, a correlation coefficient of 0.61 was obtained. To what extent this is real, i. e., to what extent intensity fluctuations in the  $\text{Cr}^+$  core are correlated with fluctuations at lower levels depends, as already explained, on the amount of imaged light scattered into the line from the continuum.

The ideal way to measure the scattered light quantitatively would be with a sodium absorption tube, to create an absorption line which is intrinsically black at the center. In the absence of such an absorption tube, a few rough measurements have been made which, although they do not explicitly determine the scattered light, do yield an order-of-magnitude estimate. The following separate contributions to scattered light have been measured: a) ghosts, b) light scattered

parallel to the spectrum from an Hg emission tube source, c) non-imaged white sunlight scattered perpendicular to the spectrum.

The details of the measurements are reported in Appendix II. Here we shall merely summarize the results: The imaged scattered light intensity in the second order is about 11% of the direct intensity, due partly to ghosts (3%) and the remainder (8%) to scattering parallel to the spectrum. In addition, non-imaged scattered light (scattered perpendicular to the spectrum) has an intensity of several percent of the direct intensity.

Although these results have an important bearing on observational work planned for the future, they do not have a significant effect on the present observations. Hence we shall not discuss them further at this point.

## PART II. METHODS OF OBTAINING, REDUCING, AND ANALYZING DATA

In Part II we shall first discuss in some detail the actual processes involved in obtaining the velocity spectroheliograms and subsequently "cancelling" them photographically to produce Doppler plates and Doppler difference or sum plates. Following this we shall take up a description of the methods of obtaining statistical information about the reduced plates from an "autocorrelation device." Finally, we shall consider the various sources of error which can enter into the measured statistical properties of the photographic plates and the extent to which these errors can lead to incorrect interpretation of the results.

### A. The Collection and Reduction of Data

Most of the observational and photographic techniques to be discussed here have already been presented (1, 2), but in the interest of completeness we shall repeat the discussion, expanding on some of the details which could be treated only lightly or not at all in the abovementioned papers.

Observations were taken from mid-May until mid-September during the summers of 1960 and 1961. Observations generally began within twenty or thirty minutes after sunrise (as soon as the image

brightness allowed and the sun rose far enough above the horizon to escape low-lying atmospheric turbulence) and continued as long as atmospheric stability permitted (usually between thirty minutes and two hours). The method of observation is as follows: the spectral line to be observed is chosen and the slit widths, spectroheliograph and telescope focus, nominal positions of the curvature and tilt correcting lenses, and zero correction for the line shifter set. The beam splitter is positioned with the appropriate order-separation filter and compensating filter setting, creating essentially identical images side by side on the first slit. The 17 cm solar image is positioned on the first slit, and the spectral line desired is brought below the second slit by tilting the grating. Using the microscope and photometer, the center of the line profile is found photometrically for light entering each of four different positions along the first slit. If the location of the center of the profile is found to vary along the slit, corrections of the curvature and tilt lens settings as well as the zero position of the line shifter are made until the line is parallel to the slit to within at most 0.01 mm along its entire length. The area of the sun to be observed is selected and the guider is positioned accordingly. The guider is checked to make sure it is operating as sensitively as possible for the particular conditions of seeing, brightness, and scattered skylight. With the solar image in its observing position, the final position of the entire spectral line is measured, the slit is placed at

the center of the profile, and the microscope is removed. Using the line shifter, the spectral line is offset by the required amount, in opposite directions for the two images. This places the opposite wings of the profile under each corresponding half of the slit. For most of our observations the slit is offset to that point on the profile where the logarithmic slope of the profile  $\frac{I dI}{I d\lambda}$  is greatest, thus giving the greatest Doppler sensitivity (p. 25 ). An 8X 10 inch Eastman Kodak spectroscopic plate of the appropriate emulsion (II-0 for  $\lambda < 5000 \text{ \AA}$ , II F for  $5000 \text{ \AA} < \lambda < 6800 \text{ \AA}$ , I-N for  $\text{Ca}^+ 8542$ ) is loaded and placed in position above the second slit. The spectroheliograph traverse speed is selected after noting the image brightness on a brightness meter and the exposure is begun. At the end of the exposure, which for a typical 11 cm traverse requires three to five minutes, the plate is immediately shifted to place fresh emulsion over the slit and a new exposure begun, this time with the spectroheliograph travelling in the opposite direction. Sometimes the setting of the line shifter is reversed between exposures, thus reversing the sign of the Doppler shift contribution to each image. The plate indexing circuit is actuated at each end of the image to provide registration marks for use in later photographic subtraction.

At the end of a sequence of observations, an expanded line profile is recorded, for later use in calibration. This is accomplished

in the following way: The shifter is reset to zero and the slit drive motor is engaged with the micrometer which positions the second slit, thus enabling the slit to be driven slowly across the line profile. A cam, which revolves with the motor and actuates a microswitch closing the plate indexing circuit twice per revolution, is set to close the indexing circuit when the second slit is in the precise position it occupied during the observation. Since the second slit micrometer moves at 0.50 mm per revolution, the plate indexer will also be actuated when the slit is 0.25 and 0.50 mm either side of its position during the observation. The slit is then backed off some distance greater than 0.25 mm and a short spectrohellogram is taken, during which the slit is driven past the spectral line. The result is a greatly expanded line profile, with index marks at the precise wavelength occupied by the slit and at wavelengths corresponding to a distance 0.25 mm either side. The latter marks, together with knowledge of the spectrograph dispersion, serve to establish the wavelength scale of the profile. The line profile serves two purposes: (a) it records the exact position of the slit on the line and whether the alignment of the line and slit was satisfactory, and (b) it yields, after microphotometer tracing, the slope of the line profile at the shifter offset used; this is essential in order to translate transmission variations on the plate into absolute velocity fluctuations on the sun.

After the observations are made, the plates are exposed at one edge to a calibrated step wedge source (red for II-F and I-N emulsions, violet for II-O), and developed for five (II-O or I-N) or ten (II-F) minutes in full strength D-19, fixed, washed, and dried.

Each member of a pair of images which were exposed simultaneously in the manner described above is ideally identical to the other in every respect except for small density variations caused by Doppler shifts of the spectral line, which produce opposite variations on the two images. In order to extract this small "difference signal" from the much larger main density field, a photographic subtraction technique is used: a negative contact print is made of one of the two images and developed to unity gamma, such that, when placed in register on its own positive, a uniform gray field results.\* When placed in register on the other member of the image pair, however, the Doppler signals, being originally of opposite polarity, now reinforce. Therefore, these two plates when cemented in register show a uniform gray field everywhere except where there was a Doppler shift of the spectral line, and the departure from grayness is proportional to the magnitude of the shift. Such a Doppler plate exhibits

---

\*The relation between the intensity  $I$  striking any point of a photographic plate and the transmission  $T$  at that point on the developed plate is  $T = CI^\Gamma$  where  $C$  and  $\Gamma$  are functions of exposure and development time. For a contact print  $I \propto 1/T_0$  where  $T_0$  is the transmission of the plate being printed. Therefore, if  $\Gamma = 1$ ,  $T = \text{const.}/T_0$ , and the transmission of the original and its contact placed in register is  $T T_0 = \text{const.}$

many interesting properties and merits detailed study; however, it is also of interest to subtract two Doppler plates in the manner just described. This yields Doppler sum or difference plates, depending on whether the line shifter was reversed or left unchanged between exposures. A Doppler sum or difference plate exhibits departures from uniform grayness at any point whenever the sum or difference of the velocity fields, as recorded at the two times the spectroheliograph scanned that point, is not zero. These two times are separated by an interval which varies linearly along the plate from nearly zero (at that end of the image scanned at the end of the first exposure and at the beginning of the second exposure) to six or eight minutes at the other end.

(In order to obtain a difference or sum plate from two successively scanned Doppler plates, each of which consists of a "sandwich" of two plates cemented emulsion to emulsion, each Doppler plate is first projection printed to unity gamma in order to bring the image to the surface of a plate for further cancellation. During the projection printing the image is purposely slightly defocused by an amount sufficient to wash out the image of plate grain in the first cancellation, but not enough to degrade solar detail significantly. Following this, the procedure is the same as for a first cancellation: a contact print of one image is made to unity gamma and superimposed on the other to bring out the difference signal between the two plates.)

## B. The Analysis of Data: Autocorrelation and Cross Correlation Functions and Their Interpretation

As we shall discuss in Part III, many of the results obtained from this investigation are qualitatively apparent after a visual examination of the plates in various stages of reduction. However, to obtain quantitative information about the nature of the velocity structure (e. g. the magnitude of the velocities, the dimensions of the elements over which the velocity is coherent, the variation of average velocity with position on the solar disk, etc.), some sort of more objective measurement procedure is necessary. A traditional method of analysis would be to make essentially one-dimensional microphotometer tracings across an area of interest, and with the help of our velocity calibration procedures, to determine the velocity profile along the line traced. We are, however, more interested in the statistical properties of the field, as averaged over a large area, than in the velocity as measured at discrete points with the microphotometer.

By quite laborious measurement and analysis procedures it is possible to obtain statistical information, such as the one-dimensional autocorrelation function, from a microphotometer tracing. It would actually be far better to use a two-dimensional autocorrelation function for statistical analysis, if it could easily be obtained, since the two-dimensional autocorrelation function averages statistical properties

over an area rather than along a line. A relatively painless method for obtaining the two-dimensional autocorrelation function directly has in fact been developed; consequently a very large fraction of our quantitative results has been obtained from two-dimensional autocorrelation function techniques.

The two-dimensional autocorrelation (A-C) function of the transmission over a given area  $A$  is defined as

$$C(\vec{s}) = \frac{1}{A} \int_A T(\vec{r}) T(\vec{r} + \vec{s}) dA \quad \equiv \quad \langle T(\vec{r}) T(\vec{r} + \vec{s}) \rangle \quad (2.1)$$

If we write the transmission of the plate as

$$T(\vec{r}) = T_0 (1 + \epsilon(\vec{r})) , \quad (2.2)$$

where  $T_0$  is the average transmission

$$T_0 = \langle T(\vec{r}) \rangle , \quad (2.3)$$

then

$$C(s) = T_0^2 \langle (1 + \epsilon(\vec{r})) (1 + \epsilon(\vec{r} + \vec{s})) \rangle , \quad \text{or} \quad (2.4)$$

$$C(s) = T_0^2 (1 + \langle \epsilon(\vec{r}) \epsilon(\vec{r} + \vec{s}) \rangle) ,$$

where we have noted from equations 2.2 and 2.3 that  $\langle \epsilon(\vec{r}) \rangle = 0$ .

If we define the normalized height of an autocorrelation function to be

$$H = \frac{C(0) - C(\infty)}{C(\infty)} , \quad (2.5)$$

we see from equation 2.4 that

$$H = \langle \epsilon^2 \rangle. \quad (2.6)$$

Thus the height of an A-C function is the mean square percentage fluctuation of transmission of the area over which the mean is performed. Similarly, one can obtain the cross correlation (C-C) function of two different plates with transmissions

$$T_1(\vec{r}) = T_{10} (1 + \epsilon_1(\vec{r})), \quad T_2(\vec{r}) = T_{20} (1 + \epsilon_2(\vec{r})). \quad (2.7)$$

We see that

$$C_{12}(\vec{s}) = T_{10} T_{20} (1 + \langle \epsilon_1(\vec{r}) \epsilon_2(\vec{r} + \vec{s}) \rangle), \quad (2.8)$$

and

$$H_{12} = \langle \epsilon_1 \epsilon_2 \rangle. \quad (2.9)$$

The full width at half maximum (FWHM) of an A-C or C-C function is a measure of the linear size of the elements in the field. The exact relation between the FWHM and the statistical properties of the sizes of the elements is a complicated function of the power spectrum; nevertheless, mathematically amenable trial functions yield A-C curves with halfwidths which are indeed of the same order of magnitude as the characteristic size of the elements contributing to the A-C function.

An A-C function contains much more information than that given by its height and width; in fact, one can obtain from it the spectral

distribution of the statistical field represented by  $T(x, y)$ , since the Fourier transform of the A-C function is the absolute square of the Fourier transform of  $T(\vec{r})$  (3). However, all the results reported here have been obtained by analysis of the height and FWHM alone.

In order to obtain the A-C or C-C function of the transmission field of a photographic plate, a device (Fig. 2-1) was built to carry out the integral involved in equation 2.1 photometrically. To obtain the A-C function over a given area  $A$  of a plate, two copies of the plate are made which are mirror images of each other, so that they may be placed in register with their emulsions in contact. We shall refer to these two plates as a right-left pair. On one plate, the entire area except for the area of interest is masked off. The plates are fixed to separate frames, which are placed in a holder in such a way that their emulsions are in contact and in register. A motor drive slides one plate slowly past the other. Collimated light is passed through the two plates and is brought to a focus on the photocathode of a photomultiplier tube. At each point, the light transmitted is proportional to the product of the transmittances of the two plates at that point, and the total light collected by the photomultiplier is the integral of that product over the area of interest. Thus, when the plates are displaced an amount  $s$  in the x-direction and  $t$  in the y-direction, relative to each other, the photomultiplier records  $C(s, t)$  (eq. 2.1). In practice,  $t$  is usually zero. The signal  $C(s, 0)$  from the photo-

Figure 2-1. Schematic diagram of the autocorrelation device. A: 6-v, 4.5 A coiled-filament lamp, air-cooled to reduce convection currents. B: beam defining stop. C: gradient-compensating filter. This filter has a linear density gradient from edge to edge; by adjusting its azimuth, an over-all "dlr" of the A-C curve may be avoided. D, D': plano-convex condensing lenses. D renders the light parallel, and D' concentrates it upon the photomultiplier cathode. E, F: fixed mounting frame. F': movable frame. G, G': circular plate carriers. These carriers may be rotated  $0^{\circ}$ - $360^{\circ}$  in azimuth and locked in position. H, H': matched right- and left-hand plates, emulsion sides in contact. The plates are fixed to the carrier G, G' so as to be in register when the carriers are concentric and co-azimuthal. I: aperture stop which defines the area of integration. J: motor-driven micrometer, which slides frame F' slowly past F. (Motor not shown.)

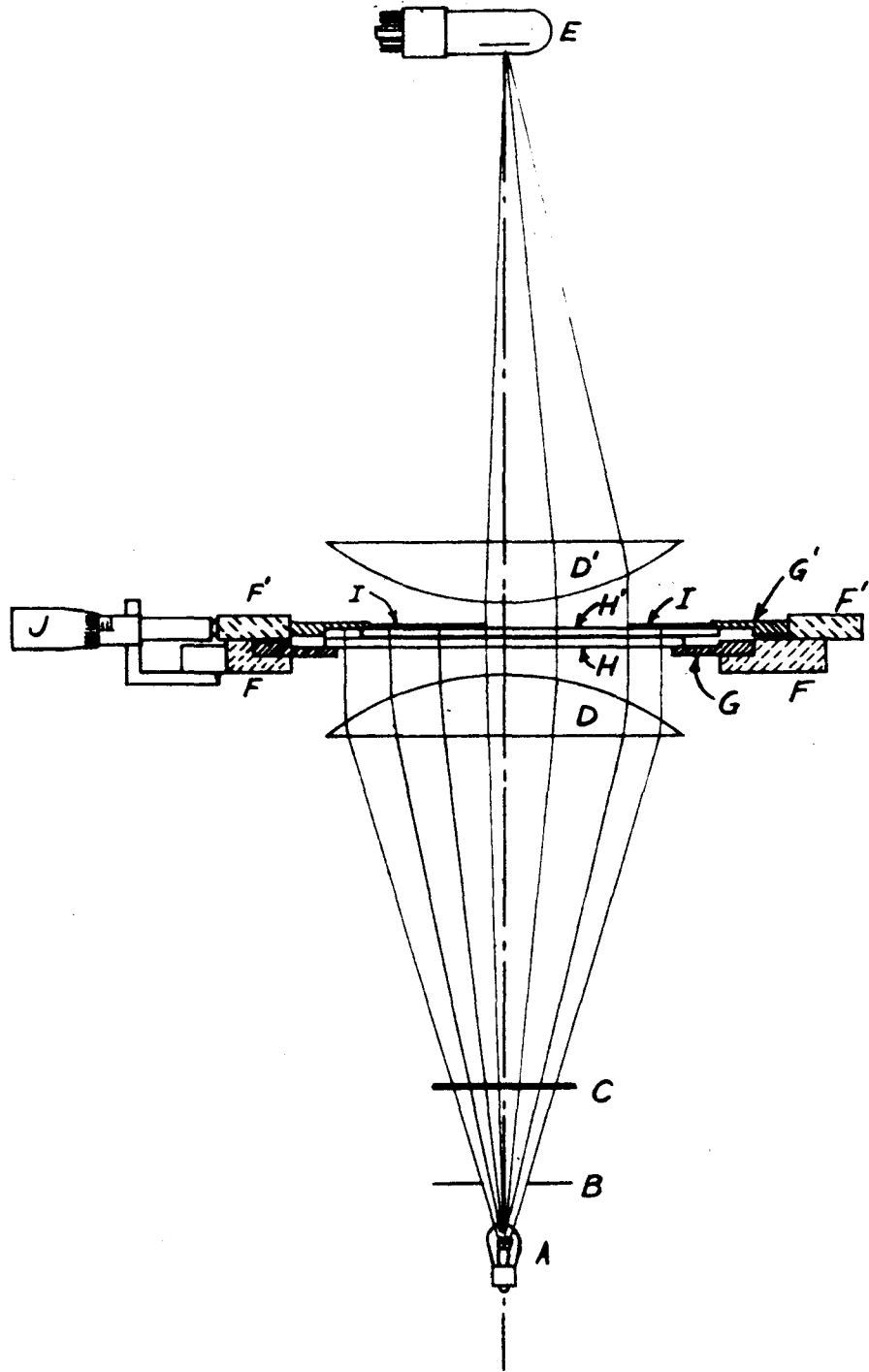


Figure 2-1

(Description on facing page (23a) )

multiplier is amplified and fed into a 0-10 mV chart recorder. Since the fluctuation of  $S(s, 0)$  seldom exceeds 10 percent,  $C(s, 0)$  varying between 9 and 10 mV when  $C(0, 0)$  is normalized to 10 mV, a 10x multiplier resistor is inserted in the circuit, along with a 90 mV bucking voltage. Thus the chart recorder's range is between 90 and 100 mV, and the full scale of the chart represents a 10 percent change in the signal. Multiplication by other factors with appropriate bucking voltages is also sometimes used.

We shall now discuss how the heights and FWHM of auto-correlation and cross-correlation curves may be interpreted to yield quantitative information about the statistical properties of the brightness and velocity fields of the solar atmosphere. A number of basic assumptions underlie our interpretations. Some of these have more validity than others; later we shall discuss the question of their validity in some detail. The basic assumptions and their consequences are:

1) The presence of a non-zero line-of-sight component of velocity over an area sufficiently large to be resolved by the instrument simply shifts the spectral line bodily by an amount  $\Delta \lambda = \frac{v}{c} \lambda$ , without changing its shape or residual intensity.

2) The slope of the line profile is constant over a wavelength range larger than any Doppler shifts actually encountered; furthermore, it is opposite for points equidistant from the line core

on either wing (the line is symmetric). Assumptions 1) and 2) imply that a line-of-sight velocity component adds an increment of intensity to a point on one image which is directly proportional to the velocity, while it subtracts an equal increment of intensity from the other image. The fractional increment in intensity is

$$\frac{\Delta I}{I} = \pm \frac{v \lambda}{c} \frac{1}{I} \frac{dI}{d\lambda} \Big|_{\lambda_0 + \Delta \lambda_0} = \pm \frac{v}{c} \lambda \frac{d \ln I}{d\lambda} \Big|_{\lambda_0 + \Delta \lambda_0} \quad (2.10)$$

where  $I(\lambda)$  is the unshifted line profile,  $\lambda_0$  is the position of the line core, and  $\Delta \lambda$  is the offset of the line core from the slit. The line profile  $I(\lambda)$  is the intrinsic line profile smoothed out by the instrumental resolution window; i. e., it is the intensity profile measured at the plate position by scanning with the second slit.

3) The intensity striking the plate consists of a mean intensity plus small fluctuations about the mean. If  $(x, y)$  are coordinates on the plate,  $I(x, y) = I_0 \left(1 + \frac{\Delta I(x, y)}{I_0}\right)$ ,  $\Delta I/I_0 \ll 1$ .  $\frac{\Delta I}{I_0}$  consists of the Doppler shift contributions

$$\lambda \frac{v}{c} \frac{d \ln I}{d\lambda} = \delta(x, y) \quad (2.11)$$

plus other contributions which we lump together into a term  $\beta(x, y)$ .

The main contribution to  $\beta$  is due to fluctuations of the solar intensity.

(We shall often adopt the working hypothesis that  $\beta$  is proportional to a temperature fluctuation. In view of the complexity of the problem of line formation, this is a rather risky assignment to make; one

justification will be the rather self-consistent picture which emerges as a result.) We choose the signs of  $\beta$  and  $\delta$  such that  $\delta$  is positive for upward (approach) velocities when the slit is in the red wing of the line, and  $\beta$  is positive for increases of intensity. Then

$$I_{r,v}(x,y) = I_0(1 \pm \delta(x,y) + \beta(x,y)) \quad (2.12)$$

where  $r$  and  $v$  refer to the red and violet wings of the line. Further, we assume  $|\delta| \ll 1$  and  $|\beta| \ll 1$ .  $I_0$  is chosen such that  $\langle \pm\delta + \beta \rangle = 0$ , i.e.,  $\langle \delta \rangle = \langle \beta \rangle = 0$ . ( $I_0 = \langle I \rangle$ .)

4) The gamma of the spectroheliograph plate is constant.

Therefore, the transmission  $T$  of the plate is  $T \propto I^\Gamma$ . From 3),  $T = T_0(1 \pm \delta + \beta)^\Gamma$ . Because  $\frac{\Delta I}{I} \ll 1$ , we approximate

$$T = T_0(1 + \Gamma\beta \pm \Gamma\delta). \quad (2.13)$$

5) In the reduction process, a contact transparency of one image is exposed and developed to gamma (it is assumed) of exactly unity. Then the transmission of the contact,  $T_{cr} = (T_r)^{-1} = T_{oc}(1 + \Gamma\beta \pm \Gamma\delta)^{-1} \approx T_{oc}(1 - \Gamma\beta \mp \Gamma\delta)$ . Therefore, when the contact is placed in register upon its mate, the single (IX) cancellation which results has the transmission

$$T_{IX} = T_0(1 + \Gamma\beta \pm \Gamma\delta) T_{oc}(1 - \Gamma\beta \mp \Gamma\delta) = T_{IX0}(1 \pm 2\Gamma\delta) \quad (2.14)$$

to terms of second order in  $\beta$  and  $\delta$ .

6) Similarly, a double (ZX) cancellation, which is prepared by making a contact print to unity gamma of a singly cancelled Doppler plate and placing it in register upon a second Doppler plate taken at a different time, has a transmission (if the shifter was set so the first Doppler plate has  $T_{1X} = T_{1X_0} (1 + 2\Gamma \delta)$ )

$$T_{ZX} = T_{1X_0} (1 + 2\Gamma \delta(x, y, t_1(x, y))) T_{1X_{0c}} (1 \mp 2\Gamma \delta(x, y, t_2(x, y))) \text{ or} \quad (2.15)$$

$$T_{ZX} = T_{ZX_0} (1 + 2\Gamma (\delta(x, y, t_1) \mp \delta(x, y, t_2))),$$

depending on whether the shifter was left unchanged (difference) or reversed (sum) between exposures.  $t_1(x, y)$  and  $t_2(x, y)$  are the two times of scanning the point  $(x, y)$ .

5) and 6) follow from assuming unity gamma of the plates in the cancelling process and that  $|\beta|$  and  $|\delta| \ll 1$ .

If we accept the preceding assumptions, and if we add the (non-trivial!) assumption that the output of the autocorrelation machine really is the purported autocorrelation function, we may relate the height of the curves to the statistical parameters of the solar velocity and brightness fields. Namely:

1) The root mean square (rms) velocity is determined from the height of an A-C function of a Doppler (singly cancelled) plate to be

$$\langle v^2 \rangle^{\frac{1}{2}} = \left\langle \left( \frac{c}{\lambda} \frac{1}{\frac{d \ln I}{d \lambda}} \delta \right)^2 \right\rangle^{\frac{1}{2}} = \frac{c}{\lambda} \frac{1}{\frac{d \ln I}{d \lambda}} \frac{1}{2\Gamma} \langle (2\Gamma \delta)^2 \rangle^{\frac{1}{2}} \text{ or} \quad (2.16)$$

$$\langle v^2 \rangle^{\frac{1}{2}} = \frac{c}{2\lambda} \frac{1}{\frac{d \ln T}{d \lambda}} (H_{1X})^{\frac{1}{2}},$$

using equations 2.2, 2.6, and 2.14 and noting  $\Gamma \frac{d \ln I}{d\lambda} = \frac{d \ln \Gamma}{d\lambda}$ .  $\frac{d \ln \Gamma}{d\lambda}$  is found from a microphotometer tracing of the line profile (see Section C).

1) The rms sum or difference between the velocity as measured at two times  $t_1$  and  $t_2$  is found in the same way from an autocorrelation curve of a (doubly cancelled) sum or difference plate to be

$$\begin{aligned} \langle (v_{t_1} \pm v_{t_2})^2 \rangle^{\frac{1}{2}} &= \frac{c}{\lambda} \frac{1}{\frac{d \ln I}{d\lambda}} \langle (\delta_{t_1} \pm \delta_{t_2})^2 \rangle^{\frac{1}{2}} \\ &= \frac{c}{2\lambda} \frac{1}{\frac{d \ln \Gamma}{d\lambda}} (H_{2X})^{\frac{1}{2}} \end{aligned} \quad (2.17)$$

(Note that the velocities and velocity differences or sums obtained are independent of  $\Gamma$ .)

3) We may also investigate the rms velocity, the rms intensity fluctuation, and the correlation between them from autocorrelation and cross correlation curves of the original spectroheliograph image pairs. The A-C and C-C functions of the red and violet images may be written:

$$\begin{aligned} \text{a) } C_{rr}(s) &= \langle T_r(x, y) T_r(x+s, y) \rangle = \langle [I_r(x, y)]^\Gamma [I_r(x+s, y)]^\Gamma \rangle, \\ \text{b) } C_{vv}(s) &= \langle T_v(x, y) T_v(x+s, y) \rangle = \langle [I_v(x, y)]^\Gamma [I_v(x+s, y)]^\Gamma \rangle, \text{ and} \\ \text{c) } C_{rv}(s) &= \langle [I_r(x, y)]^\Gamma [I_v(x+s, y)]^\Gamma \rangle. \end{aligned} \quad (2.18)$$

Using equation 2.5, and dropping terms above the second order in  $\beta$  and  $\delta$ , we find

$$\begin{aligned}
 \text{a)} \quad H_{rr} &= \Gamma^2 [ \langle (\beta + \delta)^2 \rangle ] = \Gamma^2 [ \langle \beta^2 \rangle + \langle \delta^2 \rangle + 2 \langle \beta \delta \rangle ] \\
 \text{b)} \quad H_{vv} &= \Gamma^2 [ \langle \beta^2 \rangle + \langle \delta^2 \rangle - 2 \langle \beta \delta \rangle ] \\
 \text{c)} \quad H_{rv} &= \Gamma^2 [ \langle \beta^2 \rangle - \langle \delta^2 \rangle ]
 \end{aligned} \tag{2.19}$$

Thus,

$$\begin{aligned}
 \text{a)} \quad \langle \delta^2 \rangle &= (H_{rr} + H_{vv} - 2 H_{rv}) / 4 \Gamma^2, \\
 \text{b)} \quad \langle \beta^2 \rangle &= (H_{rr} + H_{vv} + 2 H_{rv}) / 4 \Gamma^2, \text{ and} \\
 \text{c)} \quad \langle \beta \delta \rangle &= (H_{rr} - H_{vv}) / 4 \Gamma^2
 \end{aligned} \tag{2.20}$$

Finally, using  $v = \frac{c}{\lambda} \frac{1}{\frac{d \ln I}{d \lambda}}$   $\delta = \Gamma \frac{c}{\lambda} \frac{1}{\frac{d \ln T}{d \lambda}}$   $\delta$ , we obtain

$$\begin{aligned}
 \text{a)} \quad \langle v^2 \rangle &= \frac{c^2}{4 \lambda^2} \left[ \frac{1}{\frac{d \ln T}{d \lambda}} \right]^2 (H_{rr} + H_{vv} - 2 H_{rv}), \\
 \text{b)} \quad \langle \beta^2 \rangle &= \frac{1}{4 \Gamma^2} (H_{rr} + H_{vv} + 2 H_{rv}), \text{ and} \\
 \text{c)} \quad \langle \beta v \rangle &= \frac{c}{4 \Gamma \lambda} \frac{1}{\frac{d \ln T}{d \lambda}} (H_{rr} - H_{vv}).
 \end{aligned} \tag{2.21}$$

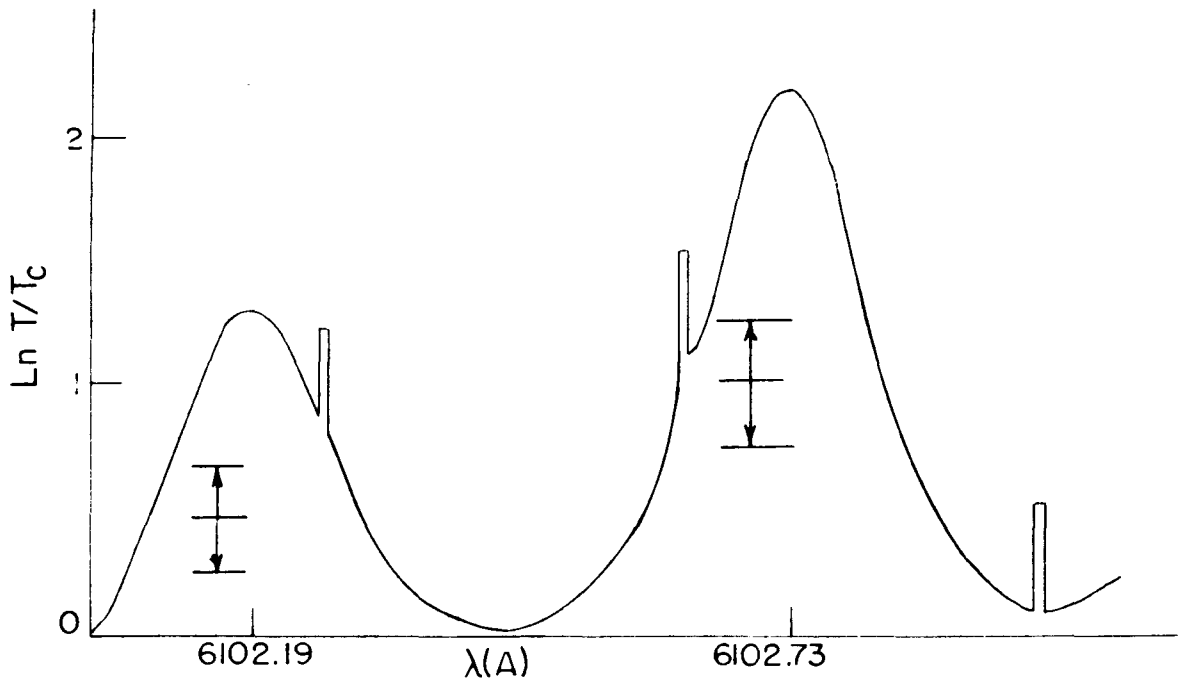
Note that if our underlying assumptions are correct, this second separate method of determining  $\langle v^2 \rangle$  (eq. 2.21) should agree with the first one (eq. 2.16). We shall see later that there is actually significant disagreement between the results of the two methods, indicating that if we wish to obtain very precise quantitative information, we should refine our assumptions and perhaps also our

techniques of obtaining A-C and C-C curves.

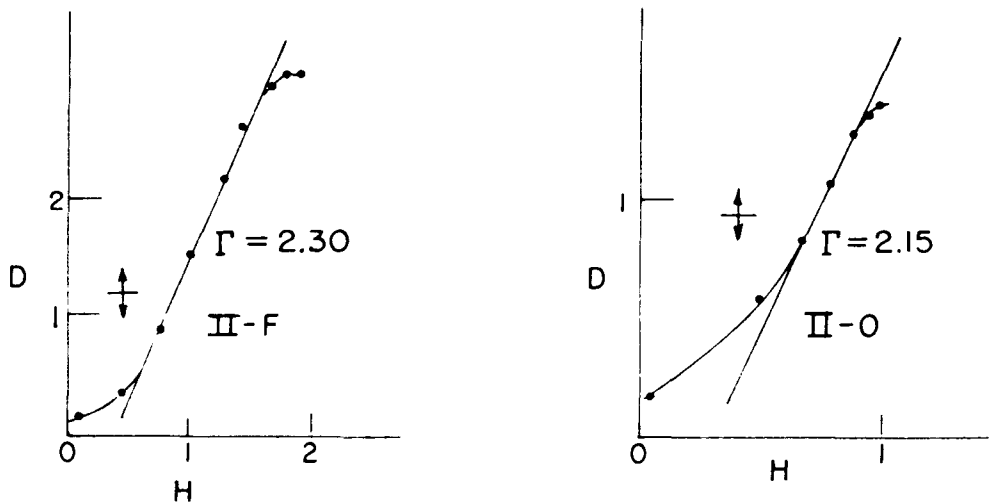
### C. Calibration

As we saw in the last section, in order to interpret density fluctuations on Doppler plates in terms of actual velocities of gases in the solar atmosphere, we need to know the logarithmic slope of the line profile as recorded on the photographic plate at the wavelength of observation, i. e.,  $\frac{1}{T} \frac{dT}{d\lambda}$  or  $d \ln T / d\lambda$ . This is accomplished by tracing the line profile with a recording microphotometer. For ease of analysis, the microphotometer is used in conjunction with a curve follower on an x-y recorder, which causes  $\ln_e T$  to be plotted directly, where T is the transmission of the plate. The microphotometer slits used are long and rather wide, in order to average out most of the detail of the solar surface which is superposed on the structure of the spectral line. Typical plots of  $\log_e T$  versus  $\lambda$  are shown in Figure 2-2(a). Also shown are the changes in transmission on the original spectroheliogram pairs for a velocity of 1.0 km/sec. We see from equations 2.16 and 2.17 that the change in transmission on a Doppler plate will be twice as great, while on a Doppler sum (if the velocity has not changed in the interim) it will be four times as great.

The logarithmic slope of the microphotometer profile,  $\frac{d \ln T}{d\lambda}$ , as measured at the offset used in the observation, varies from observation to observation, since the shape of the profile is sensitively



a) Profile of Fe6102 and Ca6103. The middle index mark is at the normal observing position for the violet image of a Ca6103 Doppler plate. The separation of the index marks corresponds to 0.22 mm. or 0.36 Å at the spectrograph.  $T_c$  = transmission of continuum. Arrows indicate changes in transmission for  $v = \pm 1.0$  km/sec.



b) H-D curves for II-F and II-O plates.  $H = \log_{10}$  (intensity  $\times$  exposure time),  $D = -\log_{10}$  (percent transmission). Zero of H is arbitrary. Arrows show normal limits of density fluctuations.

Figure 2-2

dependent upon spectroheliograph slit width, spectroheliograph focus, gamma of the plate, and mean density of the plate. Thus the line profile must be measured for each plate reduced.

We see from equation 2.21(b) that in order to interpret brightness-caused density fluctuations in terms of actual brightness fluctuations on the sun, we need in addition to know  $\Gamma$  for the original spectroheliogram, although velocity measurements are independent of  $\Gamma$ .  $\Gamma$  is determined from the stepwedge placed on the plate at the time of observation by a calibrated step light source. Typical H-D curves for the plates used are shown in Figure 2-2(b) with mean densities and limits of density fluctuations also illustrated.

#### D. Sensitivity and Errors

Most of the quantitative results to be presented in Part III depend entirely on measured heights and half-widths of A-C and C-C curves. Thus for each plate the total output of information may be contained in one or at most several A-C or C-C curves, which therefore represent the sole end product of a rather complex and tedious observation and data reduction program. (When the number of fruitless trips up Mt. Wilson on days of poor seeing, the observational errors, and blind paths pursued are taken into account, the total investment of effort per piece of output data looms rather large.) Thus it is well worth while to analyze carefully the nature of the recorded A-C and C-C functions, and in particular to determine to

what extent they differ from the "true" A-C and C-C functions for the sun. We define the "true" functions as those which would be obtained under perfect conditions--the theoretical spatial resolution of the telescope, infinitely narrow spectroheliograph slits, no scattered light, no lens aberrations, constant gamma of the plates, no plate grain, exactly unity gamma in the reduction process, perfect superposition during cancellation, etc., but with the same wavelength resolution, and thus deriving from the same range of optical depth which contributes to the actual observations. Unfortunately, the problem of errors is so complex that it is useless to attempt to assign a magnitude to each error source and then combine them into a final error estimate. We shall in the end have to rely on certain direct measurements in order to obtain a meaningful quantitative error estimate. Nevertheless, it is useful to have in mind the various sources, in order to recognize the precautions which need be taken to minimize the errors. To this end we have undertaken to investigate all significant sources of error and, whenever possible, to make estimates of their importance by comparison with measurements. The results of this study are presented in Appendix III. Also in Appendix III we present our best attempts at quantitative estimates of the limits of error, drawn from actual measurements of some of the various separate contributions to errors, from the standard deviation of sets of observations of the same quantity, and from internal

inconsistencies in the autocorrelation curve tracing process. Here we shall summarize the principal results obtained in Appendix III:

1) Sources of Error

Errors in the final A-C function may be introduced at any or all of the stages of observation and reduction. The following list summarizes the errors in the order in which they are introduced:

a) Errors introduced into the original spectroheliogram pairs

at the time of observation and development of the plates include: resolution loss due to imperfect seeing, to imperfect spectroheliograph resolution, and to third-order aberrations of the spectroheliograph; imperfect setting of the spectroheliograph focus, the curvature and tilt correcting lenses, or the position of the slit on the spectral line; non-constant  $\Gamma$  of the plate; dust streaks; and blemishes on the emulsion. All of these sources of error except the first may be essentially eliminated by proper observational, photographic, and measurement techniques. The inevitable presence of resolution loss requires us to select only plates with the best seeing for statistical analysis, and to intercompare only plates taken under similar conditions of seeing. We must also make suitable corrections for variations along the spectrograph slit of spatial and wavelength resolution, when comparing areas on the same plate but exposed at different points on the slit.

b) Errors introduced into the first cancellation include non-unity gamma of the contact print and imperfect registration of detail

on the two images being cancelled. For velocity observations, the range of density on the original plates is sufficiently small that  $\Gamma$  may be kept constant over the entire density range, and by proper choice of exposure and development times for the contact print its value may be made very close to unity. It is, however, sometimes impossible to achieve perfect registration all over the image, due to third-order aberrations of the spectroheliograph which cause unequal magnification of the two images.

c) Errors introduced into the second cancellation are similar to those introduced into the first cancellation, but somewhat more serious. The contrast of a first cancellation for a few lines is sufficiently great that the density range over which  $\Gamma = 1$  on the second cancellation may in some cases be exceeded. Slow drifts of the guiding system with time are common and may make perfect registration over the entire plate impossible. Distortions of the image due to seeing fluctuations compound the problem.

d) Errors in the autocorrelation curve tracing process arise from the preparation of right-left prints and from the actual tracing of the curve. The principal contribution of the former is from imaged plate grain which was introduced in the original plates and each of the reduction stages. This may be minimized by slightly defocusing the image when projection printing the cemented first cancellation (p. 19), and when projection printing the right-left pairs. Errors

in the curve tracing process may arise from lack of perfect registration of the plates in the A-C machine, from improper masking of blemishes, and from effects due to the boundary of the area integrated. Ambiguities in normalization of A-C and C-C curves have not been entirely avoided.

e) Calibration errors, finally, arise from the difficulty of accurately measuring the logarithmic slope of a line profile and variations of the profile from point to point on the solar image and on the spectroheliograph slit.

## 2) Limits of Error

The combined effects of the numerous sources of error just listed have been estimated in several ways:

a) "Noise plates" were obtained with the slit on the same wing of the spectral line for each image. Thus the velocity field should be cancelled rather than reinforced in the subtraction process, leaving only "noise" due to imperfect cancellation, non-unity gamma, etc. Comparison with normal Doppler plates yields a "signal to noise" ratio of about 16 to 1 for rms velocity as measured on Doppler plates.

b) Measurements of the self-consistency of sets of A-C and C-C functions indicate that errors of about 20 percent in rms velocity may be introduced by the reduction and measurement processes.

c) Calibration errors have been estimated to be about 10 percent, from the dispersion of repeated measurements of the same profile, and of different profiles of the same spectral line.

d) The observed dispersion of measurements of velocity in one spectral line is usually less than 25 percent.

With the help of the above considerations, we adopt 30-40 percent as a conservative estimate of the "limits of error" of the velocity measured on a Doppler plate. Much of this error is systematic; as we shall discuss later, errors in relative velocities (as measured for instance at different parts of a spectral line or different points on the sun) are much less.

### PART III. THE OBSERVATIONS

We now proceed to a discussion of the observations of time-varying macroscopic velocity and intensity fields in the solar atmosphere. A number of the observations given here have already been reported (2) in somewhat less detail.

Observations of solar velocity fields were attempted in the fashion described in Part II on virtually every clear morning from June through September of 1960 and 1961. The seeing was considered good when a resolution of a few seconds of arc was attained; only rarely was one-second resolution encountered. The principal observations made were Doppler difference and sum scans with various time lags in lines of differing strengths, and scans in the core of certain chromospheric lines. The lines most often employed were, in order of increasing strength, Fe6102, Ca6103, Ba<sup>+</sup>4554, Na5896, Mg5173, Ca<sup>+</sup>3933, Ca<sup>+</sup>8542 and H $\alpha$ 6563. Roughly 32 percent of the observations, those with the best image quality or having some particular property of interest, were reduced. Some of the reduced plates were analyzed only visually; the others underwent measurements, in various stages of the reduction process, on the autocorrelation machine described in Part II and (for line profile calibrations) on the recording microphotometer in Robinson Laboratory.

We shall begin by presenting the results of observations of the instantaneous line-of-sight velocity field--the size of the elements of the field, the magnitude of the line-of-sight velocities, and the variations of these parameters with height in the solar atmosphere and with position on the disk. We shall then present evidence for a quasi-oscillatory variation in time of the velocity at every point. We shall evaluate the "average period" of this oscillation and see how it varies with altitude, and also investigate the "lifetime" of the oscillation. Next we shall turn to the intensity (brightness) fluctuations of the oscillating elements and discuss evidence for a correlation between brightness and velocity. We shall see that this correlation varies in a regular way with altitude. Finally, we shall find that at higher elevations the intensity field also undergoes a quasi-oscillatory variation. We shall evaluate the "average period" of this variation, its change with altitude, and the phase relation between the brightness and velocity oscillations.

In this part we shall content ourselves with presenting only the observational results, deferring all speculations as to their interpretation or their interrelationships to the Discussion in Part IV.

### A. The Instantaneous Velocity Field

A singly cancelled Doppler plate of the inner wing of a medium-strong spectral line, such as Ca6103, exposed over the center of the solar disk, reveals a velocity "granulation" pattern somewhat similar in size and appearance to that of the ordinary photospheric granulation as seen with poor resolution. (Fig. 3-1(a)). Indeed, the qualitative similarity between the two patterns, as well as the small separation of at most a few hundred kilometers between the line-forming region at  $\tau \sim .005$  to  $.05$  and the photospheric granulation at  $\tau \sim 0.5$  leads us to suspect that they are intimately connected. The similarity of the appearance of the velocity field to the white-light granulation is largest for the lowest-lying lines, i. e., those closest physically to the photospheric granulation. As one observes stronger and stronger lines, formed at higher and higher levels in the atmosphere, the size of the "granules" in the velocity field increases to many times that of the photospheric granules and magnetic fields in plages begin to inhibit the velocity field (Fig. 3-1(b)). Finally, in the high  $H\gamma$  chromosphere (Fig. 3-1(c, d)), the gas motions seem to bear no apparent relation to the photospheric granulation far below.

For each of the spectral lines observed, a number of Doppler plates have been obtained and reduced, and their autocorrelation (A-C) curves obtained as described in Part II. Typical A-C curves

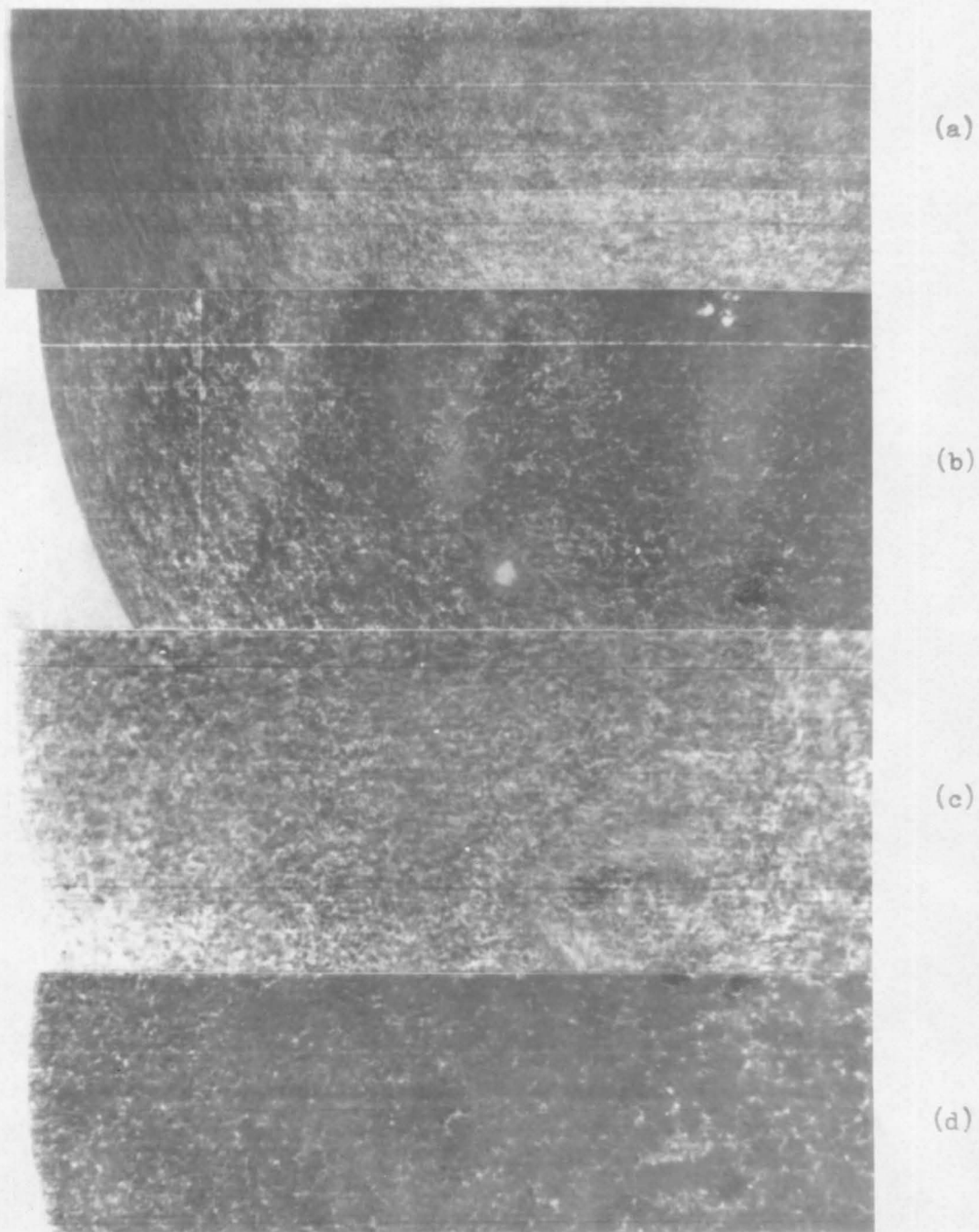


Figure 3-1. Singly cancelled Doppler plates:

- (a) Ca6103,  $\Delta\lambda = 0.1\text{\AA}$ ; darker areas receding.
- (b) Na5896,  $\Delta\lambda = 0.1\text{\AA}$ ; darker areas receding.
- (c) H $\alpha$ 6563,  $\Delta\lambda = 0.35\text{\AA}$ ; darker areas approaching.
- (d) H $\alpha$ 6563,  $\Delta\lambda = 0.7\text{\AA}$ ; darker areas approaching.

for six of the spectral lines studied are illustrated in Figure 3-2. Comparison of the various curves with each other shows that both the height (i. e., mean square velocity) and width (i. e., the size of the elements of the velocity field) increase as we progress from weaker to stronger lines. The average rms velocity for each of the lines has been determined with the help of a number of such A-C functions, using the relation  $\langle v^2 \rangle^{\frac{1}{2}} = \frac{c}{2\lambda} \frac{H^{\frac{1}{2}}}{d \ln T / d\lambda}$  (see p. 27) where H is the height of the A-C function and  $\frac{d \ln T}{d\lambda}$  is the logarithmic slope of the line profile, measured at the position of the slit on the line wing. Table I lists the rms vertical velocity for the different lines as averaged from a number of measures of different plates from different observations.

Table I<sup>1</sup>

Line	Offset (A°)	No. of sets of observations	No. of measures	$\langle v^2 \rangle^{\frac{1}{2}}$ (km/sec)
Fe6102	.10	3	18	.41 ± .04
Ca6103	.10	4	23	.43 ± .06
Ba <sup>+</sup> 4554	.07	1	4	.50
Na5896	.11	3	20	.56 ± .07
Ca <sup>+</sup> 8542	.23	1	2	1.8
H $\alpha$ 6563	.35	1	2	1.6

<sup>1</sup> Deviations shown are rms deviations from the mean of a number of measurements of various areas on several different plates, each plate taken on a different day. As shown in column three, the measurements for the lines Ba<sup>+</sup>4554, Ca<sup>+</sup>8542, and H $\alpha$  6563 were each made on plates from a single set of observations, and hence for these lines we have no estimate of probable errors due to seeing and calibration variations.

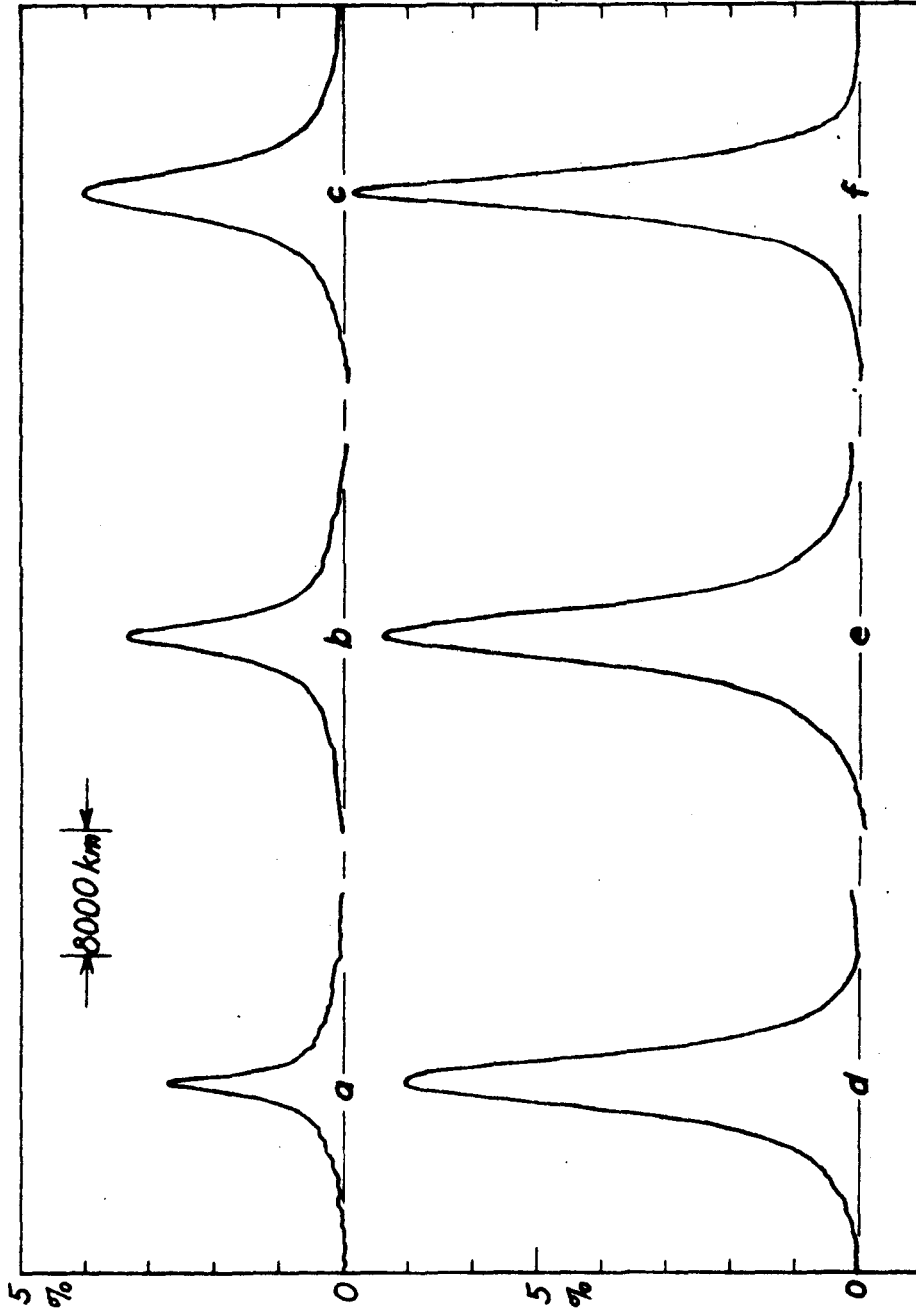


Figure 3-2. A-C curves of singly cancelled Doppler plates.

- a) Fe6102,  $\Delta\lambda = 0.10 \text{ \AA}$ ,  $H = (0.41 \text{ km/sec})^2$   
 b) Ca6103,  $\Delta\lambda = 0.10 \text{ \AA}$ ,  $H = (0.39 \text{ km/sec})^2$   
 c) Na5896,  $\Delta\lambda = 0.11 \text{ \AA}$ ,  $H = (0.58 \text{ km/sec})^2$   
 d) Ba<sup>+</sup>4554,  $\Delta\lambda = 0.07 \text{ \AA}$ ,  $H = (0.49 \text{ km/sec})^2$   
 e) H <sub>$\alpha$</sub> <sup>+</sup>6563,  $\Delta\lambda = 0.50 \text{ \AA}$ ,  $H = (1.6 \text{ km/sec})^2$   
 f) Ca<sup>+</sup>8542,  $\Delta\lambda = 0.23 \text{ \AA}$ ,  $H = (1.8 \text{ km/sec})^2$

Also listed in Table I are the number of different sets of observations contributing to the average, and the number of A-C curves obtained. (In each set of observations, several plates may have been taken and on each plate several A-C curves were often run over different areas, or scanned in different directions.) Deviations shown are rms deviations from the means; most of the contributions to these deviations are due to certain factors which vary from plate to plate and day to day. Chief among these are: (a) seeing variations, with consequent variations in resolution of the solar velocity field, and (b) velocity calibration errors, different for each set of observations.

Table II shows the results of attempts to explore the velocity structure within individual spectral lines by taking plates at different offsets. For each line, although the individual velocities are subject to the errors just mentioned, the relative sizes of the velocities are nearly free of such errors: (a) The effect of slow seeing variations is essentially eliminated by exposing an entire set of images with different offsets from a line during a single observational sequence, and also by arranging the order of taking the images such that an image at every offset immediately precedes and follows an image at every other offset. (b) Since all images are part of the same observational sequence, the calibration is the same for all. The remaining variations which contribute to the rms deviations shown in Table II

Table II\*

## Variation of Velocity within Spectral Lines

Line	Offset (A)	$\langle v^2 \rangle^{\frac{1}{2}}$ (km/sec)
Fe6102	( 0.13	0.35 $\pm$ 0.01
	( .10	.37 $\pm$ .01
	( .07	.40 $\pm$ .01
	( .04	.49 $\pm$ .01
Ca6103	( .13	.43 $\pm$ .01
	( .10	.40 $\pm$ .02
	( .07	.43 $\pm$ .01
	( .04	.45 $\pm$ .05
Na5896	( .17	.42 $\pm$ .01
	( .14	.41 $\pm$ .01
	( .11	.48 $\pm$ .01
	( 0.08	0.49 $\pm$ 0.01

---

\* Eight measurements were made of four different images for each offset. Deviations shown are rms deviations from their mean. The values of the velocities disagree with those in Table I because they refer to only one set of observations, while entries in Table I show the average of several sets of observations.

are mainly due to photographic and instrumental noise in the A-C curve tracing process. In addition, there are probably small systematic errors remaining due to errors in measuring the difference in velocity calibration between different parts of a line profile. Nevertheless, it is felt that these measurements do indicate a tendency toward higher velocities in the core of a line than in its wings.

We conclude from Tables I and II therefore that there is a definite trend toward the increase of vertical velocity with height in the upper photosphere and low chromosphere, both from line to line and within lines. This finding is in substantial agreement with that of other investigators (4, 5, 6). It should be pointed out that the velocities listed in Tables I and II, being rms velocities averaged over areas containing both quiescent and moving elements, do not represent typical velocities of a moving element. Indeed, if we anticipate the results of the discussion in Part IV and associate the motions with the presence of bright photospheric granules directly below, we find from estimates (7) of the fraction of the photosphere covered by bright granules that approximately one-third of the atmosphere directly above is in motion. The figure of  $1/3$  also agrees with the estimate by Evans and Michard (8) of the fraction of the vertical velocity field undergoing oscillatory motion at any one time. Thus typical velocities within individual moving elements might be

about  $\sqrt{3}$  times as large as given in Tables I and II. The observed velocities listed in Tables I and II are plotted, with their probable errors, in Figure 3-3. The abscissa is the height above  $\tau = 0.003$  at which the various velocities are observed. The actual assignment of a height of formation to a given part of the profile of a given line is of course an exceedingly complicated matter. In Figure 3-3, and elsewhere in this paper, we define the height  $z$  of formation to be the height where the emergent intensity  $I(\lambda)$  as measured by the residual intensity of the line is equal to the black body source function  $B_{\lambda}(T) = \frac{2\pi hc^2}{\lambda^5} (e^{hc/\lambda kT} - 1)^{-1}$ .  $T = T(z)$  is the equilibrium temperature prevailing at height  $z$ . Thus, if  $r$  is the residual intensity expressed as a fraction of the continuum intensity,  $I(\lambda) = B_{\lambda}(T(z)) = rB_{\lambda}(T_e)$  ( $T_e$  is the "effective temperature" of the sun).  $z$  is then determined for each value of residual intensity by solving  $r = \frac{e^{hv/kT_e} - 1}{e^{hv/kT} - 1}$  for  $T(z)$  and using an atmospheric model (we used the model given by Allen (7)) to determine  $z$ . This crude approximation cannot avoid giving incorrect absolute heights, especially in the chromosphere where the continuous opacity is much less than the line opacity and where the source function becomes complicated through scattering and the absence of local thermodynamic equilibrium. Nevertheless, the ordering of the lines which it suggests is probably approximately correct; the exact placement of the lines will not seriously affect the interpretations which will result from the observations.

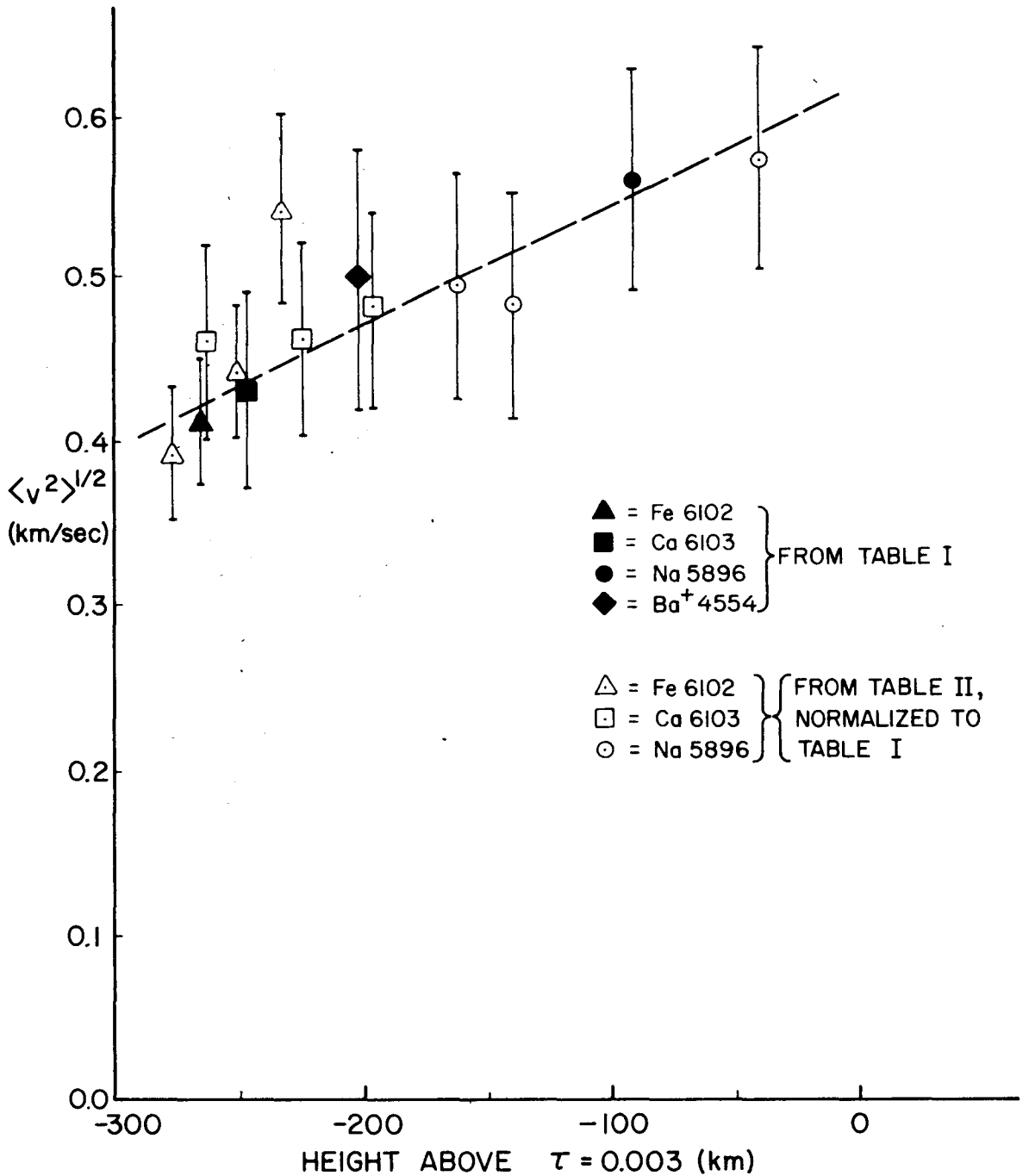


Figure 3-3.  $\langle v^2 \rangle^{1/2}$  versus height of formation for upper photospheric lines.

Solid figures: Data from Table I.

Open figures: Data from Table II, normalized to agree with Table I at offsets common to the two tables. (See footnote to Table II.)

We conclude our discussion of the instantaneous line-of-sight velocity field by an observation about the effect of the relatively strong magnetic fields in plage regions on the velocities. On plates taken in Ca 6103 and Na 5896, the rms velocity is reduced in size in plage regions, and the velocity structure is diffuse in appearance. (Cf. Fig. 3-1(b).) We are apparently seeing an inhibition of the motion due to the magnetic fields. The inhibition appears greatest both in magnitude and spatial extent in Na 5896. Figure 3-4 illustrates A-C curves corresponding to plage areas and non-plage areas on the Na 5896 Doppler plate of Figure 3-1(b).

#### B. Size of the Elements of the Velocity Field

It has already been mentioned that the elements in the small scale Doppler field vary in size from somewhat larger than that of the photospheric granulation at levels immediately above the granulation to several times the photospheric granulation at the level of the NaD line. It is somewhat difficult to describe this variation precisely, due to the fact that the apparent cell size depends strongly on the image quality of the plate being studied. Therefore, a collection of measurements of half-widths of A-C curves of singly cancelled Doppler plates will exhibit large variations between data from different sets of observations; the variations are considerably larger than half-width variations of different areas on the same plate. Nevertheless,

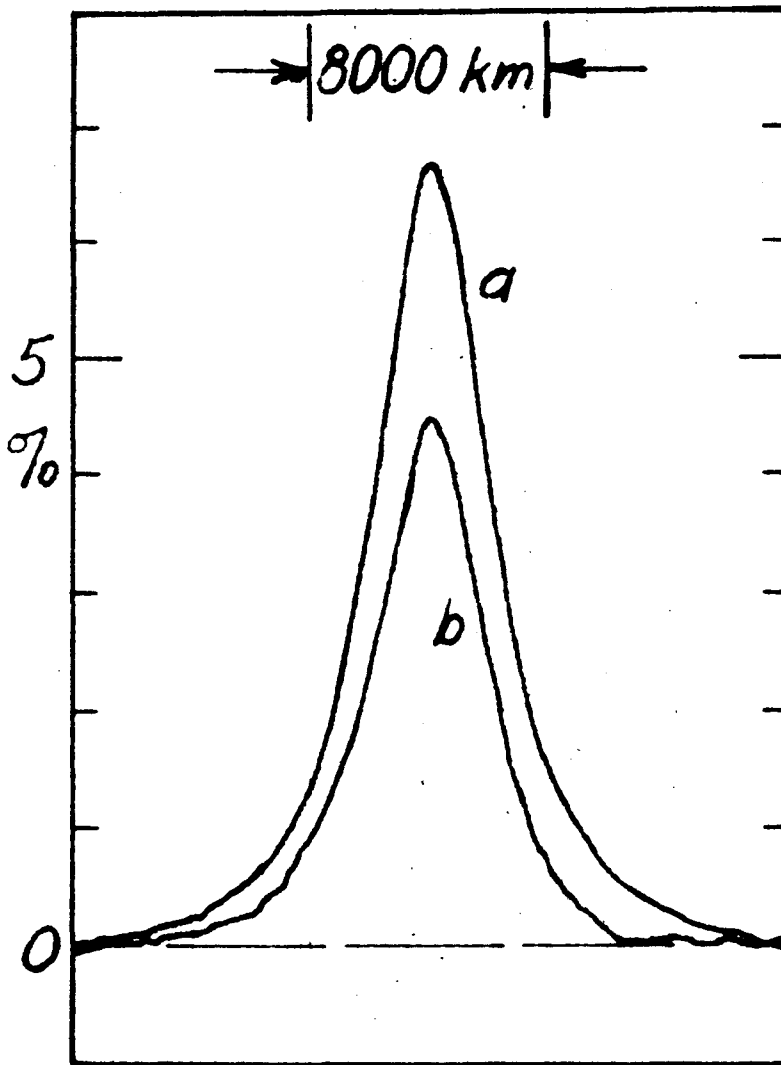


Figure 3-4. A-C curves of Na5896 velocity field, (a) outside plate and (b) inside plate. Plate is that illustrated in Figure 3-1(b).

by studying only those plates for which the seeing was exceptionally good, we find enough self-consistency in the different half-widths for given lines to have some confidence in the rather large variations of apparent cell size from line to line.

Figure 3-5 shows as crosses a plot of the full width at half maximum of A-C curves of Doppler plates of various spectral lines. The curves which were measured are similar to those illustrated in Figure 3-2. Also shown as dots are half-widths of A-C functions of the original images taken on either wing of the line. Each cross or dot represents the average of a number of A-C scans over several different areas on a set of plates from a single observational sequence. The ordinate is the half-width in units of km on the sun; the lines are arranged along the abscissa in the same way as Figure 3-3. In view of the fact that the total change in altitude of line formation between the Fe 6102 line and the Na 5896 line is probably not more than a few hundred km, i. e., less than the order of magnitude of the size of the cells themselves, the more than doubling of their size in such a distance as implied by Figure 3-5 is a very significant change.

It also appears from Figure 3-5 that the size of the velocity field for Fe 6102 and Ca 6103 is very nearly the size of the photospheric granulation field, as photographed in green light by the granulation camera at the 60 foot tower.\* This is scarcely surprising in view of

\* An exact comparison of the sizes of the elements in the two fields is impossible since the granulation camera has far better instrumental resolution than does the spectroheliograph.

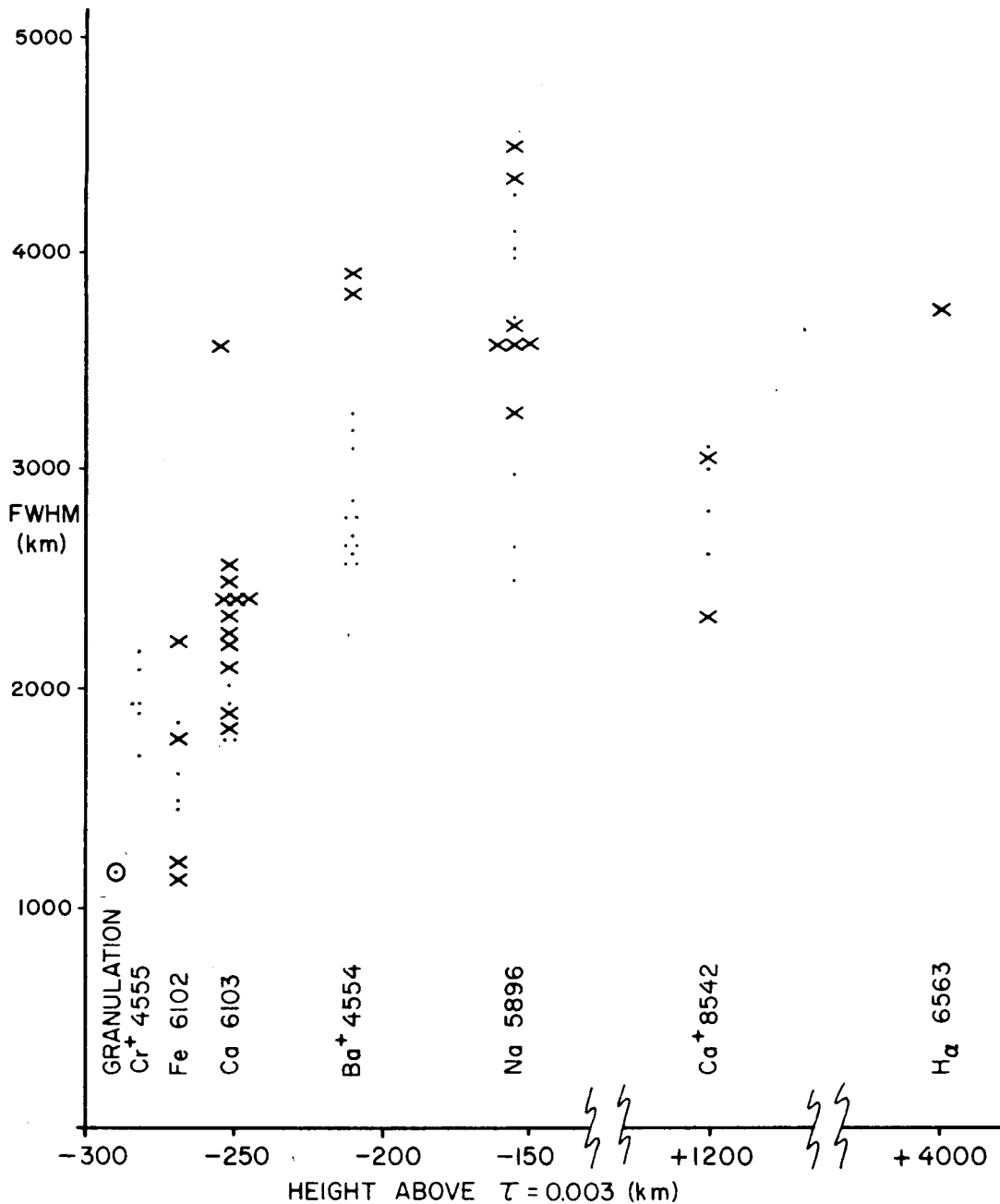


Figure 3-5. FWHM (km) versus height of formation for original images exposed on spectral line wings (dots) and Doppler plates (crosses). Also shown (circle) is the FWHM for a direct photograph of the solar granulation. (Heights of atmospheric lines  $\text{Ca}^+$  8542 and  $\text{H}_\alpha$  6563 are from De Jager (10).)

the close physical association of the velocity field at that altitude with the granulation field directly below. It should be pointed out that although all of the points on the figure represent plates of unusual image quality, the average image quality for Fe 6102 and Ca 6103 considerably surpasses that of the other lines. Therefore, the difference in half-width between these two lines and the higher lying lines represents an upper limit, and the true difference is quite probably somewhat less.

A few upper chromospheric lines are also included in Figure 3-5. The half-width for these lines represents a characteristic size of the velocity field at this altitude, but it should be recalled that this field is apparently uncorrelated with the granulation or the velocities at lower levels. Rather it is to be associated with the velocity structure of the "chromospheric mottling" visible on ordinary spectroheliograms, and discussed by DeJager (5). The size of this chromospheric velocity detail appears to remain roughly constant from the level of Na 5896 to the level of  $H\alpha$ .

### C. Variation of Line-of-Sight Velocity with Position on the Solar Disk

Near the center of the solar disk ( $\theta = 0$ ,  $\cos \theta = 1$ ) the observational line-of-sight coincides with the local vertical, and thus the Doppler shift technique is sensitive to only vertical, rather than horizontal, velocities. Near the limb of the sun ( $\theta = 90^\circ$ ,  $\cos \theta = 0$ ), the line-of-sight coincides with a local horizontal line, and the situation is reversed: only horizontal velocities can be detected.

Therefore, an analysis of the variation of line-of-sight velocity with  $\cos \theta$  will yield information on the relative sizes of the horizontal and vertical components of the velocity field.

For the lines Fe6102, Ca6103, and Na5896, such an analysis has been made. The plates used for this purpose included areas on the sun from the center nearly to the limb, and furthermore had exceptional image quality. On all of the plates the Doppler granulation can be observed to well past  $\theta = 45^\circ$ . In regions where  $\theta$  is larger than about  $30^\circ$ , there is some danger of confusing the Doppler granulation with the long-lived large cells of primarily horizontal motion discussed by Leighton et al. (2). However, the great difference in size between the two velocity fields does permit a separation of their contributions to the overall velocity field.

The method of analysis in all three lines was to mask off all the area on the singly cancelled plate except that within an annulus  $(\rho, d\rho)$  of width  $d\rho = d(R \sin \theta \sim 0.03R)$  centered at  $\rho = R \sin \theta$ . For each value of  $\rho$ , two A-C curves were run, one perpendicular to the limb, the other parallel. The heights of these A-C curves were measured with respect to a baseline chosen to intersect the A-C curve  $C(s)$  at a distance  $\pm s'$  from the central peak, where  $s'$  corresponds to 3 sec of arc (2400 km) for the Ca and Fe plates, and 7 sec of arc (5600 km) for the Na plate. This choice of baseline includes most of the contribution of the small-scale velocity field (2000 km for Fe and

Ca; 3500 km for Na) to the autocorrelation peak, yet eliminates most of the contribution of the large convective cells, whose size is measured (2) to be 14000 to 18000 km.

The velocity is derived from the height of the A-C curves measured in the above fashion by dividing the square root of the height by the logarithmic slope of the line profile as measured separately for each value of  $\rho$ :  $\langle v^2 \rangle^{1/2}(\rho) = \frac{c}{2\lambda} \frac{H^{1/2}(\rho)}{d \ln T(\rho) / d\lambda}$ . (See eq. 2.16, p. 27.)

The slope of the line profile is determined by two factors:

(1) the slope of the intrinsic solar profile, which decreases from center to limb of the sun, and (2) the curvature of the focal surface for spectral lines at the spectroheliograph, which causes the apparent slope of the line profile to decrease from the center to edge of the slit. The latter effect actually considerably exceeds the former and therefore the profile should be measured at the appropriate distance along the slit. On the plates used, however, the position on the slit varies over the annulus ( $\rho, d\rho$ ) of integration; at each value  $\psi$  of solar latitude the distance  $x$  along the slit from that point on the slit which scanned the center of the disk is given by  $x = \rho \cos \psi$ . Since a significant range of latitude was covered in the image, we measured the profile at that point  $\bar{x}$  which was the average position on the slit of points in the annulus:  $\bar{x}(\rho) = \frac{\int x(\rho, \psi) d\psi}{\int d\psi}$ .

To analyze the contribution of the horizontal and vertical components of velocity to the line-of-sight velocity, let us consider

the velocity field statistically to have a distribution function  $f(\underline{v})$ , i. e., if we assign to each resolvable element in the field a point  $(v_x, v_y, v_z)$  in velocity space, the density of points will be  $f(v_x, v_y, v_z)$ . Taking the z-axis to be in the direction of the local vertical, and the x-z plane to contain the line of sight, inclined at an angle  $\theta$  to the z-axis, we see that

$$v_{\parallel} = v_x \sin \theta + v_z \cos \theta. \quad (3.1)$$

Then

$$v_{\parallel}^2 = v_x^2 \sin^2 \theta + v_z^2 \cos^2 \theta + v_x v_z \sin 2\theta, \quad (3.2)$$

from which we determine

$$\langle v_{\parallel}^2 \rangle = \int v_{\parallel}^2 f(\underline{v}) dv_x dv_y dv_z. \quad (3.3)$$

If we make the plausible assumption that

$$f(v_x, v_y, v_z) = f(-v_x, v_y, v_z) \quad (3.4)$$

we have

$$\begin{aligned} \langle v_{\parallel}^2 \rangle &= \int v_x^2 \sin^2 \theta f(\underline{v}) d^3 v + \int v_z^2 \cos^2 \theta f(\underline{v}) d^3 v \\ &= \sin^2 \theta \langle v_x^2 \rangle + \cos^2 \theta \langle v_z^2 \rangle \end{aligned} \quad (3.5)$$

(It should be noted that this result is independent of any correlation between horizontal and vertical velocities; our assumption in equation 3.4 causes such correlations to cancel out in the averaging process of the A-C function integration.) If we now write

$$\cos^2 \theta = w, \quad \sin^2 \theta = 1-w, \quad (3.6)$$

equation 3.5 becomes

$$\langle v_{\parallel}^2 \rangle = w(\langle v_z^2 \rangle - \langle v_x^2 \rangle) + v_x^2 = aw + b \quad (3.7)$$

Therefore, we see that any velocity distribution  $f(v)$  should yield a linear relation between mean square line-of-sight velocity and  $w = \cos^2 \theta$ . The  $w = 0$  and  $w = 1$  intercepts should be the mean square horizontal and vertical velocities, respectively.

Accordingly, the measured line-of-sight mean square velocity,  $\langle v_{\parallel}^2 \rangle^{1/2}(\theta)$ , has been plotted versus  $w = \cos^2 \theta$ . This plot is shown in Figure 3-6. Also shown are the straight line least-square fits to the data,  $\langle v_{\parallel}^2 \rangle^{1/2} = a + bw$ . We may read the best fits to the mean square vertical and horizontal velocities from the intercepts at  $w = 1$  and  $w = 0$  (center and limb), respectively. The data for  $0 < \theta < 54^\circ$  were used in the least-square fit, weighted equally. The parameters  $a$  and  $b$  and the corresponding values of mean square horizontal and vertical velocity, as well as their ratio, are listed in Table III for the lines investigated.

Table III

Mean square horizontal and vertical velocities, determined from variation of  $\langle v_{\parallel}^2 \rangle$  with  $w = \cos^2 \theta$ ;  $\langle v_{\parallel}^2 \rangle = aw + b$ .  $a$  and  $b$  are determined from least square fits of the data plotted in Fig. 3-6.

Line	$a(\text{km/sec})^2$	$b(\text{km/sec})^2$	$\langle v_h^2 \rangle$ (km/sec) <sup>2</sup>	$\langle v_v^2 \rangle$ (km/sec) <sup>2</sup>	$\langle v_h^2 \rangle / \langle v_v^2 \rangle$
Fe6102	.25±.02	.09±.04	.25±.02	.34±.06	.73±.16
Ca6103	.13±.01	.08±.01	.13±.01	.21±.02	.62±.04
Na5896	-.04±.03	.51±.04	-.04±.03	.47±.05	-.09±.08

51a

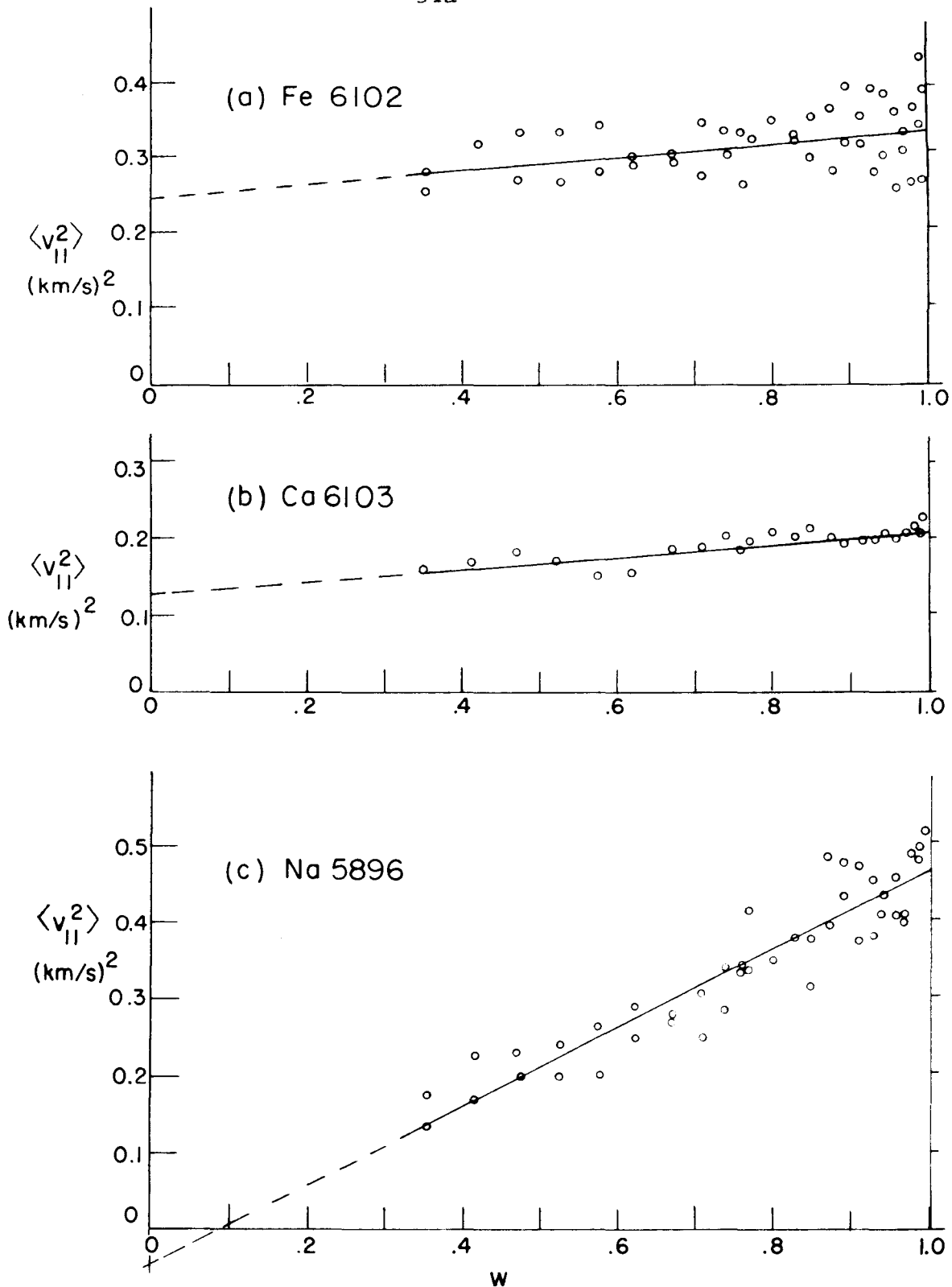


Figure 3-6. Mean square line-of-sight velocity  $\langle V_{||}^2 \rangle$ , as measured at various values of  $\theta$ , for three spectral lines. Abscissa:  $w = \cos^2\theta$ . Intercepts at  $w = 0$  and  $w = 1$  are  $\langle V_{\text{horiz}}^2 \rangle$  and  $\langle V_{\text{vert}}^2 \rangle$ , respectively.

The individual magnitudes of the horizontal and vertical velocity components listed in Table III do not have any more validity than any of the individual measures which contributed to Table I, for both are subject to calibration errors in the line profile measures and to the image quality on the particular plate analyzed. However, the ratio of the horizontal to the vertical velocity components, given in the last column, should be independent of calibration errors and of variations in image quality. Therefore, except for possible instrumental effects which vary from center to limb, and which we shall shortly discuss, the last column should represent with some reliability the actual situation on the sun. This situation, as implied by the table, is that in the lower lying levels of formation of the Fe and Ca lines, presumably immediately above the level of the photospheric granulation, the horizontal component of mean square velocity is nearly as large as the vertical. However, at the level of formation of the Na 5896 line, at least several hundred km above the granulation, the velocities are substantially vertical only. Part of the change in the ratio is due to the increase of vertical velocity with height which we have already encountered (p. 43 ), but it appears also that the horizontal velocity decreases with height. The deviations in the measured values for Fe6102 and Ca6103 are sufficient to mask any difference between those two lines.

There are four factors which might complicate the above interpretation of the data, and which must be examined. They are:

- 1) As described in Part I, the spatial resolution is somewhat poorer near the ends of the slit than near its center due to the curvature of field of the spectroheliograph. This might cause measured velocities to be too low near the edges of the cancelled image, because there the smaller velocity elements are less well resolved.
- 2) Since the cell size might be expected to drop off toward the limb due to foreshortening, and since the resolution worsens as the cell size decreases, the measured velocities might be too low near the limb.
- 3) The horizontal motions in the large cells, being not completely separated from the small-scale field, might contribute to the measured small-scale field in an amount which increases toward the limb.
- 4) Due to the rise of height of formation of a spectral line near the limb, coupled with the observed increase of velocity with height, the observed velocities might be slightly too high near the limb.

Due to a fortuitous combination of circumstances, none of these considerations affect our major conclusion, which is that although the velocity field has a sizeable horizontal component at lower levels, this is much less or even essentially disappears at the higher level of the Na 5896 line. The first three factors can only act to make the observed decrease of horizontal velocity with height smaller than the true decrease, and the fourth is negligible. We see this in the following way:

- 1) Because the Fe and Ca Doppler cells are smaller in size than the Na cells, the decrease in measured velocity near the edges of the image due to curvature of field in the spectroheliograph will be greater for the Fe and Ca lines than the Na line.
- 2) For the same reason, the decrease in resolution due to foreshortening near the limb must decrease the measured velocities in the Na line less than those in the Fe or Ca lines.
- 3) Because the size of the Na Doppler cells is more than twice the size of the Ca and Fe Doppler cells, it is more difficult to separate the Na small scale field from the Na large cells than to make a similar separation for Fe and Ca. Therefore, the influence of the large cells, i. e., the increase of measured velocity toward the limb, will be greatest for Na.
- 4) The height of formation of a spectral line increases significantly toward the limb only if there is a large temperature gradient. At the level of observation, the solar temperature is approaching a minimum, and the gradient is small enough that the change of height of formation with  $\mu$  is unimportant (6).

The only remaining qualification necessary is to note that our conclusion--that although the horizontal and vertical components of the velocity field are comparable at lower levels, the horizontal component decreases with altitude while the vertical component increases, until the velocities are substantially vertical at higher

levels--is based on only three plates. More observations are badly needed to put this conclusion on firmer ground. The observations, however, are in agreement with other observers, notably Evans and Michard (6), who also find that there is a marked increase of vertical velocity with altitude, with a concomitant slight decrease of horizontal velocity.

#### D. Oscillatory Motions as Revealed by the Time Dependence of the Velocity Field

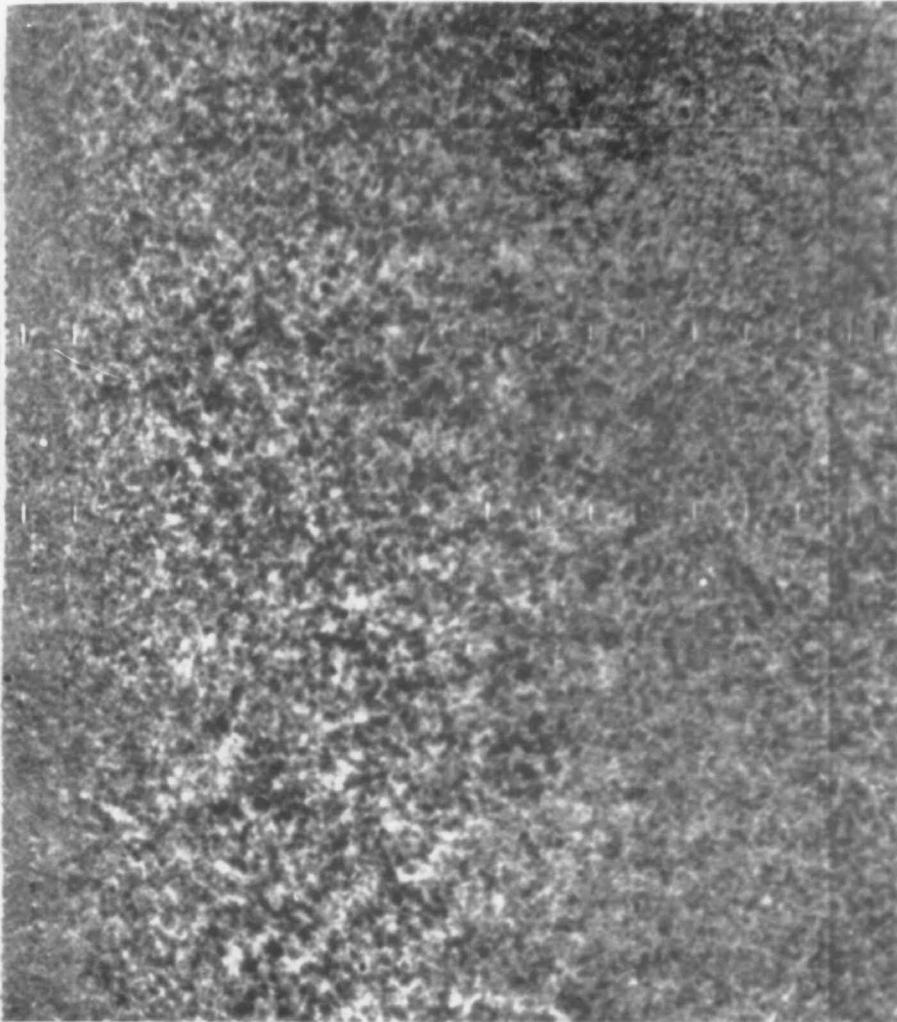
It will be recalled that a fluctuation in transmission at any point of a Doppler difference (or sum) plate is directly proportional to the difference (or sum) of the velocities at that point as observed at two times separated by  $\Delta t$ , where  $\Delta t$  varies linearly from nearly zero at one end of the image to several minutes at the other end. Thus the mean square fluctuations of transmission, which are qualitatively appreciated as "contrast," and which may be quantitatively measured as the height of an A-C function of the transmission field, are related to the correlation of the velocity field with itself after a time interval  $\Delta t$ .<sup>\*</sup> If there were no time correlation of the velocity field, i. e., if the velocity at a point were a random function of time, the contrast would be uniform all over the plate. If (as originally expected) the velocity at a point gradually evolved in time with a

\* If the transmission of a Doppler plate is (eq. 3.8)  $T_D = T(1 + \delta(x, y, t(x)))$  the transmission of the Doppler sum or difference plate is (eq. 3.9)  $T_{D\delta} = T'(1 + \delta(x, y, t(x)))$  and the mean square fluctuation of transmission is (eq. 3.10)  $H_{\delta} = 2\langle \delta^2(x, y) \rangle + 2\langle \delta(x, y, t)\delta(x, y, t + \Delta t) \rangle$ . Equation 3.10 results from equation 3.9 if we assume statistical stationarity in time.

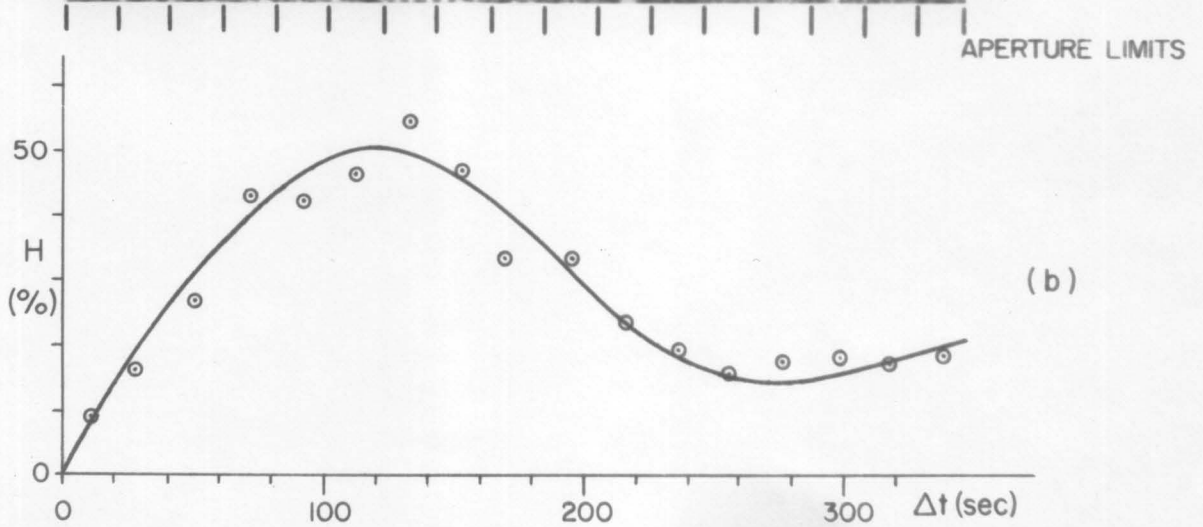
lifetime  $\tau$  for changes in velocity comparable to the velocity itself, the time correlation would decrease with a lifetime  $\tau$ , and in a Doppler difference (sum) plate, the "contrast" would increase (decrease) with the same lifetime. It would be reasonable to expect the lifetime  $\tau$  to approximate the observed lifetime of a few minutes for decay of the time correlation of the photospheric granulation field.

An actual Doppler difference plate is shown in Figure 3-7(a). It is seen that the behavior of the contrast is quite different from that just described. Near  $\Delta t = 0$ , the contrast does increase with  $\Delta t$ , but at  $\Delta t \sim 150$  sec it reaches a maximum, and decreases to a minimum near  $\Delta t = 300$  sec. This is followed by another maximum and minimum of contrast at  $\Delta t \sim 450$  and  $600$  sec, respectively, on plates whose scanning speed is sufficiently slow to permit observation of these longer time lags.

The existence of a minimum of contrast on a Doppler difference plate, i. e., a minimum in the mean square velocity difference, at  $\Delta t \sim 300$  sec,  $600$  sec, etc., can only mean that the velocity field tends to repeat itself after this time. Thus we conclude that the vertical velocity field contains a strong quasi-oscillatory component, with an "average period"  $T$  of about five minutes. The fact that the contrast at the  $\Delta t \sim 300$  sec minimum is only slightly greater than that at  $\Delta t \sim 0$  sec leads us to suspect that the oscillatory component may constitute the major part of the vertical velocity field.



(a)



(b)

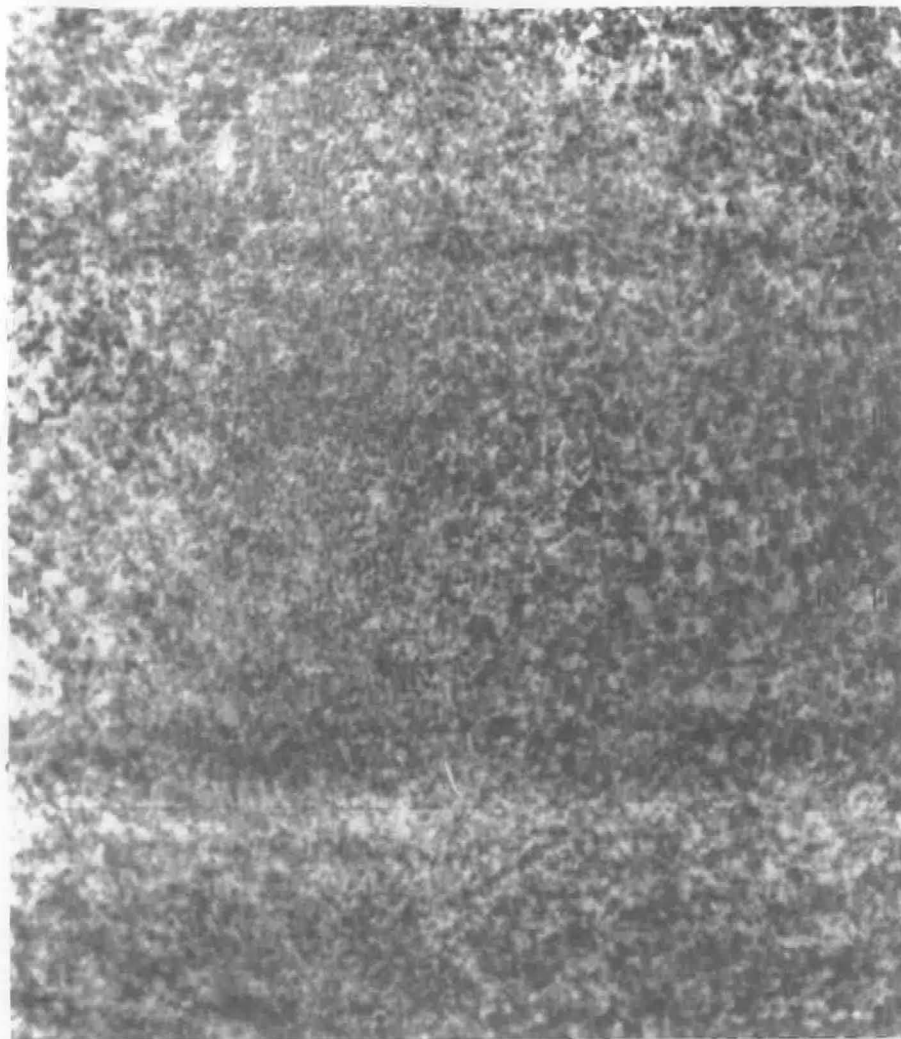
Figure 3-7. (a): Doppler Difference Plate,  $Ba^+ 4554$ , 7-1-61.  
 (b) Heights of A-C curves averaged over long narrow areas whose width is bounded by vertical lines at bottom of plate. Time lag increases from left to right.

Figure 3-7(b) shows the heights of A-C functions integrated over long narrow areas with the long axis parallel to the slit, i. e., areas where  $\Delta t \sim \text{const}$ . The height of the A-C functions is a quantitative measure of the mean square fluctuation of velocity, and of the time correlation of the velocity fields.

A Doppler sum plate is illustrated with the corresponding plot of mean square fluctuation of transmission in Figure 3-8. The contrast and mean square fluctuation is seen to pass through a minimum at  $\Delta t \sim 150$  sec and a maximum at  $\Delta t \sim 300$  sec. The fact that the sum of the velocity fields after one-half period of the oscillation is very nearly zero (as evidenced by the low contrast of Figure 3-8(a) and the low mean square velocity amplitude in Figure 3-8(b) for  $\Delta t \sim 150$  sec) leads us to conclude with some confidence that practically the entire vertical velocity field is oscillatory in nature.

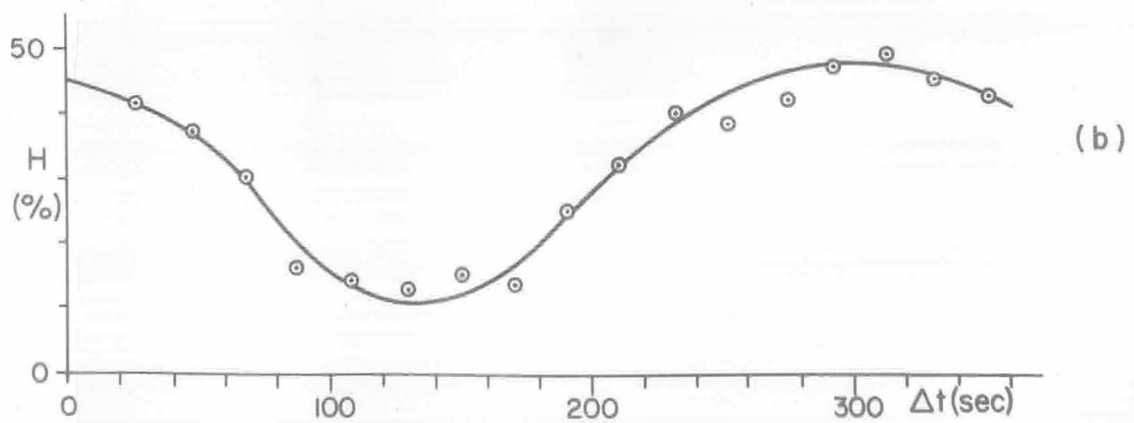
#### E. Determination of the Average Period of the Oscillation and Its Variation with Altitude

Experience with preliminary estimates of the oscillation period on twenty plates taken in the Ca6103 line in 1960 has shown that rough visual estimates of the position of minimum contrast on the Doppler difference plates yield remarkably consistent results for the average period. Not only are different visual estimates self-consistent, but they also agree closely with the minimum of the corresponding time correlation curve (Figs. 3-7(b), 3-8(b)) obtained



(a)

APERTURE LIMITS



(b)

Figure 3-8. (a): Doppler Sum Plate,  $Ba^+ 4554$ , 7-1-61.

(b) Heights of A-C curves averaged over long narrow areas whose width is bounded by vertical lines at bottom of plate. Time lag increases from left to right.

with the A-C machine. Therefore, for the purpose of a more detailed investigation of the average period and its variation from line to line, it was decided to use visual estimates, which give results similar to those from the much more laborious A-C curve tracing process. Because of the simplicity of the visual estimation method, a large number of plates could be analyzed without an impractical expense of labor.

Although it is difficult on a single plate to determine the position of minimum or maximum contrast precisely (indeed the position of minimum or maximum contrast may not be well defined), it is relatively easy to determine it to within perhaps  $\pm 10\%$  of the distance to the  $\Delta t \sim 0$  end of the image; the standard deviation of a single estimate from the mean of many estimates of the period usually turns out to be between 5 and 10 percent. A set of  $n$  independent observations will produce a mean whose standard deviation from the population mean is  $\frac{1}{\sqrt{n}}$  times as large. For example, each of the 20 visual observations of 1960 Ca6103 plates reported by Leighton et al. (2) had a standard deviation of about 5 percent, leading to a period estimate with a standard deviation of one percent. The massive statistics offered by estimates from many plates allows us to extract relatively precise numbers from a collection of relatively imprecise individual measures.

Therefore, a systematic visual study of many plates of

different spectral lines was undertaken, in order to determine the average period more precisely and to search for variations from line to line. The lines Fe102, Ca6103, Mg5528, Ba<sup>+</sup>4554, Na5896, Mg5173, and Ca<sup>+</sup>8542 were studied. All plates obtained in 1960 and 1961 which satisfied the following basic criteria were selected: (a) good image quality, (b) location of the minimum or maximum to be measured not too near the limb of the sun or the end of the plate, (c) good centering of the spectral line, (d) relatively free of sunspots and plages, and (e) no large guiding errors. The selected plates included both sum and difference pairs, with widely varying scanning speeds.

All of the plates underwent a first cancellation, and the individual cemented image pairs were projection printed. A contact print was made of one pair and this was superimposed on the other to form a second cancellation. This second cancellation was not cemented, in order that the observer be allowed to bring the two prints in and out of register at will. (This freedom is of some help in estimating the minimum of contrast when the plates are in register, as the contrast decreases sharply at a minimum and nowhere else as the plates are brought into register.)

On each plate, independent estimates of the position of all minima and maxima observed were made by three observers

separately (R. B. Leighton, G. W. Simon and R. W. Noyes). These observations were made without prior knowledge of the scanning speed or time delay between successive spectroheliograph scans; thus there was no way of knowing ahead of time the value of  $\Delta t$  to which any estimate corresponded.

In addition, the observers accompanied each estimate with a weighting factor, equal to 1, 2, 3, or 4. These purely subjective weighting factors served to separate the estimates into groups of different reliability, and reflected such things as the degree of cancellation at a minimum or reinforcement at a maximum, the sharpness with which the minimum or maximum was approached from either side, whether there were sunspots or plages in the region of minimum or maximum, whether the minimum or maximum occurred too close to the limb of the sun or to the edge of the plate, etc.

For each estimate, the value of that fraction of a period to which it pertained ( $\frac{T}{2}$ ,  $T$ ,  $\frac{3T}{2}$ , etc.) was calculated by the equation  $\frac{nT}{2} = D \left( \frac{1}{v_1} + \frac{1}{v_2} \right) + \Delta$ , where  $D$  is the distance from the  $\Delta t \sim 0$  end of the plate to the estimated minimum or maximum,  $v_1$  and  $v_2$  are the velocities of the spectroheliograph during the two scans, and  $\Delta$  is the time which elapsed between the scans. The individual estimates for the various lines are plotted in Figure 3-9.

For each line, and each value of  $n$ , the estimates of  $\frac{nT}{2}$  within each weight group were averaged and their standard deviations

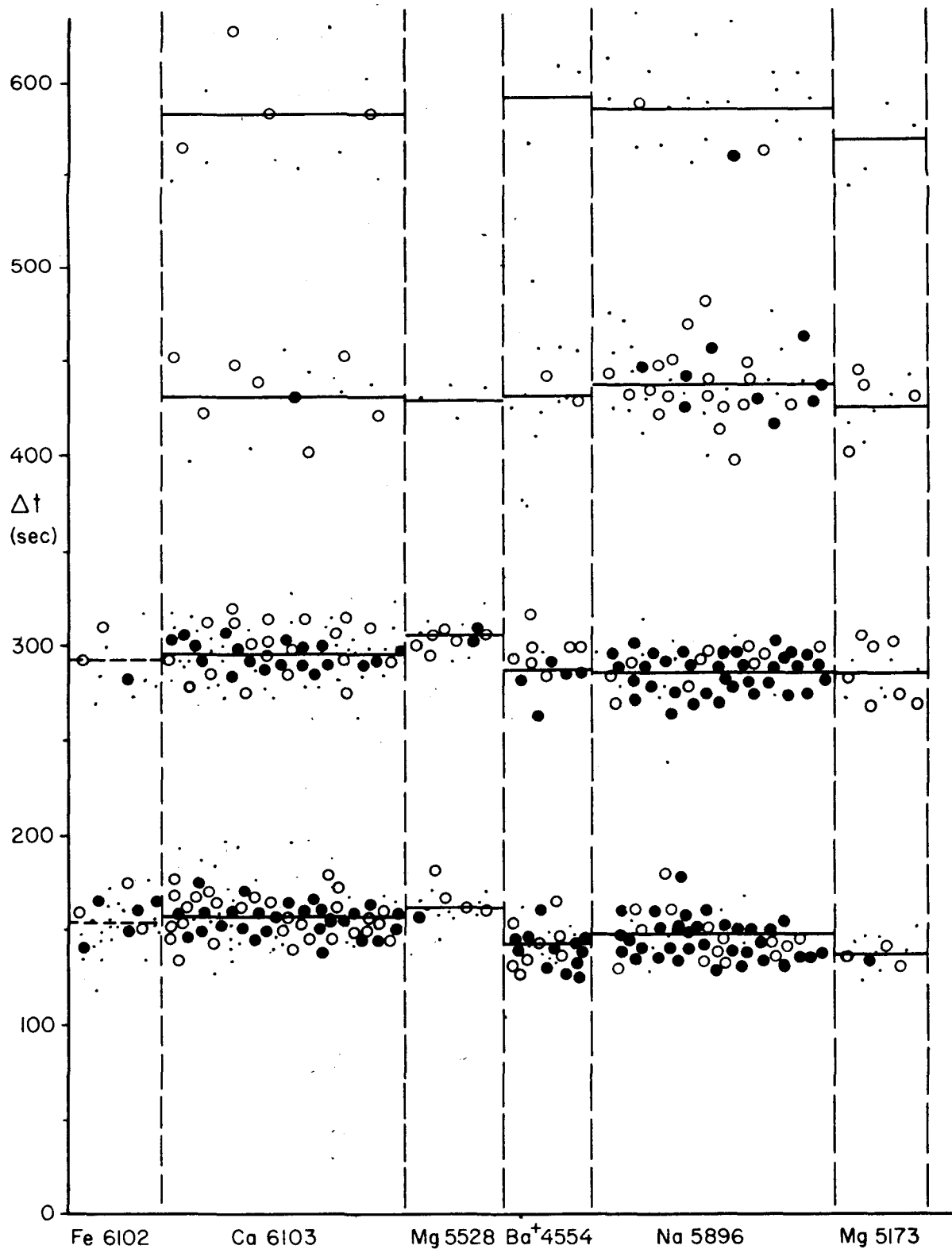


Figure 3-9. Individual estimates of average values of  $T/2$ ,  $T$ ,  $3T/2$  and  $2T$ .  
 Dots: weight 1 or 2; open circles: weight 3; closed circles: weight 4. Horizontal lines: weighted averages from Table IV.

found. It was noted that in almost every case the groups with higher weights had a smaller standard deviation than those with lower weights, thus verifying that the weights were indeed meaningful. In the very few cases where a group with a lower weight also had a lower standard deviation, it was combined with the next higher group, reaveraged, and a new standard deviation obtained. This was also necessary because in these cases the individual groups usually had only a few members, and thus the individual standard deviations were not meaningful. Following this procedure, the grand average of the results from each weight group was obtained using as weighting factors the reciprocals of the square of their standard deviations (9). The standard deviation of the entire set was computed using  $\frac{1}{\sigma^2} = \sum_i \frac{n_i}{\sigma_i^2}$ ,  $i = 1, 2, 3, 4$ , where  $\sigma_i$  is the standard deviation of the  $i^{\text{th}}$  group, which contains  $n_i$  estimates. If  $t_{ij}$  is the  $j^{\text{th}}$  estimate in the  $i^{\text{th}}$  weight group,  $\sigma_i^2 = \frac{1}{n_i - 1} \sum_j (t_{ij} - \bar{t}_i)^2$ . The results of this procedure are given in Table IV, and are graphed for T/2 and T in Figure 3-10.

The first impression from Figures 3-9 and 3-10 is that the period is roughly the same for all lines observed. The scatter of the individual estimates shown in Figure 3-9 seems to mask possible variations of average period from line to line. However, examination of Table IV reveals that the average period for the two lines Ca 6103 and Na 5896 is remarkably well-determined, due to the large number of estimates made. (A good indication of the reliability of a particular average, aside from its standard deviation, is the total weight  $\Sigma W$ , listed in

TABLE IV

Estimates of Average Velocity Period for Various Spectral Lines

Time Interval	Line	No. of Plates	No. of Estimates	$\Sigma W$	Average Time (sec)	$\sigma$ (sec)
T/2	Fe6102	10	29	68	151.5	2.2
	Ca6103	30	88	255	157.7	1.3
	Mg5528	6	16	39	163	4
	Ba <sup>+</sup> 4554	10	29	92	142	2
	Na5896	20	57	198	157.0	1.5
	Mg5173	4	12	27	138	2
T	Fe6102	5	10	22	289	6
	Ca6103	31	77	191	296.1	1.3
	Mg5528	6	17	48	303	2
	Ba <sup>+</sup> 4554	8	22	59	288	3
	Na5896	20	55	186	285.8	1.5
	Mg5173	4	12	31	285	4
$\frac{3T}{2}$	Ca6103	7	14	34	432	6
	Mg5528	3	4	4	431	16
	Ba <sup>+</sup> 4554	5	14	27	431	9
	Na5896	16	46	125	439	3
	Mg5173	4	10	23	425	5
2T	Ca6103	6	11	21	583	9
	Ba <sup>+</sup> 4554	2	3	3	590	30
	Na5896	12	22	33	588	4
	Mg5173	3	4	5	567	10

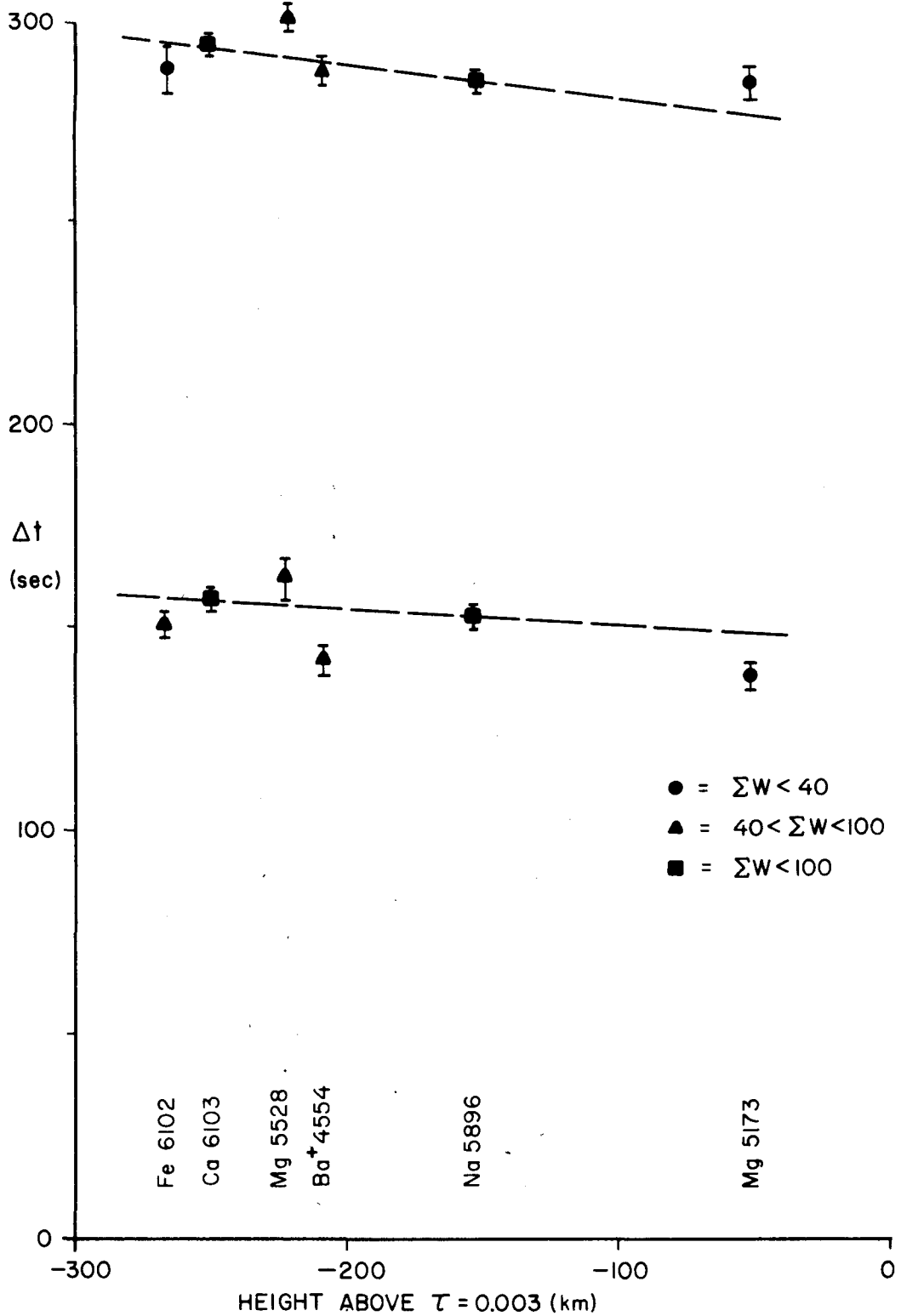


Figure 3-10. Estimates of  $T/2$  and  $T$  for six spectral lines, from Table IV. The lines are arranged according to approximate heights of formation. Dashed lines are fitted to the values for Ca 6103 and Na 5896.

column five of Table IV, i. e., the sum of the weights assigned to the individual estimates.) The average period for Ca 6103 is 296 sec; for Na 5896 it is 286 sec. This implies a slight but definite decrease in average period from the weaker and lower-lying (6103) line to the stronger and higher-lying (5896) line, i. e., a decrease of period with height. Such a conclusion is borne out by the other lines studied: the higher-lying (Ba 4554, Mg 5173, and Na 5896) lines tend to have a shorter average period  $T$  than the lower-lying (Fe 6102, Ca 6103, Mg 5528) lines.

We shall briefly discuss three apparent exceptions to this tendency: (a) Mg 5528 is slightly stronger than Ca 6103 and therefore might be expected to have a shorter period instead of a longer period, as observed. The average period, however, is based only on two sets of observations, and lacks good confirmation. Furthermore, we have already mentioned that the exact ordering of lines with altitude by their strength or residual intensity is an uncertain procedure. (b) Fe 6102, which, because it is considerably weaker than Ca 6103 and has a higher excitation potential, is almost certainly formed at a lower level, has nevertheless a shorter average period than Ca 6103. It is also very difficult to observe the oscillation for longer than one period in this line; i. e., the "lifetime" of the oscillation may be shorter at this level than at higher levels (See Fig. 3-12, next section). Perhaps this could be due to such a low-lying line being more closely associated with the turbulent motion of the granulation, which would destroy the periodicity. As we shall see later (p. 95), a rapid decay of the oscillation will cause the observed average period to be too short. (c) For the longer time intervals  $\frac{3T}{2}$  and  $2T$ , the trend of period with height seems, if

anything, to be reversed. But we see from Table IV that our statistics are not reliable enough to justify any conclusion for these longer time intervals.

Finally, we should note that the "average" period we have measured is the period of the spatially averaged time correlation function of the velocity field. The small dispersion of the measures of this period should not be taken to imply that the dispersion of the oscillation period of individual elements in the velocity fields is also small. The present measurements can make no statement about the period of individual elements, except that they combine to form a well-defined average period which seems to decrease with height.

#### F. Lifetime of the Oscillation

The oscillatory motions have been followed through at least three full periods on Doppler difference plates made with very slow scanning speeds. However, the amplitude of the oscillation of the time correlation function appears to decay rather rapidly with time delay  $\Delta t$ , and it is difficult to follow the oscillation for more than two or three cycles on a normal difference or sum plate.

For large time delays, it is desirable to analyze a Doppler difference or sum plate for which the time delay is constant over a large area, in order to obtain better statistics. Therefore, sets of difference plates were scanned in the same direction, separated by various time intervals. Because the two images were scanned in the same direction at the same speed, the time delay is constant over the entire plate.

Sets of such scans were obtained for the lines Fe 6102, Ca 6103,

and Na 5896, with time delays of  $\Delta t = \frac{T}{2}, T, \frac{3T}{2}, \dots$  where  $T = 296$  sec. A-C curves of Doppler difference plates in Ca6103 with various time delays are graphed in Figure 3-11.

In Figure 3-12(a) the peak heights of such A-C curves are shown as a function of time delay  $\Delta t$ , expressed in units of the period  $T$ . It is seen that the characteristic maxima and minima of the oscillation may be followed out to at least three periods.

If we assume that the peak height of the A-C function varies sinusoidally in  $\Delta t$  with a period of five minutes, and with an exponentially decaying amplitude, we may estimate the mean life  $\tau$  of this "damped oscillation" by expressing the height of the A-C function as

$$H(\Delta t) = A e^{-\Delta t/\tau} (1 - \cos \omega \Delta t) = A e^{-nT/\tau} (1 - \cos n\pi T) \quad (3.11)$$

where  $n$  is the number of oscillations,  $T$  is the period, and  $\tau$  is the mean life of the oscillation.

Figure 3-12(b) shows semilog plots of  $|H(\frac{n}{2}T) - H(\frac{n-1}{2}T)|$  for the data of Figure 3-12(a). From the slopes of the two lines shown, which correspond to mean lives of 320 and 440 sec, we conclude that the data for the three lines Fe6102, Ca6103, and Na5896 are all consistent with a mean life  $\tau \sim 380$  sec.

We should point out that two sources can contribute to the decay of the time correlation function: a) actual loss of energy in the oscillating elements, i. e., damping, and b) changes of phase of the oscillating elements, which destroy the correlation. We shall discuss this point again later.

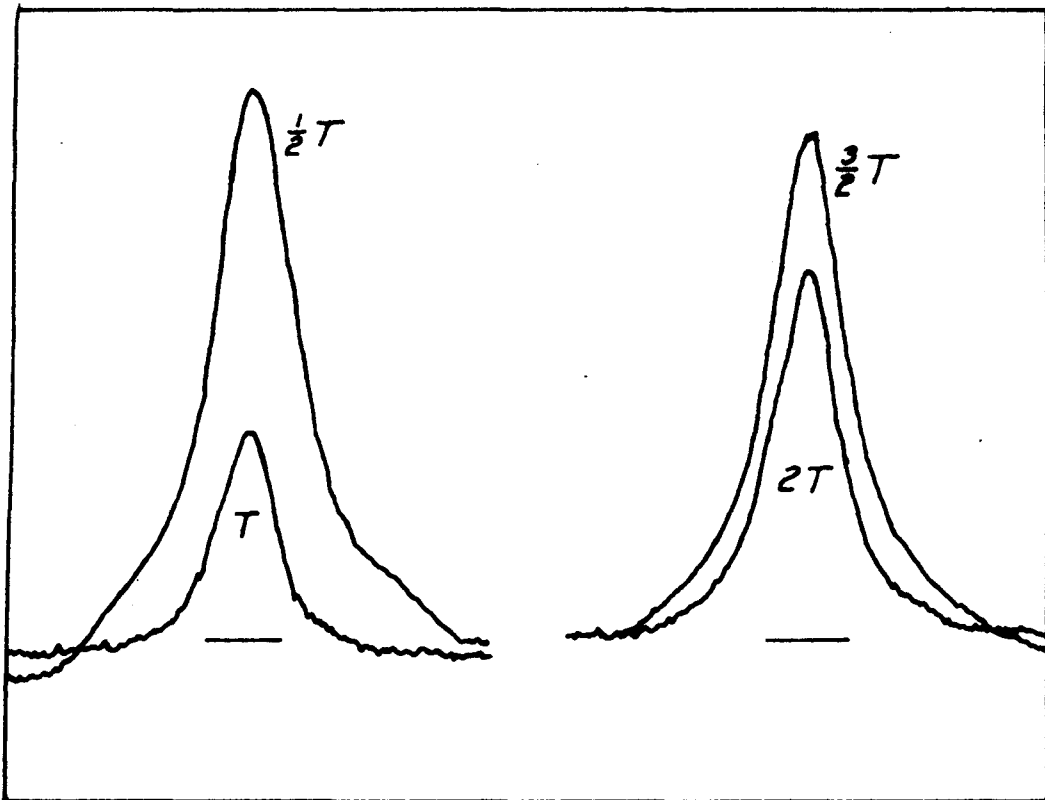


Figure 3-11. A-C curves for Ca6103 Doppler difference plates for which the time delays are constant over the entire plate and have the values  $T/2$ ,  $T$ ,  $3T/2$ ,  $2T$ . These curves show that at integral periods the curves are both less high and narrower than at half-integral periods.

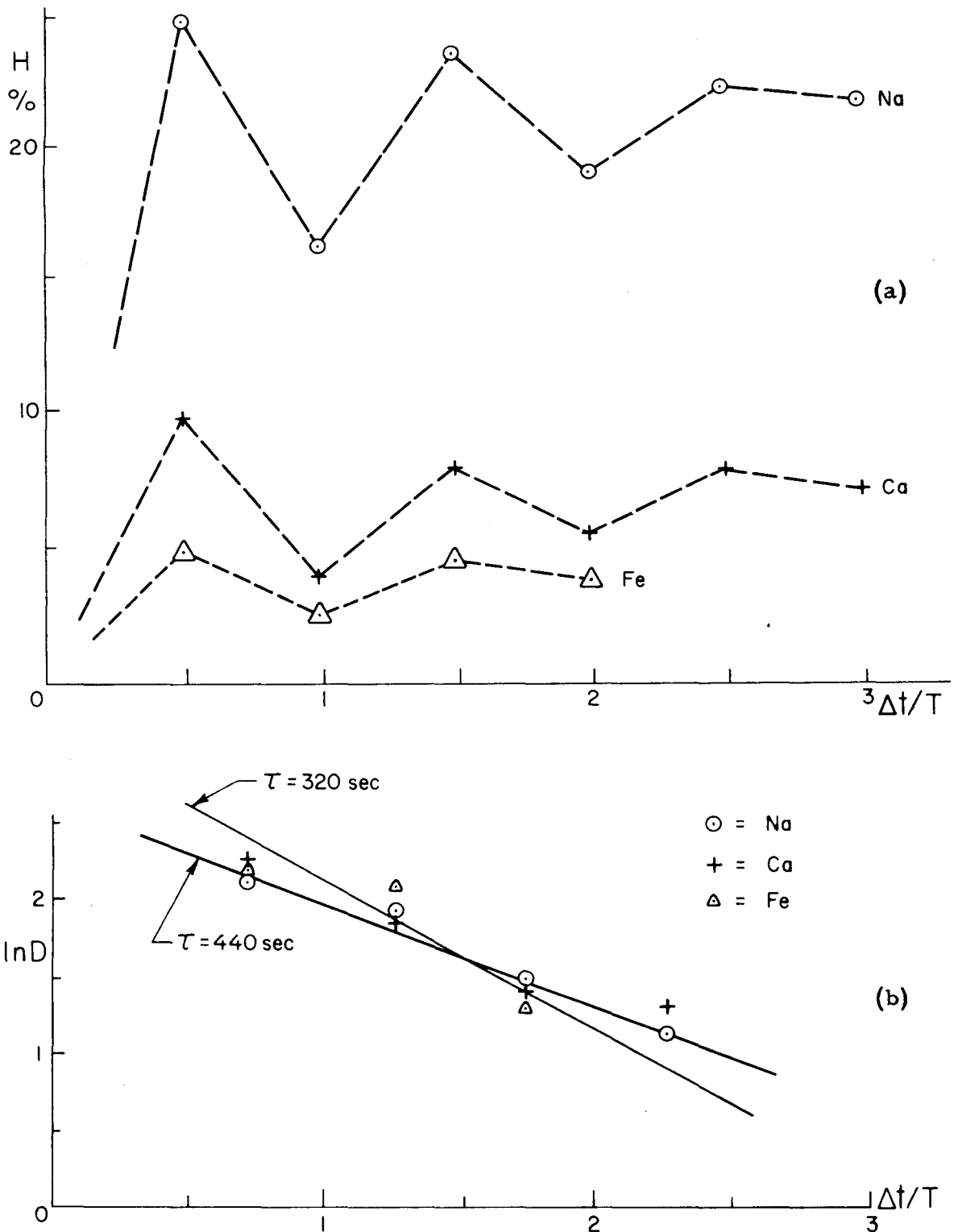


Figure 3-12. (a) A-C heights versus  $\Delta t/T$  for Fe6102, Ca6103, and Na5896. (b) Semilog plot of successive differences  $D$  in peak height versus  $\Delta t/T$ . The mean decay time is  $\tau \sim 380$  sec.

**G. Relative Sizes of Oscillatory and Non-Oscillatory Components  
of the Velocity Field**

From Figure 3-11 it is apparent that the full width at half maximum (FWHM) of the A-C curves of Doppler difference plates is greatest for time lags of  $1/2T$  and  $3/2T$ , i. e., when the oscillatory fields reinforce. Doppler sum A-C curves exhibit the greatest FWHM at time lags of  $T$  and  $2T$ , again when the oscillatory fields reinforce.

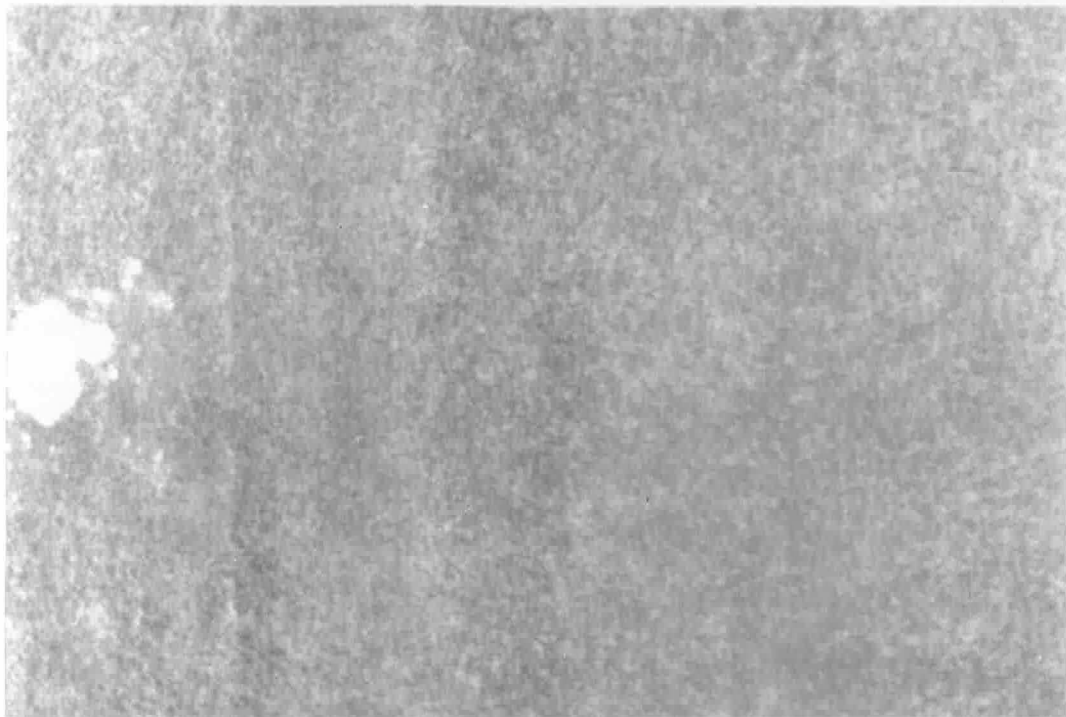
This behavior suggests that the size of the elements of the oscillatory velocity field is greater than the size of non-oscillatory elements. When on a Doppler sum or difference plate the oscillatory fields reinforce, they dominate the velocity sum or difference field, and the larger FWHM of the A-C curve is therefore primarily due to them. On the other hand, when the time lag is such that the oscillatory components cancel, the short-lived and non-periodic components dominate, and the smaller FWHM of the A-C curve is therefore primarily due to these components.

We have already seen (p. 57) that almost the entire contribution to the rms velocity is oscillatory. Thus we may conclude that the elements of the oscillatory field are larger both in size and in velocity amplitude than the non-oscillatory components. A part, but certainly not all, of the "non-oscillatory component" is actually photographic "noise"--grain, spurious signals due to imperfect

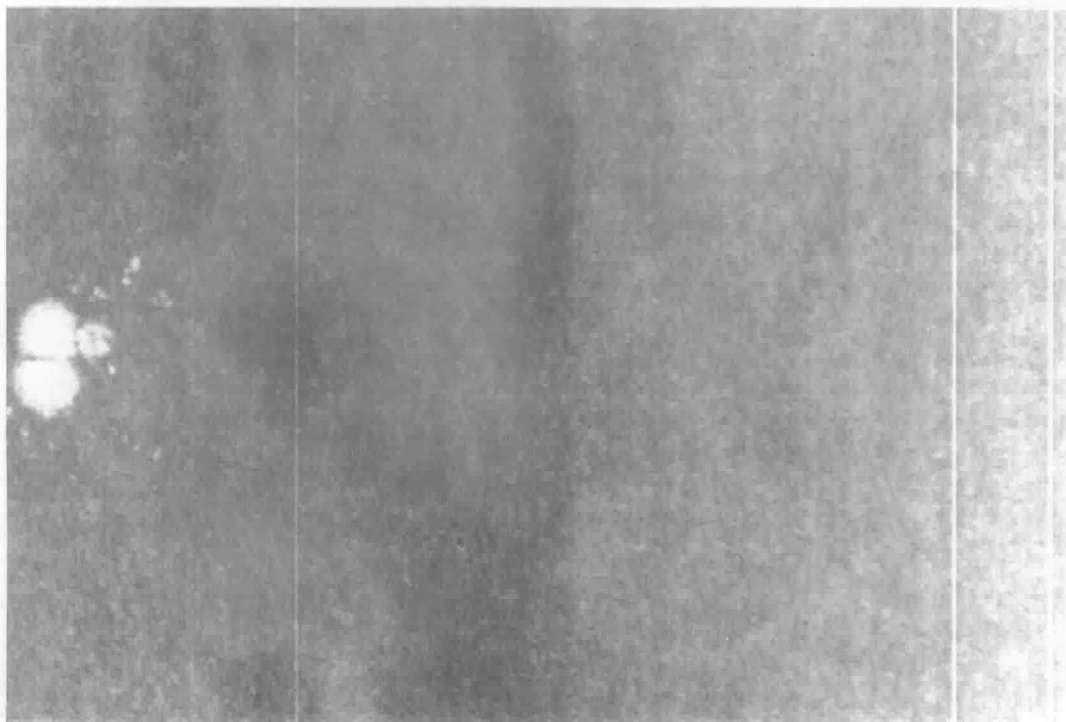
cancellation, etc. --which is masked by the much larger oscillatory component when the latter reinforces. We may take the observed variation of halfwidth illustrated in Figure 3-11 to be an upper limit to the true situation it represents.

#### H. The Brightness-Velocity Correlation

It will be recalled that the two original spectroheliograph images which are cancelled to bring out the Doppler field are identical except that one was exposed on the red wing of the spectral line and the other an equal distance from the core on the violet wing. When two such images exposed on the wings of the Ca6103 line are compared with each other, a striking difference between them is immediately apparent. Although both images were exposed over the same area at the same time, and show identical detail, the image exposed on the red side of the line invariably has more "contrast" than that exposed on the violet side; i. e., light areas are lighter and dark areas are darker. This effect is illustrated in Figure 3-13. We interpret the contrast difference in Ca6103 as being due to a local correlation between brightness and velocity, such that brighter-than-average areas tend to be associated with upward velocities, and darker areas with downward velocities: On the red side of the line, the variations in the light transmitted by the slit resulting from the local Doppler shifts and variations due to intrinsic brightness fluctuations tend to reinforce, while on the violet side of the line they tend to cancel. The effect is



(a)



(b)

Figure 3-13. Simultaneous spectroheliograms taken (a) on the red wing and (b) on the violet wing of the line Ca 6103. The greater "contrast" of image (a) implies a positive correlation between increased brightness and upward velocity.

so marked that even a previously uninformed observer can easily identify to which side of the line each image corresponds.

The line Fe6102 shows a brightness-velocity correlation of the same sign as Ca6103. This line is somewhat weaker than Ca6103 and has a higher excitation potential, and hence is formed at a lower level in the atmosphere.

A weaker correlation, but of the same sign, is also found in the strong NaD<sub>1</sub> ( $\lambda$ 5896) line wing for offsets greater than about 0.15 Å from the line core. However, plates taken less than about 0.12 Å from the line core show a reversed correlation: at these heights brighter-than-average areas are associated with downward velocities. Observations in Mg 5173 and Ca<sup>+</sup> 8542 show that the correlation remains reversed for still higher levels in the atmosphere.

These conclusions can be drawn from visual inspection, as just described, but we may also analyze the situation quantitatively with autocorrelation techniques. Figure 3-14 shows A-C and C-C curves of images taken near the center of the solar disk, on the red and violet sides of the lines Fe 6102, Ca 6103, Ba<sup>+</sup> 4554, Na5896, and Ca<sup>+</sup> 8542. The height of the peak of each A-C curve gives the mean square transmission variation on the plate, which is a quantitative measure of the "contrast." The lines are arranged in order of increasing altitude in the solar atmosphere. It is seen that for curves (a-d) the red side of the line has the higher A-C height, while for (e) and (f) the violet side has the higher A-C height, in agreement with the visual observations just discussed.

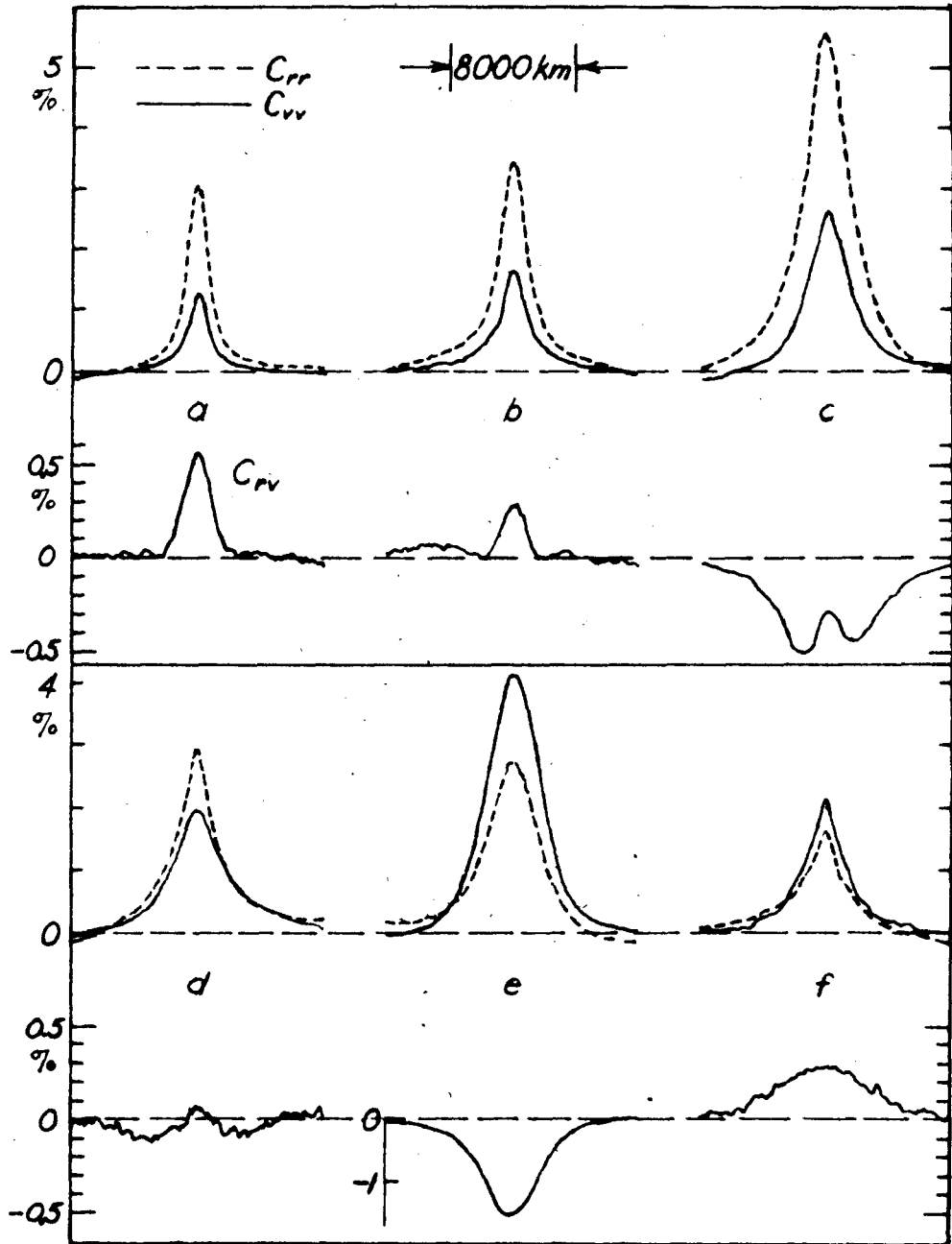


Figure 3-14. A-C curves of original plates exposed on the violet (—) and red (----) sides of various spectral lines. Also shown (bottom curve of each group) is the C-C curve between the images on the two wings of each line.

We may use the measured heights of the A-C and C-C functions illustrated in Figure 3-14 to achieve an analytic separation of the mean square brightness fluctuation from the mean square velocity fluctuation, and to investigate their correlation. Recalling equation 2.21 (p. 29),

$$\begin{aligned}
 \text{a) } \quad \langle v^2 \rangle &= \frac{c^2}{4\lambda^2} \left[ \frac{1}{d \ln T / d\lambda} \right]^2 (H_{rr} + H_{vv} - 2H_{rv}) \\
 \text{b) } \quad \langle \beta^2 \rangle &= \frac{1}{4\Gamma^2} (H_{rr} + H_{vv} + 2H_{rv}) \\
 \text{c) } \quad \langle \beta v \rangle &= \frac{c}{4\Gamma\lambda} \frac{1}{d \ln T / d\lambda} (H_{rr} - H_{vv}),
 \end{aligned} \tag{2.21}$$

we obtain for these quantities the values listed in Table V. Further, we may define a correlation coefficient  $C$  between the brightness and velocity to be

$$C = \frac{\langle \beta v \rangle}{\langle \beta^2 \rangle^{1/2} \langle v^2 \rangle^{1/2}} = \frac{H_{rr} - H_{vv}}{[(H_{rr} + H_{vv})^2 - H_{rv}^2]^{1/2}}. \tag{3.12}$$

The values of  $C$  calculated in this manner are listed in the sixth column of Table V.

As we have pointed out in Part II, some internal inconsistency appears when one compares  $\langle v^2 \rangle$  as calculated by equation 2.21 above with the same quantity as calculated from singly cancelled Doppler plates in the normal fashion (eq. 2.16, p. 27). The source of the inconsistency is quite possibly the C-C curves, the heights of which appear in general to be too low. This question is discussed in more detail in Appendix III. Here we simply wish to estimate to what extent such errors would affect the values of the correlation coefficient just obtained.

Table V\*

Line	Offset (Å)	$\langle v^2 \rangle^{\frac{1}{2}}$ (km s <sup>-1</sup> )	$\langle \frac{\Delta I}{I} \rangle^{\frac{1}{2}}$ = $\langle \beta^2 \rangle^{\frac{1}{2}}$	$\langle v \frac{\Delta I}{I} \rangle$ = $\langle v \beta \rangle$ (km s <sup>-1</sup> )	C (using (3.12))	C (using (3.15))
Fe 6102	.10	.39	.039	.0057	.38	.34
Ca 6103	.10	.43	.048	.0103	.50	.38
Ba <sup>†</sup> 4554	.07	.61	.068	.0166	.38	.42
Na 5896	.17	.35	.053	.0022	.12	.12
Na 5896	.11	.50	.045	-.0051	-.23	-.37
Ca <sup>†</sup> 8542	.23	1.20	.048	-.0070	-.12	---
		(+30%)	(+30%)	(+30%)	(+20%)	(+20%)

\* Data for each spectral line were obtained from measurements of plates taken during a single set of observations. Such sets of measurements are usually self-consistent to within 10%. However, systematic and random errors which vary from day to day arise from numerous sources; these errors may be correlated or uncorrelated in the various columns of the table. The uncertainties indicated at the foot of each column represent our best provisional estimates, based upon our experience with many plates reduced under similar conditions, but are not to be considered as independent statistical errors in the usual sense.

From Appendix III we find that the four quantities  $H_{rr}$ ,  $H_{vv}$ ,  $H_{rv}$ , and  $H_{cc}$  (where  $r$ ,  $v$ , and  $c$  refer to the images on the red and violet sides of the spectral line and to the cancelled image) contain redundant information about the three quantities  $\langle \beta^2 \rangle$ ,  $\langle v^2 \rangle$ , and  $\langle \beta v \rangle$ . We may thus determine the correlation coefficient  $C$  using only the three A-C curve heights  $H_{rr}$ ,  $H_{vv}$ , and  $H_{cc}$ :

$$C = \frac{H_{rr} - H_{vv}}{[2(H_{rr} + H_{vv}) - H_{cc}]^{\frac{1}{2}} H_{cc}^{\frac{1}{2}}} \quad (3.13)$$

In this equation we have eliminated the C-C curve height  $H_{rv}$ , which, as we have said, may be somewhat too low. If we calculate  $C$  by equation 3.13 rather than equation 3.12, we get the values listed in the last column of Table V. Comparison of the last two columns gives an indication of the self-consistency of the technique. We see that although there is some uncertainty in the individual values, the general trend from line to line is about the same.

The conclusions we may draw from Table V are:

- 1) There is a strong positive correlation between brightness and upward velocity at low elevation, which decreases with altitude through zero and becomes negative for lines in the upper photosphere and chromosphere.
- 2) The amplitude of the intensity fluctuation appears to remain about the same or to increase slightly with altitude.
- 3) The velocity appears to increase with altitude, in the same way as we have already observed from our analysis of single cancelled plates.

In Figure 3-15(a-c) we have plotted the values of  $(v^2)^{\frac{1}{2}}$ ,  $(\beta^2)^{\frac{1}{2}}$ , and C from Table V for the various spectral lines studied. The lines are arranged along the abscissa in order of increasing residual intensity, in the fashion described on page 44.

The fact that in the photosphere the rising material is brighter (i. e., hotter) than average and the falling material is darker (i. e., colder) than average suggests that there is a net flux of energy upward in the photosphere. As we have already mentioned, the statement that intensity fluctuations in spectral lines are proportional to temperature fluctuations in the region of line formation is an extremely crude approximation, especially in the chromosphere. Nevertheless, it is interesting to evaluate the flux observed at various heights in the atmosphere on the basis of this assumption.

The energy transported upward per second per  $\text{cm}^2$  at any point in the solar atmosphere consists of a part due to bodily transport of heat, a part due to work done by pressure, and a part due to bodily transport of kinetic energy:

$$E = \frac{1}{\gamma-1} \rho \frac{RT}{\mu} v + Pv + \frac{1}{2} \rho v^3 = \frac{\gamma}{\gamma-1} Pv + \frac{1}{2} \rho v^3 \quad (3.14)$$

The last term may be written as  $\frac{1}{2} Pv \left( \frac{\rho}{P} v^2 \right) \sim \frac{1}{2} Pv \left( \frac{v}{v_s} \right)^2$ ; since the velocity of sound  $v_s$  in the solar photosphere is about 6 km/sec, while  $v \sim \frac{1}{2}$  km/sec, the last term is negligible compared to the first.

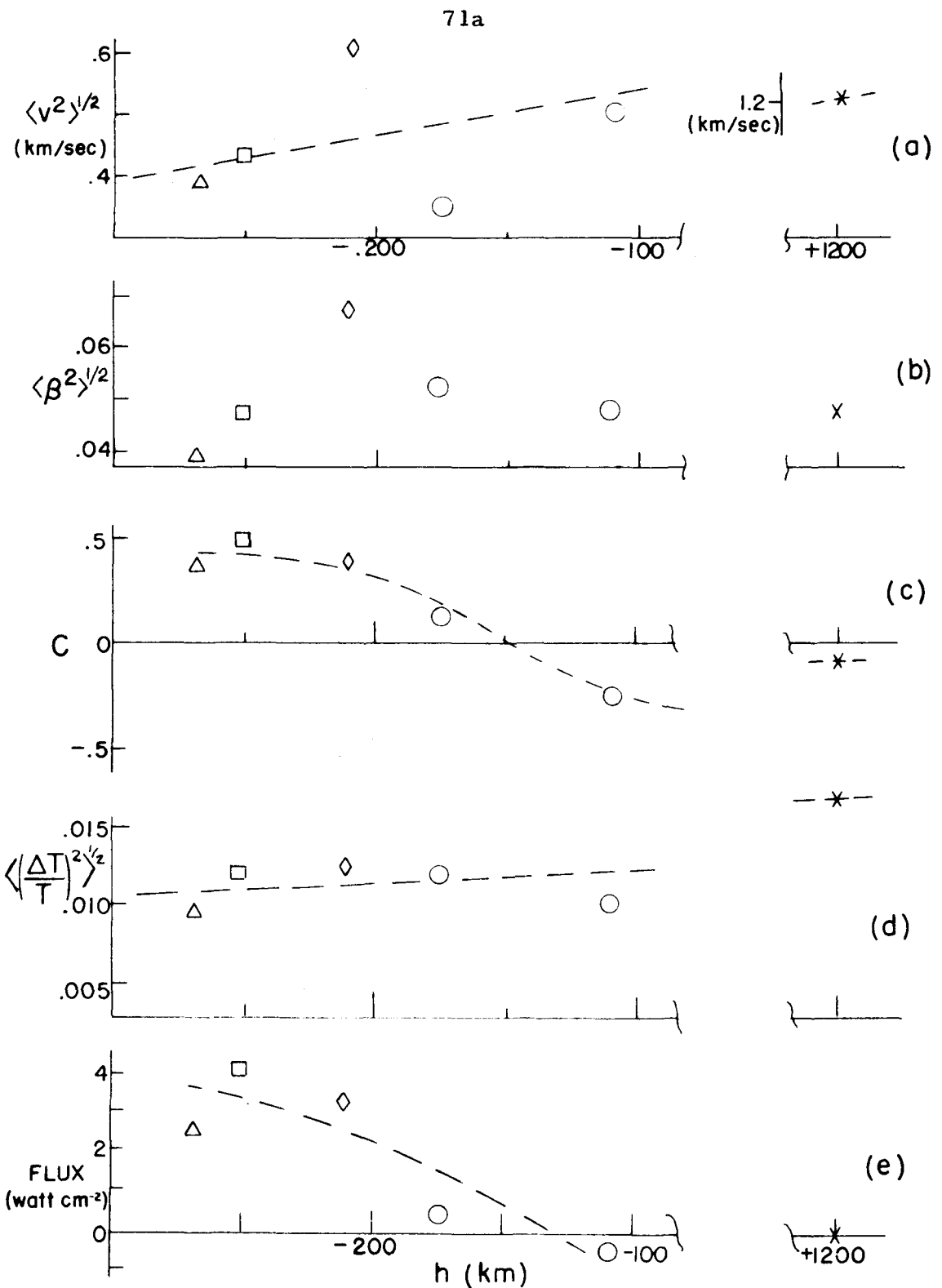


Figure 3-15. Rms velocity, rms intensity fluctuation, brightness-velocity correlation coefficient, rms temperature fluctuation, and upward flux of mechanical energy, as observed at various heights  $h$  in the solar atmosphere.  $\Delta$  = Fe6102;  $\square$  = Ca6103;  $\diamond$  = Ba<sup>+</sup>4554;  $\circ$  = Na5896;  $\times$  = Ca<sup>+</sup>8542.

The spatial average of the energy flux is then

$$\frac{1}{A} \int \mathbf{E}(\mathbf{x}, y) dA = \langle \mathbf{E} \rangle = \frac{\gamma}{\gamma-1} \langle P\mathbf{v} \rangle = \frac{\gamma}{\gamma-1} \frac{R}{\mu} \langle \rho T \mathbf{v} \rangle \quad (3.15)$$

If we write  $T = T_0 + \Delta T$  and note that mass conservation requires  $\langle \rho \mathbf{v} \rangle = 0$ , equation 3.15 becomes

$$\langle \mathbf{E} \rangle = \frac{\gamma}{\gamma-1} \frac{RT_0}{\mu} \left\langle \rho \mathbf{v} \frac{\Delta T}{T_0} \right\rangle \quad (3.16)$$

If we further write  $\rho = \rho_0 + \Delta \rho$  and neglect third degree correlations between the small quantities  $\Delta \rho$ ,  $\Delta T$  and  $\mathbf{v}$ ,

$$\langle \mathbf{E} \rangle = \frac{\gamma}{\gamma-1} \frac{R\rho_0 T_0}{\mu} \left\langle \mathbf{v} \frac{\Delta T}{T_0} \right\rangle = \frac{\gamma}{\gamma-1} P_0 \left\langle \mathbf{v} \frac{\Delta T}{T_0} \right\rangle. \quad (3.17)$$

$$\text{We now set } \frac{\Delta T}{T} \sim a(\lambda) \frac{\Delta I}{I}, \quad (3.18)$$

where  $I$  is the residual intensity of the spectral line,

$$a(\lambda) = \frac{1}{B_\lambda(T)} \frac{\partial}{\partial T} B_\lambda(T), \text{ and} \quad (3.19)$$

$$B_\lambda(T) = f(\lambda) \left( e^{\frac{hc}{\lambda kT}} - 1 \right)^{-1}. \quad (3.20)$$

For  $T = 6000^\circ\text{K}$  and  $4500 \text{ \AA} < \lambda < 8500 \text{ \AA}$ , we find  $5.5 > a(\lambda) > 2.9$ .

In Figure 3-15(d, e) we have plotted  $\frac{\Delta T}{T}$  and the upward flux for the various lines, which we have calculated using equations 3.17-3.20 and the values of  $\frac{\Delta I}{I}$  listed in Table V.

We see that there appears to be an upward flux of  $\sim 3 \text{ watt/cm}^2$  in the solar photosphere, which, however, decreases with increasing altitude, due both to the decreasing brightness-velocity correlation

and the decreasing pressure with altitude. At chromospheric levels the calculated flux is negative. The question arises whether this reversal of flux is an erroneous result of our assumption about the relation between temperature and residual intensity, or whether it is indeed real. If it is real, some sort of dumping of energy into the atmosphere at about the level of the NaD line is suggested. We shall discuss this question further in Part IV.

We shall now return briefly to the cross-correlation curves shown in Figure 3-14 in order to make two additional remarks:

a) With the exception of  $\text{Ca}^+ 8542$ , the height  $H_{rv}$  of the central peak is positive for low-lying lines and negative for high-lying lines. Since  $H_{rv} \propto \beta^2 - \delta^2$ , we conclude that on plates exposed in low-lying lines, the intensity-induced fluctuations are greater than the velocity-induced fluctuations; whereas the situation is reversed for higher lines. In the chromospheric  $\text{Ca}^+ 8542$  line, however, the intensity fluctuations again predominate, presumably due to a decrease of velocity sensitivity in this line along with the appearance of the large-scale chromospheric emission pattern.

b) The C-C curves  $C_{rv}(\xi)$  for Ba 4554 ( $\Delta\lambda = 0.01 \text{ \AA}$ ), and Na 5896 ( $\Delta\lambda = 0.17 \text{ \AA}$ ) have a pronounced  $\nabla$  shape. This implies that there is positive correlation at small displacements  $\xi$  (about 2000 km on the sun) but negative correlation at larger displacements (about 8000 km). Since

$$C_{rv}(s) = \langle [1 + \beta(x,y) + \delta(x,y)]^\Gamma [1 + \beta(x+s,y) - \delta(x+s,y)]^\Gamma \rangle$$

$$= 1 + \Gamma \langle \beta(x,y) \beta(x+s,y) \rangle - \Gamma \langle \delta(x,y) \delta(x+s,y) \rangle, \quad (3.21)$$

this behavior suggests that the size of the elements of the velocity field is greater than that of the elements of the intensity field.

### I. Oscillations in the Chromospheric Brightness Field

As we have just discussed, the presence of a brightness-velocity correlation which is positive in the lower solar atmosphere and reverses sign at higher elevation has led us to suspect an upward flux of mechanical energy in the lower regions, which dissipates itself at higher levels. Inasmuch as the flux is closely associated with the oscillatory motions, it seems reasonable to expect a periodic heating of the chromosphere. Therefore, oscillations in the intensity of the small-scale chromospheric structures were sought in plates taken in the cores of the chromospheric lines Na 5896, Mg 5173, Ca<sup>+</sup> 3933, Ca<sup>+</sup> 8542, and H $\gamma$ . The plates used were "brightness difference" plates. These plates are sets of normal spectroheliograms (the beam splitter and line shifter are not used) in which an area of the sun is scanned successively in opposite directions. Pairs of consecutive scans are then "subtracted" photographically in the usual way. If the line is well centered on the slit, the intensity should be independent of the velocity field, and should vary only with the residual intensity of the line. For this last statement to be explicitly true,

we require that the width of the line core over which the profile remains at its minimum be larger than the spectroheliograph slit. While this is true for most of the lines listed, there might be some question about the relatively sharp Na 5896 line. However, examination of the profile of Na 5896 recorded with the same slit width used for brightness difference plates shows that a velocity of  $\frac{1}{2}$  km/sec will change the transmission of the plate at that point by less than one percent. (If the slit were accidentally offset by  $\Delta\lambda = 0.01 \text{ \AA}$ , about the maximum tolerated error, the change in transmission due to a  $\frac{1}{2}$  km/sec velocity would be about 3 percent. These numbers should be compared with the 15 percent change in intensity observed due to a  $\frac{1}{2}$  km/sec velocity when the slit is offset to the steep part of the line profile for Doppler measurements. We see that the size of the transmission fluctuations contributed to a "brightness" plate in Na 5896 by velocity field is a factor of at least five smaller than that contributed to each image of a Doppler plate, and at least ten times smaller than that contributed to a cancelled Doppler plate. (The factor of 2 is included because of the doubling of the velocity-induced fluctuation in a Doppler cancellation.) For the other lines studied, the velocity-induced fluctuations are even less.

In spite of this loss of velocity sensitivity, however, a relatively strong secondary minimum of contrast is observed in the brightness difference plates. This is observed not only in plates

exposed in the Na 5896 line, but also on those exposed in Mg 5173, Ca<sup>+</sup> 3933, and Ca<sup>+</sup> 8542. The Ca<sup>+</sup> 3933 plates have been taken in the core and also at various positions on the line wing. The slope of the line wing for Ca<sup>+</sup> 3933, however, is so small that there is negligible Doppler sensitivity. In several cases, for Na 5896, Mg 5173, and the Ca<sup>+</sup> 3933 wing, the minimum of contrast after one period is nearly as pronounced as that for a normal Doppler difference plate. Therefore, due to the relatively good cancellation even when the Doppler sensitivity is very low (indeed essentially zero for Ca<sup>+</sup> 3933), we feel confident that the brightness oscillation observed is truly due to variations in residual intensity rather than to a pure Doppler shift of the line profile.

Table VI lists the values for the period derived from visual observations of these lines. The method of analysis of the visual estimates is the same as that for the oscillation period estimates. It is seen that the period is considerably shorter for the chromospheric brightness oscillation than for the velocity oscillations at somewhat lower levels. In Figure 3-16 we have plotted the determination of average period versus the mean height of emission (the height where the optical depth in the line is unity) of these various chromospheric lines as given by De Jager (10). Also in the figure we have included our earlier measurements of average velocity period.

TABLE VI

Estimate of Average Intensity Period for Various Spectral Lines

Time Interval	Line	No. of Plates	No. of Estimates	EW	Average Time (sec)	$\sigma$ (sec)
T/2	Na5896	7	17	53	130.5	1.6
	Mg5173	3	6	20	142	5
	Ca <sup>+</sup> 8542	3	7	13	103	4
	Ca <sup>+</sup> 3933					
	$\Delta\lambda = .83$ A	1	2	4	124	4
	.58 A	1	2	4	115	4
	.50 A	1	2	4	120	10
	.35 A	1	2	5	130	3
	.10 A	1	1	1	95	-
T	Na5896	7	15	44	257.5	4.2
	Mg5173	3	6	20	281	5
	Ca <sup>+</sup> 8542	3	6	8	200	15
	Ca <sup>+</sup> 3933					
	$\Delta\lambda = .83$ A	1	2	7	262	10
	.58 A	1	2	7	265	20
	.50 A	1	3	5	238	20
	.35 A	1	2	6	262	10
	.10 A	1	2	3	174	10

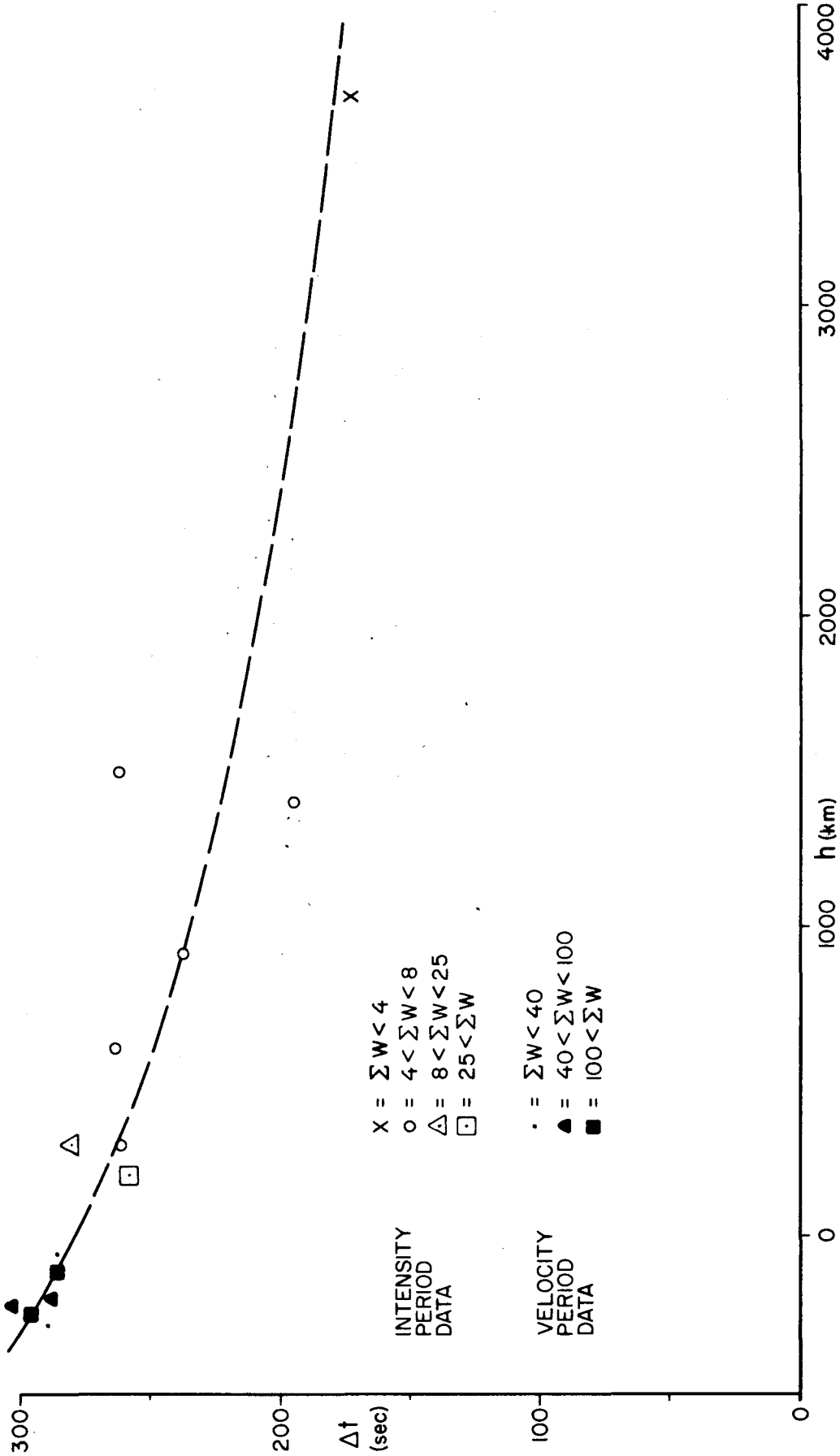


Figure 3-16. Estimates of average period of intensity oscillation in chromospheric lines, from Table VI. Also shown are estimates of velocity period for upper photospheric lines (Cf. Fig. 3-10). The reliability of the measurements is greater for those points with the greatest total weight ( $\Sigma W$ ).

As can be seen from the fourth and fifth columns of Table VI, the reliability of the brightness period determinations is (except for the case of Na) vastly inferior to the velocity period determinations. This is due both to the paucity of observations and to their inaccuracy, i. e., to their large standard deviation. Nevertheless, it appears that we may draw two conclusions: (1) the period of the brightness oscillation is somewhat shorter than that of the velocity oscillation, even when the observations are made at approximately the same level, and (2) there is a tendency for the brightness oscillation period to decrease with altitude, in the same way as the velocity oscillation period. The second conclusion must be regarded as tentative only, in view of present observational uncertainties.

A third conclusion may be drawn from the visibility of the minimum contrast on brightness difference plates. The minimum of contrast is much easier to see and identify on brightness difference plates exposed in the core of Na 5896, the core of Mg 5173, and the wing of CaK (for offsets from the core  $\Delta\lambda > 0.2 \text{ \AA}$ ) than on similar plates exposed in the core of CaK or Ca<sup>+</sup> 8542. Careful search of brightness difference plates in H $\alpha$  reveals no sign of a periodicity. This suggests that the brightness period is more predominant in the chromosphere below 3000 km than above that level, and that by the time the altitude of H $\alpha$  (5000 km) is reached, the brightness oscillation has entirely disappeared.

Finally, we shall report on preliminary attempts to detect the brightness oscillation at levels lower than that of the Na 5896 core. The best way to accomplish this would be to take brightness-difference plates in the cores of photospheric lines. Lacking such plates, the following method was used: Doppler difference plates exposed in the photospheric lines Fe 6102, Ca 6103, and Na 5896 were recancelled in order to bring out the brightness field rather than the velocity field. As is seen from equation 2.13, this is accomplished by adding, rather than subtracting, the density on the two members of an image pair. When such a photographic addition was performed to obtain the brightness field and the brightness difference between two successive plates obtained, only a very weak, although definite, cancellation was observed in the Na 5896 line ( $\Delta\lambda = 0.16 \text{ \AA}$ ), and no sign of a brightness oscillation was observed in the Fe 6102 or Ca 6103 lines. Instead, for the latter lines a uniform decay of the time correlation was observed, with a time constant of a few minutes.

The above should not be accepted as conclusive evidence that the brightness oscillation disappears in the photosphere, in view of the fact that only three plates were analyzed (the photographic reduction process involved in preparing a photographic addition rather than a subtraction is very tedious). Nevertheless, there is some encouragement in the agreement with direct observations of the granulation

immediately below, which reveal no sign of a periodicity in brightness (11). A search for brightness oscillations in the cores of upper photospheric lines, as well as H $\beta$ , H $\gamma$ , and H $\delta$ , is presently under way.

#### J. Observations of the Phase Relation between the Velocity and Brightness Oscillations

On one occasion (August 1, 1961) a normal Doppler scan of the sun was made in the Na 5896 line, with slits offset 0.16 Å from the line core, immediately followed by a return scan in the core. Also, a scan in the core at a later time was immediately followed by a normal Doppler scan with slits offset 0.08 Å from the core. This offered two opportunities for observing the time correlation between the brightness and velocity field by searching for a minimum in contrast in the difference between the consecutive Doppler and core brightness plates. Such a minimum was sought and actually found; the cancellation was rather weak, but definite. The time delay and the Doppler polarity were such that the cancellation implied a negative correlation between the two fields; areas with increased intensity were associated with velocities of recession about 270 sec later, and velocities of recession were followed by increased intensity about 295 sec later. This implies that the brightness oscillation leads the velocity oscillation by about 163°. The result that the two oscillations

are anticorrelated is in good agreement with the negative brightness-velocity correlation already found at the elevation of the NaD line core and inner wing.

We must qualify the result above by noting that uncertainties in identifying the minimum of contrast might allow the phase by which the intensity leads the velocity to be anywhere between about  $150^\circ$  and  $175^\circ$ . Also, it should be mentioned that the plates taken in the core and in the line wing refer to somewhat different elevations; the core is formed at a rather higher altitude. The exact difference is of course exceedingly uncertain, but if as a first approximation we assign a height of formation to the core based on the measured residual intensity, as described on page 44, we find the difference of height between the core and the average offset ( $\Delta\lambda = .12 \text{ \AA}$ ) for these measurements to be  $\Delta h \sim 100 \text{ km}$ . If we assume that we are observing an acoustic wave propagating upward at the sound speed  $V_s \sim 5 \frac{\text{km}}{\text{sec}}$ , then disturbances at the altitude of the core should lag disturbances at  $\Delta\lambda = .12 \text{ \AA}$  by  $\sim 20 \text{ sec}$ . Therefore, we conclude that at the latter elevation the intensity should lead the velocity by about  $163^\circ + \frac{20}{300} 360^\circ \sim 187^\circ$ , or, equivalently, it lags the velocity by  $173^\circ$ .

The rather large uncertainty in this measurement should not be underrated. We have roughly calculated the phase lag in the face of such uncertainties only because the phase relations between temperature and velocity have a great significance in any theoretical interpretation of the observations. In the discussion, to which we shall now turn, we shall come back to this point and consider it further.

## PART IV. DISCUSSION

### A. Introduction

The possibility that oscillatory motions might be present in the solar photosphere and above has been recognized at least since the mid 1940's. About that time it became apparent that in the low chromosphere there is a reversal of the temperature gradient, and that above that point the temperature climbs steeply to attain a value of  $1-2 \times 10^6$ °K in the corona. The flux of non-radiative energy required to maintain such an extreme temperature inversion has been estimated (12, 13) to be from one to several watts per square centimeter. Biermann (14) in 1946 and Schwarzschild (15) in 1948 independently suggested that the required non-thermal energy flux might be supplied by acoustic waves generated by turbulent motion in the granulation at the top of the convection zone, propagated through the convectively stable upper photosphere, and finally dissipated as heat in the chromosphere and corona. As the acoustic wave travels upward through regions of decreasing density, its amplitude should increase, and if at higher altitudes the material velocity becomes comparable to the sound velocity, the acoustic waves will be transformed into shock waves with accompanying dissipation.

The theoretical problem of an acoustic wave propagating in a

gravitating atmosphere was attacked as early as 1845 by Laplace (16), followed in 1890 by Rayleigh (17) and in 1908 by Lamb (18). These studies have been extended and applied to low frequency acoustic waves generated in the earth's atmosphere by meteor impacts (19) and atomic explosions (20). Since the already mentioned work of Biermann and Schwarzschild, a number of authors have analysed the propagation of acoustic waves in the solar atmosphere (21, 22, 23, 12).

The present observations have provided the first direct evidence of the actual presence of such an acoustic wave in the solar atmosphere. In the short time since the first announcement of the observations, corroborating evidence has appeared from several other observers. Evans and Michard (8) at the Sacramento Peak Observatory have obtained time lapse spectrogram sequences at single points on the solar surface, and have found evidence for the oscillation simultaneously in different spectral lines. They also have observed the brightness oscillation in the cores of stronger lines, as well as phase relations between velocity oscillations at different altitudes and between the brightness and velocity oscillations at the same altitude (24). Howard (25) at Mt. Wilson has observed a 300 sec periodicity in the velocity time-correlation function, as well as a 380 sec decay time of the function, by using the Babcock magnetograph set in the Doppler mode. Deubner (26) reports similar results from the Fraunhofer Institute's magnetograph in Anacapri.

In any theoretical analysis of an acoustic wave propagating vertically through an isothermal atmosphere with gravitational acceleration  $g$  and scale height  $H$  (the vertical distance in which the density and pressure drop by a factor  $\frac{1}{e}$ ), a critical frequency  $\omega_c$  appears, which is of the order of  $\sqrt{\frac{g}{H}}$ ; we shall see that if the expansions are isothermal ( $\gamma = 1$ ),  $\omega_c = \frac{1}{2}\sqrt{g/H}$ . For the solar photosphere,  $g = 10^{4.44}$  cm/sec, and at  $\tau = 0.5$ ,  $H \sim 120$  km (7). This yields a critical period  $T_c = \frac{2\pi}{\omega_c} = 262$  sec. The striking agreement with our observed oscillation period strongly suggests that we are actually observing the motion of material in a vertical gravitational-acoustic wave.

While our observations therefore provide gratifying confirmation of long-standing theoretical predictions, they also seem to raise some new questions. Chief among these is the problem of understanding how the particular frequency we observe is singled out, and what its precise value can tell us about the structure of the solar atmosphere. The fact that the period depends on altitude suggests that it is probably not a normal mode of the atmosphere, but is determined by local conditions which vary with height. The presence of an oscillation in the intensity field raises questions about the thermodynamic character of the acoustic wave, which have often been neglected. The variation of amplitude of the oscillation with height should tell us something about the energy dissipation and reflection

of the wave. Finally, the three-dimensional properties of the wave (variation of size of the oscillating elements with height, the relative sizes of the elements of the intensity and velocity fields, and the ratio of horizontal to vertical velocities) need explaining.

It is not within the scope of this thesis to present a full-scale discussion of the above questions. Nevertheless, it is possible to present a rather simplified picture of the mechanism behind the oscillation; such a picture has been found to retain the overall qualitative features of the observations we have just reported, at the sacrifice of more detailed agreement between theory and observations.

We shall now discuss such a simplified mathematical description of the wave and try to use it to see how the atmosphere can single out a predominating frequency. Next we shall consider various mechanisms by which this frequency can change with height. Finally, we shall devote some time to the question of radiative thermal relaxation in the solar atmosphere, in an attempt to understand the observed rms intensity fluctuations, the brightness-velocity correlation, the oscillations of the intensity field, and the phase between the intensity and velocity oscillations.

### B. The Wave Equation

In order to make a quantitative treatment of oscillations in the solar atmosphere at all tractable, certain simplifying approximations must be made. First, we shall restrict ourselves to small

perturbations of the static conditions, i. e., we consider linearized solutions to the hydrodynamic equations. This we realize already removes us somewhat from reality, for the total excursion of a typical element during an oscillation period,  $2 \frac{v_0}{\omega}$  (for  $v = v_0 \cos \omega t$ ) is about 50 km for the observed values of  $\omega$  and  $\langle v^2 \rangle^{\frac{1}{2}}$ . This distance is a large fraction of a scale height, and thus any small element of the gas travels back and forth between regions of rather different pressure and density. In addition, we shall neglect viscosity, heat conduction, magnetohydrodynamic effects, and radiation. (The first two are indeed negligible, and the third is negligible in the photosphere but not in the chromosphere. The last is nowhere negligible. We shall shortly try to consider some of its effects separately.)

With these approximations, we may write down the usual hydrodynamic relations for perturbed quantities in terms of the velocity and the unperturbed quantities:

$$\frac{\partial \rho'}{\partial t} + \nabla \cdot (\rho_0 \underline{v}) = 0 \quad (\text{continuity}) \quad (4.1)$$

$$\frac{\partial}{\partial t} (\rho_0 \underline{v}) = \rho' \underline{g} - \nabla P' \quad (\text{momentum conservation}) \quad (4.2)$$

$$\rho_0 \frac{\partial E'}{\partial t} + \rho_0 \underline{v} \cdot \nabla E_0 = - \nabla \cdot P_0 \underline{v} + \underline{g} \cdot (\rho_0 \underline{v}) \quad (\text{energy conservation}) \quad (4.3)$$

$$P' = \rho_0 \frac{R}{\mu} T' + \frac{R}{\mu} T_0 \rho' \quad (\text{equation of state}) \quad (4.4)$$

$$E = \frac{1}{\gamma-1} \frac{P}{\rho} \quad (4.5)$$

where  $P = P_0 + P'$ , etc., and  $P_0$  is the equilibrium pressure, etc. For a layered atmosphere, where  $\underline{g} = -g \underline{e}_z$ , and  $P_0 = P_0(z)$ ,  $\rho = \rho_0(z)$ , these equations may be combined to give a general equation for the perturbation velocity  $\underline{u} = \underline{v}/c$ , where  $c^2(z) = \frac{\gamma P_0(z)}{\rho_0(z)}$  :

$$\begin{aligned} \frac{\partial^2 \underline{u}}{\partial t^2} - c^2 \nabla (\nabla \cdot \underline{u}) + \left[ \gamma - 1 - \frac{\gamma}{2} \frac{dH}{dz} \right] g \underline{e}_z \nabla \cdot \underline{u} + \left( 1 - \frac{\gamma}{2} \frac{dH}{dz} \right) g \nabla \underline{u}_z \\ + \left[ \frac{\gamma}{2H} \frac{dH}{dz} + \frac{1}{4} \frac{\gamma}{H} \left( \frac{dH}{dz} \right)^2 - \frac{\gamma}{2} \frac{d^2 H}{dz^2} \right] g \underline{u}_z \underline{e}_z = 0 \end{aligned} \quad (4.6)$$

In this equation  $H(z)$  is the (variable) scale height  $\frac{P_0(z)}{\rho_0(z)g} = \frac{c^2(z)}{\gamma g}$ .

This general equation is rather complex; it may be reduced somewhat if we further idealize and restrict ourselves to the isothermal case ( $c = \text{constant}$ ,  $H = \text{constant}$ ):

$$\frac{\partial^2 \underline{u}}{\partial t^2} - c^2 \nabla (\nabla \cdot \underline{u}) + (\gamma - 1) g \underline{e}_z \nabla \cdot \underline{u} + g \nabla \underline{u}_z = 0 \quad (4.7)$$

Unfortunately, even this simplified case presents problems, for in general the flow will not be irrotational unless  $\gamma = 1$ . As will shortly be seen, however, in the photosphere radiative leakage is so fast compared to the oscillation period that temperature perturbations are unable to build up, and the expansions and compressions are essentially isothermal. Therefore, in the photosphere the effective value of gamma is in fact nearly unity. If we set  $\gamma = 1$  in equation 4.7, we obtain the irrotational equation

$$\frac{\partial^2 \underline{u}}{\partial t^2} - c^2 \nabla^2 \underline{u} + g \nabla \underline{u}_z = 0. \quad (4.8)$$

Although we can scarcely expect exact agreement with observations from equation 4.8, the solution should have at least qualitative similarity to the actual situation. The complications we are omitting will certainly alter the details, but the basic description of an acoustic wave propagating under the influence of a gravitational field is contained in equation 4.8.

To discuss this equation we first note that since the flow is irrotational  $\underline{u}$  is the gradient of a velocity potential  $\varphi$ . Substituting  $\underline{u} = \nabla \varphi$  into equation 4.8, we see that the three equations contained there reduce to one equation with the same appearance:

$$\frac{\partial^2 \varphi}{\partial t^2} - c^2 \nabla^2 \varphi + g \frac{\partial \varphi}{\partial z} = 0 \quad (4.9)$$

For convenience we write this in dimensionless units, setting  $c = 1$  and  $g = 2$ , hence  $H = \frac{c^2}{g} = \frac{1}{2}$

$$\frac{\partial^2 \varphi}{\partial t^2} - \nabla^2 \varphi + 2 \frac{\partial \varphi}{\partial z} = 0 \quad (4.10)$$

This equation is separable, and the solution is easily found to be

$$\varphi(\underline{r}, t) = e^z \iiint A(\underline{k}) e^{i \underline{k} \cdot \underline{r}} e^{-\omega(\underline{k}) t} d^3 \underline{k} \quad (4.11)$$

where

$$\omega^2(k) = 1 + k^2 \quad (4.12)$$

and  $A(k)$  is determined from the initial or boundary conditions in the usual way. If the boundary condition is, for instance, that there be an oscillating velocity potential on the plane  $z = 0$ , i.e.,

$\varphi(z=0, t) = A_0 \cos \omega_0 t$ , then the response is one dimensional, and

$$\varphi(z, t) = A_0 e^{z i(k(\omega_0)z - \omega_0 t)} \quad (4.13)$$

If  $|\omega_0| > 1$ ,  $k(\omega_0)$  is real, and we have just an upward propagating wave. The group velocity  $\frac{d\omega_0}{dk} = \frac{\sqrt{\omega_0^2 - 1}}{\omega_0}$ , or in real units  $v_g = \frac{\sqrt{\omega_0^2 - c^2}}{\omega_0} c$  where  $\omega_c = \sqrt{\frac{g}{4H}}$  is the critical frequency and  $c$  is the sound velocity  $c = \sqrt{\frac{\gamma P}{\rho}}$ . The amplitude of the oscillation,  $A = A_0 e^{z/2H}$ , increases with altitude as the wave encounters regions of less and less density. This behavior is to be expected since the kinetic energy per unit volume, which is proportional to  $\rho A^2$ , should remain constant as the wave propagates upward. Since  $\rho \sim e^{-z/H}$  we must have  $A \sim e^{+z/2H}$ .

If  $|\omega_0| < 1$ ,  $k(\omega_0)$  is imaginary, and a standing rather than propagating wave is set up:

$$\varphi(z, t) = A_0 e^{z - \kappa z} e^{i\omega_0 t} \quad (4.14)$$

where  $\kappa = \sqrt{1 - \omega_0^2}$ . Now the amplitude does not increase fast enough to conserve energy density with altitude, because the wave attenuates rather than propagates. In the limit of zero frequency,

$n = 1$ , and the amplitude remains constant, i. e., the atmosphere is simply bodily translated upward.

If we assume cylindrical symmetry and separate the differential equation in cylindrical coordinates, we have in place of equation 4.11

$$\varphi(\rho, z, t) = e^{-z} \iint A(k, l) e^{ikz} J_0(l\rho) e^{i\sqrt{1+k^2+l^2}t} dk dl \quad (4.15)$$

The integral in equation 4.15 may be carried out in closed form only for certain forms of the function  $A(k, l)$ . Typical three-dimensional solutions corresponding to localized, rather than plane, sources at  $t = 0$  are given below:

$$\varphi(\rho, z, t) = \begin{cases} 0, & \tau^2 < 0 \\ z J_1(\tau) & \\ e \frac{1}{\tau}, & \tau^2 > 0 \end{cases}, \quad \tau^2 = t^2 - r^2 \quad (4.16)$$

$$\varphi(\rho, z, t) = \begin{cases} 0, & \tau^2 < 0 \\ z J_0(\tau) & \\ e \frac{1}{\tau}, & \tau^2 > 0 \end{cases} \quad (4.17)$$

$$\varphi(\rho, z, t) = \begin{cases} 0, & t < z \\ z J_0(\sqrt{1-a^2} \sqrt{t-z^2}) K_0(a\rho), & t > z \end{cases} \quad (4.18)$$

From the above examples, it is seen that in general the response to a localized impulse at  $t = 0$  is zero until a time  $R/c_s$  has elapsed, where  $R$  is the distance from the nearest part of the source to the response point and  $c_s$  is the sound velocity. Thereafter a Bessel

function "oscillation"  $J_n(\sqrt{t^2 - r^2})$  sets in with decaying amplitude. The Bessel function has a period which for large times becomes the critical period  $2\pi$ , or in physical units  $\frac{4\pi H}{c}$ . The amplitude again varies with  $z$  as  $e^z$ , or in physical units  $e^{z/2H}$ .

We shall now further restrict ourselves to motion in the vertical, or  $z$ -direction, only, and attempt a somewhat more detailed treatment. The restriction to one dimension is not alarming, in view of the observational evidence that, at least at the level of the Na5896 line, velocities are primarily vertical.

It is well at this point to list again the basic assumptions which underlie the following treatment. These are:

- 1) Small amplitudes (linear behavior)
- 2) No losses due to heat conduction, viscosity, radiation, or magnetic fields
- 3) Isothermal atmosphere
- 4) Isothermal expansions ( $\gamma = 1$ )
- 5) One-dimensional motion

In view of the crudity of each of these assumptions, we shall be content to seek in the equations only a rather qualitative understanding of the wave propagation mechanism.

Since we are dealing with one-dimensional motion, it is as easy to derive the velocity field  $u_z(x, t) = u(x, t)$  as the potential  $\varphi(x, t)$ , and since our observations are of velocity fields themselves, we use the one-dimensional form of equation 4.8 (setting  $c = 1$ ,  $g = 2$ ):

$$\frac{\partial^2 u}{\partial t^2} - \frac{\partial^2 u}{\partial z^2} + 2 \frac{\partial u}{\partial z} = 0. \quad (4.8a)$$

This has the general solution

$$u = e^{-z} \int A(k) e^{ikz - i\omega(k)t} dk \quad (4.11a)$$

where

$$\omega^2 = k^2 + 1 \quad (4.12)$$

We shall now let the initial condition be that there is a localized region of upward-moving material at  $z = 0$  (this is the same problem treated by Lamb (18)\*):

$$u(z, 0) = u_0 \delta(z) \quad (4.19)$$

(This initial condition might correspond physically to the sudden appearance of a bright granule at the photosphere, which is thought of as "breaking the surface" like a bubble rising to the surface of a liquid, causing the "interface" to move upward like a piston (Fig. 4-1).

Since the scale size of a granule is perhaps

700 to 1000 km, and the lines at which we observe the response of the atmosphere are

located not more than a few hundred km

above the granulation "surface," the

approximation of one-dimensional motion

is not totally inappropriate.)

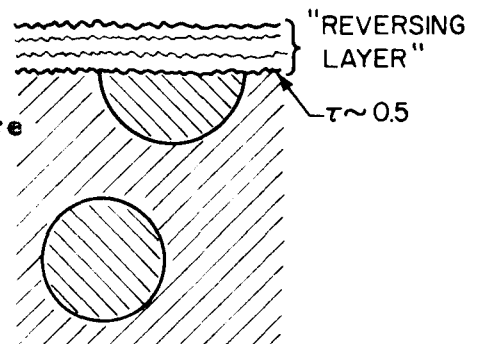


Fig. 4-1

\*I am indebted to Professor R. F. Christy for pointing out this reference.

Our initial condition (eq. 4.19) leads to

$$A(k) = \frac{u_0}{2\pi} \quad (4.20)$$

and

$$u = \operatorname{Re} \frac{u_0}{2\pi} e^{z} \int_{-\infty}^{\infty} e^{ikz} e^{i\sqrt{k^2+1}t} dk = \frac{u_0}{\pi} \int_0^{\infty} \cos kz \cos \sqrt{k^2+1} t dk \quad (4.21)$$

Using the Bateman Tables of Integral Transforms (27),

$$0, t < z$$

$u =$

$$e^{z} \frac{\partial}{\partial t} \frac{u_0}{2} J_0(\sqrt{t^2-z^2}) = -\frac{u_0}{2} e^{z} J_1(\sqrt{t^2-z^2}) \frac{t}{\sqrt{t^2-z^2}}, \quad t > z \quad (4.22)$$

In real units the displacement is  $\xi(z, t) = \frac{u_0}{c} e^{z/2H} J_0\left(\sqrt{\frac{c^2 t^2}{4H^2} - \frac{z^2}{4H^2}}\right)$ .

This is plotted for several values of  $z$  in Figure 4-2. It is seen as expected that the onset of the oscillation occurs only after a time delay  $t_D = \frac{z}{c}$ , and that the amplitude increases as  $e^{z/2H}$ . Although for long times the motion approaches a periodic oscillation with period  $\frac{4\pi H}{c}$ , independent of altitude, the period of the first few oscillations depends on  $z$ , and is shorter for oscillations at higher  $z$ .

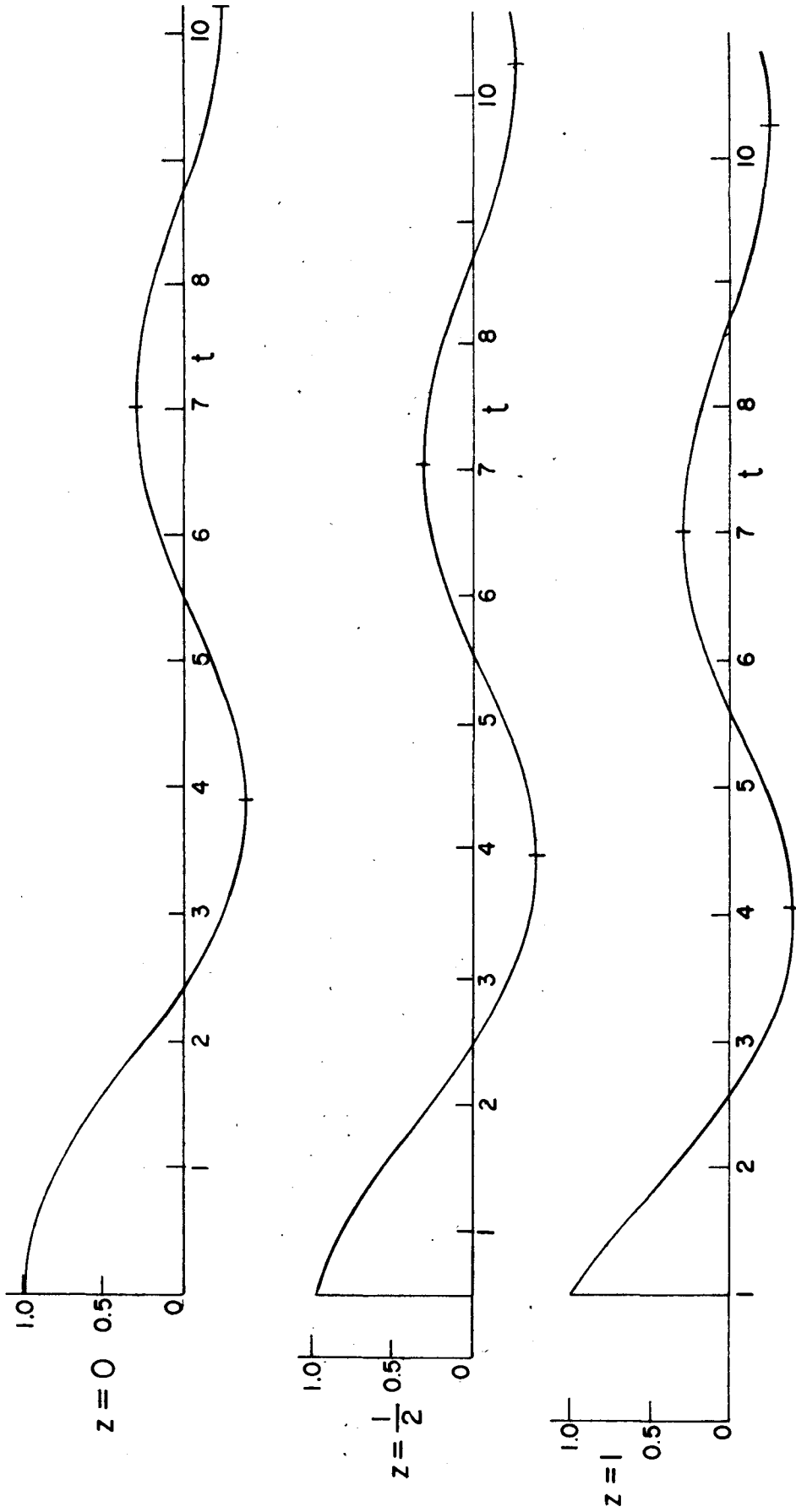


Figure 4-2.  $J_0(\sqrt{t^2 - z^2}) = \frac{2}{u_0} \xi(z, t)$ , plotted versus  $t$  for  $z = 0, \frac{1}{2}$ , and  $1$ . Note the time delay before onset of the oscillation and the shorter period of the first oscillation, for  $z > 0$ .

C. Possible Mechanisms for the Decrease of Average Period of the Velocity Oscillation with Altitude

We shall now turn our attention to the problem of the variation of average period of the oscillation with height in the solar atmosphere. There are several attractive possibilities for explaining the decrease of period with height. Among them are:

1) The intrinsic period is constant with altitude, but the "decay time" of the oscillation, which modifies the observed period, does vary with height.

2) The atmosphere attenuates frequencies below the critical frequency  $\omega_c = \frac{1}{2} \sqrt{\frac{g}{H}}$ . As the wave progresses to higher altitudes there is greater attenuation of low frequencies, causing the average period to decrease. We have just seen (Fig. 4-2) the effect of this attenuation on the response to an impulsive source at the base of the atmosphere.

3) In the solar atmosphere the scale height (which determines the critical period for an isothermal atmosphere to be  $T_c = 4\pi \sqrt{\frac{H}{g}}$ ) is not constant. If the observed period is determined primarily by local conditions at that height, it should vary with height in the same way as  $\sqrt{H}$ .

4) We shall see later that as a wave progresses upward, it passes out of the region where it undergoes isothermal expansions into a more nearly adiabatic region. This causes the speed of sound and the critical frequency to increase.

We shall now discuss these separate possibilities in turn.

1) Change of Decay Time of the Time Correlation Function with Height

We shall assume for simplicity that the time correlation function is of the form

$$C(\Delta) = e^{-\Delta/\tau} \cos(\omega \Delta), \quad (4.23)$$

$\Delta$  being the time lag. Then the maximum time correlation occurs

$$\text{where } \frac{dC}{d\Delta} = 0, \text{ or } \cot \omega \Delta_{\max} = -\omega \tau. \quad (4.24)$$

For a given  $\omega$ , the smaller  $\tau$  is, the smaller will be the period  $\Delta_{\max}$ .

We shall assume  $\omega$  is the same for all lines and find the values of  $\tau$  necessary to yield the observed periods for the various lines. The value of  $\omega$  used was chosen in the following way: The line (Ca6103) with the best determined period,  $T = 296 \pm 2$  sec, was chosen. The observations reported in Part III indicate that the decay time for the oscillation in Ca6103 is about 380 sec. Solving  $\cot[\omega(296 \text{ sec})] = -\omega(380 \text{ sec})$  yields  $\omega = .0208 \text{ sec}^{-1}$ , or  $T = \frac{2\pi}{\omega} = 302$  sec. Using  $\omega = 0.0208 \text{ sec}^{-1}$ , we find the values of  $\tau$  necessary for the various lines listed in the following table:

<u>Line</u>	<u>Observed Average Period (sec)</u>	<u><math>\tau</math> (sec)</u>
Fe6102	289	170
Ca6103	296	380
Mg5528	303	-2310
Ba4554	288	160
Na5846	286	140
Mg5173	285	130
Na5896 core (intensity oscillation)	258	37

However, actual observations of decay of the oscillation in Na5896, which indicated a decay time of 320-440 sec, seem to rule out any decay time as short as 140 sec, and a decay time as short as 40 sec in the intensity oscillation of the Na5896 core would completely suppress the oscillation. Therefore, we conclude that the mechanism for decrease of average period with altitude cannot be simply a decrease of decay time of the oscillation with altitude.

## 2) The Atmosphere as a High Pass Filter; Attenuation of Frequencies

### Less than $\omega$ c

We have already observed that due to the dispersive properties of an isothermal gravitating atmosphere, the response of any point in the atmosphere to a velocity impulse directly below is a quasi-oscillatory motion. Further, we found that the "period" of the first few cycles depends on the separation  $z$  of the source and the response point; namely, the "period" decreases with increasing  $z$  (Fig. 4-2).

This behavior actually can be predicted without solving the problem of an impulse source: we have seen that the dispersion relation for an isothermal one-dimensional atmosphere is  $k^2 = \omega^2 - 1$  in dimensionless units ( $c^2 = \frac{g}{2} = 2H = 1$ ). This means that all frequencies  $|\omega| < 1$  are attenuated rather than propagated (Fig. 4-3).

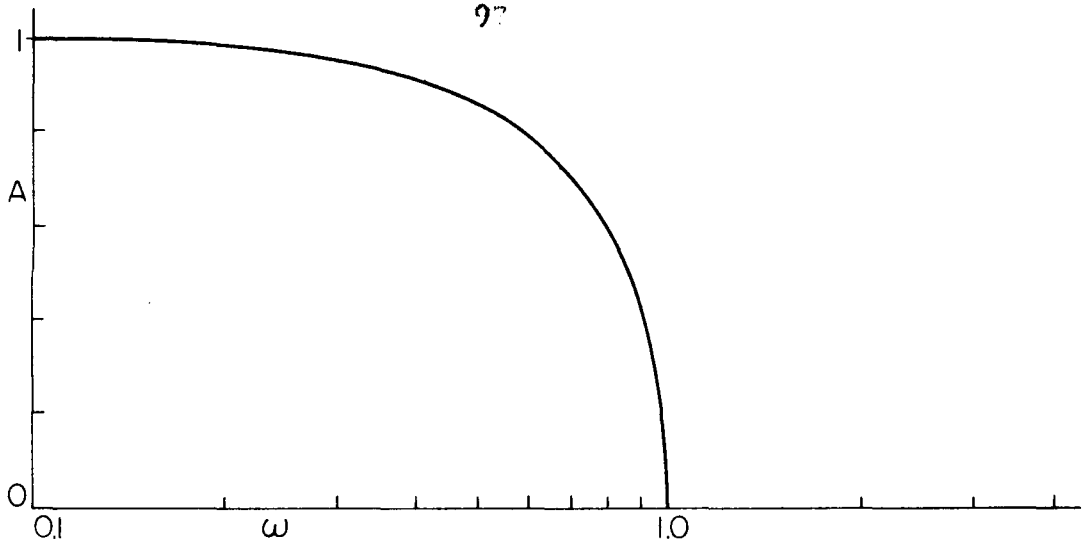


Figure 4-3. Attenuation  $A$  versus  $\omega$  for isothermal oscillations in a gravitating atmosphere.

To the extent that the granulation produces a spectrum which contains significant amplitude in the attenuated frequency range, the response will vary with thickness of the filter traversed by the signal, i. e., the height. Namely, because the lower frequencies are attenuated, the predominant frequency of the transmitted signal will shift to higher frequencies at higher altitudes.

As we see from Figure 4-3, the attenuation for very low frequencies will reduce their amplitude by a factor  $1/e$  in a distance  $\Delta z = 1$ , or in real units,  $\Delta z = 2H$ . The scale height in the region of line formation is 100 to 120 km, which means that the "attenuation length" is 200 to 250 km for very low frequencies. Such a distance is approximately what we estimate to be the distance from the "granulation zone" to level of formation of the upper photospheric and lower chromospheric spectral lines. Thus significant attenuation

is possible in the observed height range.

We should also note that in the photosphere our observed average period of about 300 sec is somewhat longer than the critical period  $\frac{2\pi}{\omega_c} \sim 260$  sec. Thus a considerable fraction of the energy in the frequency spectrum appears to lie in the range  $0 < \omega < \omega_c$ . Therefore, the attenuation of these frequencies should indeed have a large effect on the average frequency.

Finally, we may recall that the chromospheric heating occurs with an average period of 200 to 260 sec, i. e., shorter than the critical period. This implies that the oscillations below the critical frequency must not extend far up into the chromosphere.

### 3) The Variation of Scale Height $H = \frac{RT}{\mu g}$ with Altitude

We have seen (p. 89) that the critical frequency for vertical propagation in an isothermal atmosphere is given by  $\omega_c = \frac{1}{2} \sqrt{\frac{g}{H}}$ . Because of the decrease of the temperature with altitude in the region of observation, the scale height decreases also, and hence the critical frequency increases with altitude. Figure 4-4 is a plot of the scale height  $H = \frac{RT}{\mu g}$  and of the "critical period"  $\frac{2\pi}{\omega_c} = 4\pi \sqrt{\frac{H}{g}}$  versus altitude, using scale heights derived from models by Allen (7) and Kuiper (28). We see that the critical period decreases with altitude in the upper photosphere, by about 15 sec per hundred km.

If the value of the periodicity we observe is determined primarily by the local properties of the atmosphere at the level of

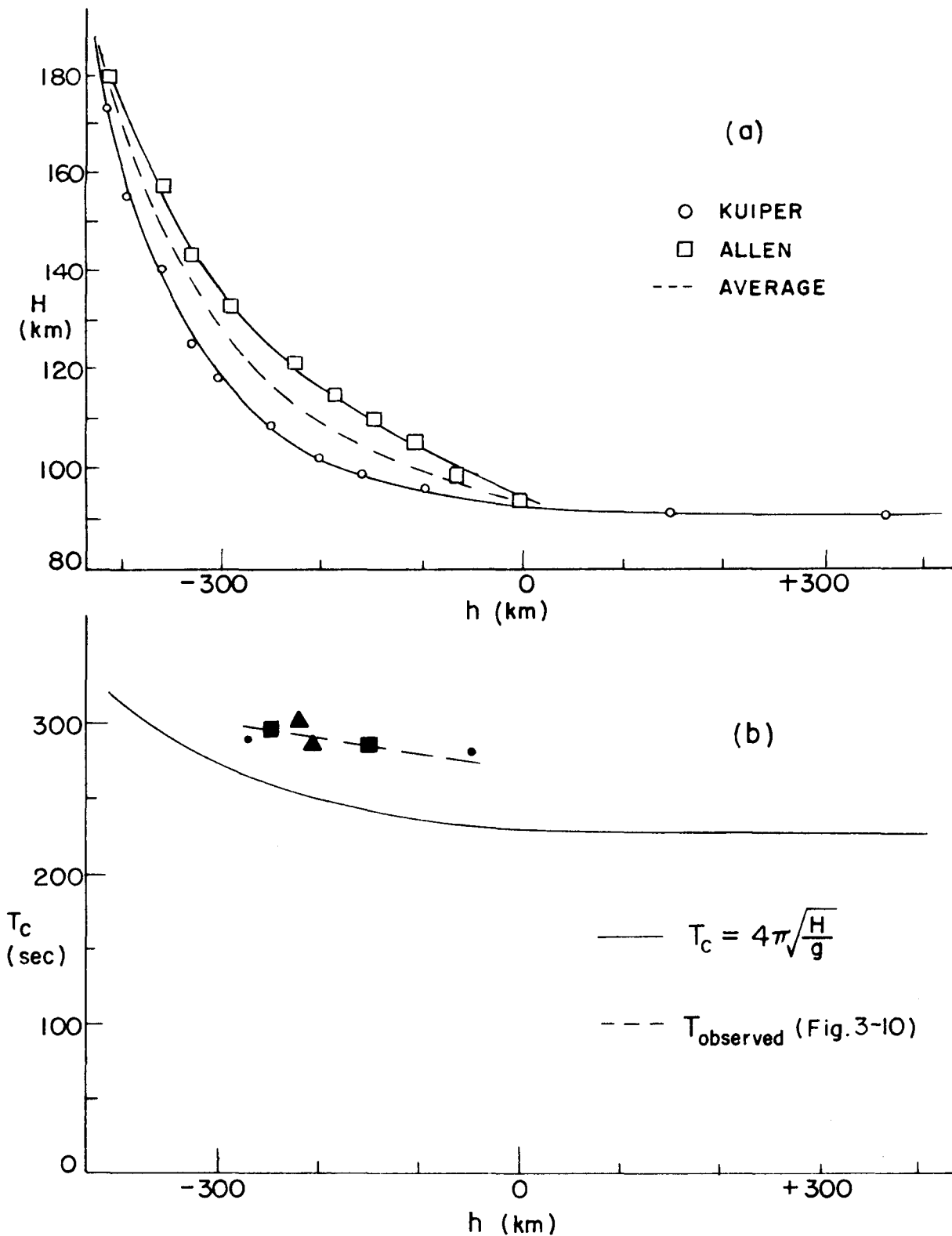


Figure 4-4. (a) Scale height  $H = P/\rho g$ , versus height  $h$  above  $\tau = 0.003$ , using models of Kuiper (28) and Allen (7). (b) Critical period  $T_c = 4\pi\sqrt{H/g}$ , using average scale height from (a). Also shown are observed periods from Figure 3-10.

line formation, then the trend in period will follow the trend of the "local" critical period. It is, however, impossible to predict the exact variation without undertaking to solve directly the complete problem of a pulse propagating vertically through a layered atmosphere.

#### 4) The Effect of Adiabaticity of the Acoustic Wave at Higher Altitudes

We shall see (p. 101) that for an acoustic wave of five-minute period, while the wave expansions are isothermal at low altitudes, they become more nearly adiabatic at higher altitudes. If one considers the case of one-dimensional motion with  $\gamma \neq 1$ , the critical frequency becomes  $\omega_c = \frac{1}{2} \sqrt{\frac{\gamma g}{H}}$ . Thus, if we consider changes of both scale height and "effective  $\gamma$ " with height, the critical period will decrease as  $\sqrt{\frac{H}{\gamma}}$ , i. e., somewhat faster than illustrated in Figure 4-3. As before, in order to get a quantitative estimate of this effect we would have to solve the problem of a layered atmosphere in full.

#### D. The Variation of Opacity with Altitude and Its Possible Effects on the Oscillation

As we have mentioned earlier, in the solar photosphere the lifetime of a temperature perturbation is so short compared to the observed oscillation period that the oscillation may be considered to be isothermal. This may easily be seen by an order of magnitude calculation: Let there be a temperature perturbation  $\Delta T$ , at optical

depth unity. The excess internal energy per unit volume is  $\frac{3}{2} Nk \Delta t$ . The energy absorbed and emitted per unit volume per second is assumed to be  $4\kappa\rho\sigma T^4$  and  $4\kappa\rho\sigma(T + \Delta T)^4$ , respectively, where the absorption coefficient  $\kappa$  is evaluated at optical depth unity. Equating the rate of change of internal energy per unit volume to the excess of absorbed over reradiated energy flux, we have  $\frac{3}{2} Nk \frac{d\Delta T}{dt} = -16\kappa\rho\sigma T^4 \frac{\Delta T}{T}$ . Noting that  $\sigma T_e^4 = \frac{L}{4\pi R_\odot^2}$ ,  $\kappa\rho H = 1$ , where  $H$  is the scale height, and  $NkT = P$ , we see that

$$-\frac{1}{\Delta T} \frac{d\Delta T}{dt} = \beta = \frac{32}{3} \frac{L}{4\pi R_\odot^2} \frac{\kappa\rho}{NkT} \quad (4.25)$$

$$= \frac{8}{3} \frac{L}{\pi R_\odot^2} \frac{1}{NHkT} = \frac{8}{3} \frac{L}{\pi R_\odot^2} \frac{1}{PH}$$

where  $P$  and  $H$  are to be evaluated at  $\tau = 1$ . Using  $\frac{L}{4\pi R_\odot^2} = 6.2 \times 10^{10}$  erg/cm<sup>2</sup> sec,  $P = 10^4$  dyn/cm<sup>2</sup>, and  $H = 100$  km, we find  $\frac{1}{\beta} = 0.15$  sec.

This number is to be compared with  $\frac{1}{\omega} \sim 50$  sec from our observations. The fact that the radiative decay time  $\frac{1}{\beta}$  is so much faster than the "wave compression" time  $\frac{1}{\omega}$  implies that there is no chance for a temperature perturbation to be created by the compression, i. e., the oscillations are isothermal.

Nevertheless, the observations of a brightness oscillation at higher altitude, which is apparently connected with the velocity oscillation, suggest that the behavior is far from isothermal at

these elevations. Accordingly, the radiative relaxation time  $1/\beta$  was calculated for various altitudes, from the photospheric model of Allen (7), using

$$\beta(z) = \frac{16 \kappa(z) \sigma T^3(z)}{\frac{3}{2} k/m_H} \quad (4.26)$$

This relation follows immediately from the relations leading up to equation 4.25, if we use  $\kappa(z)$  and  $T(z)$  directly. It has also been discussed by Spiegel (29) and Krasberg and Whitney (30).

Figure 4-5 presents the results, which show that the radiative decay time  $\frac{1}{\beta}$  increases from  $\sim 1$  sec at  $\tau = 1$  to about 25 sec in the upper photosphere where  $\tau \sim 0.01$ . This latter height is probably about where the Na5896 line wing is formed; the fact that here the decay time  $\frac{1}{\beta}$  is roughly half as large as  $\frac{1}{\omega}$  implies that the oscillation will be non-isothermal at this altitude.

We may investigate acoustic wave propagation vertically in an isothermal gravitating atmosphere with radiative leakage by solving the usual one-dimensional linearized equations for small motions. We shall consider an isothermal atmosphere with temperature  $T_0$  and scale height  $H$ , and use a Lagrangian description of the motion. We let  $z$  be the vertical coordinate and  $\xi(z, t)$  the (small) displacement from equilibrium of a particle whose equilibrium position is  $z$ . Then the position of that particle is  $z + \xi(z, t) = x(z, t)$ . We let  $\rho(z, t)$ ,  $P(z, t)$  and  $T(z, t)$  be the state variables at the position

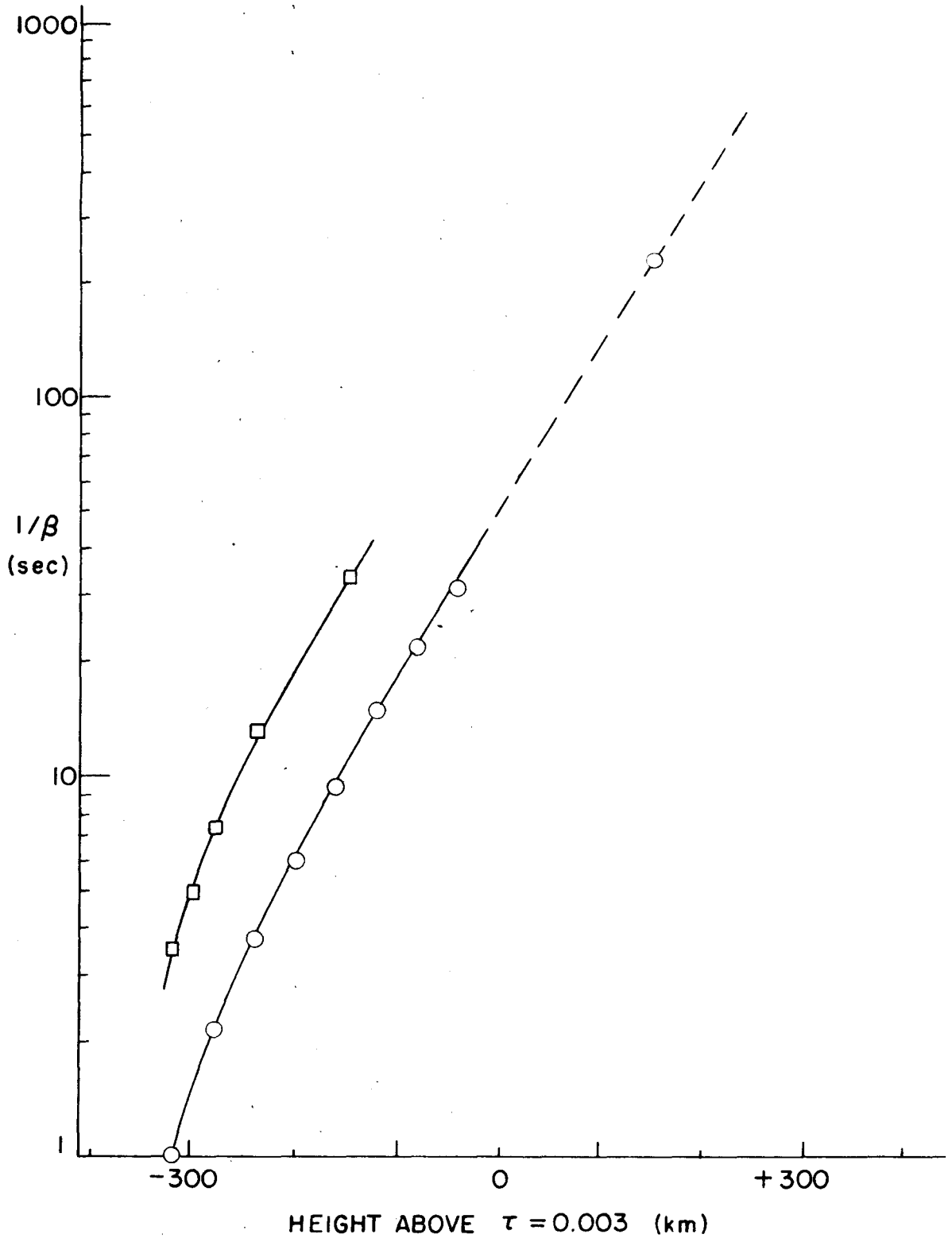


Figure 4-5. Semilog plot of radiative decay time  $\frac{1}{\beta}$  versus height  $z$  above  $\tau = 0.003$ .  $\circ$ : using equation 4.26 and data from Allen (7).  $\square$ : from Krasberg and Whitney (30), Table II.

$x(z, t)$  of the particle. The linearized equations of continuity and of state are then:

$$\rho(z, t) = \rho_0(z) \left(1 + \frac{\Delta \rho}{\rho_0}\right) = \rho_0(z) \left(1 - \frac{\partial \xi(z, t)}{\partial z}\right), \text{ and} \quad (4.27)$$

$$P(z, t) = P_0(z) \left(1 + \frac{\Delta P}{P_0} + \frac{\Delta T}{T_0}\right) = P_0(z) \left(1 - \frac{\partial \xi}{\partial z} + \theta(z, t)\right) \quad (4.28)$$

where

$$\rho_0(z) = \rho_0(0) e^{-z/H} \text{ and } P_0(z) = P_0(0) e^{-z/H} \quad (4.29)$$

are the equilibrium values of density and pressure, and where

$$\theta(z, t) = \frac{\Delta T(z, t)}{T_0} . \quad (4.30)$$

The equation of momentum conservation is

$$\rho_0(z) \frac{\partial^2 \xi(z, t)}{\partial t^2} = - \frac{\partial P(z, t)}{\partial z} - \rho_0(z) g . \quad (4.31)$$

or

$$\rho_0(z) \frac{\partial^2 \xi}{\partial t^2} = - P_0(z) \left[ - \frac{\partial^2 \xi}{\partial z^2} + \frac{\partial \theta}{\partial z} - \frac{1}{H} + \frac{1}{H} \frac{\partial P}{\partial z} - \frac{6}{H} \right] - \rho_0(z) g . \quad (4.32)$$

The zero-order terms  $\frac{P_0(z)}{H}$  and  $-\rho_0(z) g$  on the right hand side cancel, because  $P_0 = \rho_0 g H$  for hydrostatic equilibrium. If we write  $c_0^2 = \frac{P_0}{\rho_0}$ , equation 4.32 reduces to

$$\frac{\partial^2 \xi}{\partial t^2} - c_0^2 \frac{\partial^2 \xi}{\partial z^2} - \frac{c_0^2}{H} \frac{\partial \xi}{\partial z} + c_0^2 \left( \frac{\partial \theta}{\partial z} - \frac{\theta}{H} \right) = 0 . \quad (4.33)$$

We may note that if there is no radiative leakage ( $\frac{\beta}{\omega} \rightarrow 0$ ), the expansions are adiabatic, and we have  $T\rho^{(1-\gamma)} = \text{const.}$ , or

$$\theta = (\gamma - 1) \frac{\Delta\rho}{\rho} = -(\gamma - 1) \frac{\partial \xi}{\partial z} . \quad (4.34)$$

Putting this in equation 4.33 yields

$$\frac{\partial^2 \xi}{\partial t^2} - \gamma c_o^2 \frac{\partial^2 \xi}{\partial z^2} + \gamma \frac{c_o^2}{H} \frac{\partial \xi}{\partial z} = 0 , \quad (4.35)$$

which is the correct adiabatic relation for one dimensional motion (cf. equation 4.7, previous section). On the other hand, if the expansions are isothermal,  $\theta = 0$ , and equation 4.33 reduces to  $\frac{\partial^2 \xi}{\partial t^2} - c_o^2 \frac{\partial^2 \xi}{\partial z^2} + \frac{c_o^2}{H} \frac{\partial \xi}{\partial z} = 0$ , independent of  $\gamma$ . This is the case where radiative leakage is so fast compared to compression times of the wave that temperature perturbations do not have an opportunity to build up, i. e.  $\frac{\beta}{\omega} \rightarrow \infty$ . The mathematical behavior is the same as if there were no source of temperature perturbation; i. e., if  $\gamma$  were equal to 1.

For finite rates of radiative decay,  $0 < \frac{\beta}{\omega} < \infty$ , we expect the temperature to be governed by an equation

$$\frac{\partial \theta}{\partial t} = -\beta \theta - (\gamma - 1) \frac{\partial^2 \xi}{\partial z \partial t} . \quad (4.36)$$

The first term on the right-hand side of equation 4.36 describes the relaxation tendencies of the atmosphere; i. e., a temperature perturbation  $\theta$  decays at a rate proportional to the perturbation. The

second term describes the adiabatic heating due to the rate of compression  $\frac{\partial}{\partial t} \left( -\frac{\partial \xi}{\partial z} \right)$  by the wave. For the equation to be valid we must assume that the atmosphere is optically thin, in order that the second-order radiation effects be negligible, i. e., in order that the perturbed element does not absorb radiation different from the equilibrium value because of the presence of neighboring perturbations.

Now if we assume that

$$\xi = A e^{\frac{+i\omega t}{c_0}} e^{qz} \quad \text{and} \quad \theta = B e^{\frac{+i\omega t}{c_0}} e^{qz} \quad (4.37)$$

we find that, for a solution of equations 4.33 and 4.36 to exist,

$$q = 1 + i \sqrt{\frac{\beta + i\omega}{\beta + i\gamma\omega} \left( \frac{c_0^2}{c^2} - 1 \right)}, \quad (4.38)$$

and

$$B = \mp \frac{(\gamma - 1) i \omega}{\beta + i\gamma\omega} q A. \quad (4.39)$$

Here we have set  $c_0^2 = 2H = \frac{g}{2} = 1$  as before. The first term of equation 4.38 yields the exponential increase of velocity amplitude with height which we have already encountered, and which was necessary to conserve kinetic energy per unit volume for propagation without losses or reflection. We see that if  $\beta = 0$  or  $\infty$  in equation 4.38, that  $\text{Re}(q) = 1$ ; i. e., the amplitude increases with height in the way already discussed. For  $0 < \beta < \infty$ , however, there is a contribution to  $\text{Re}(q)$  from the second term in equation 4.38, causing the

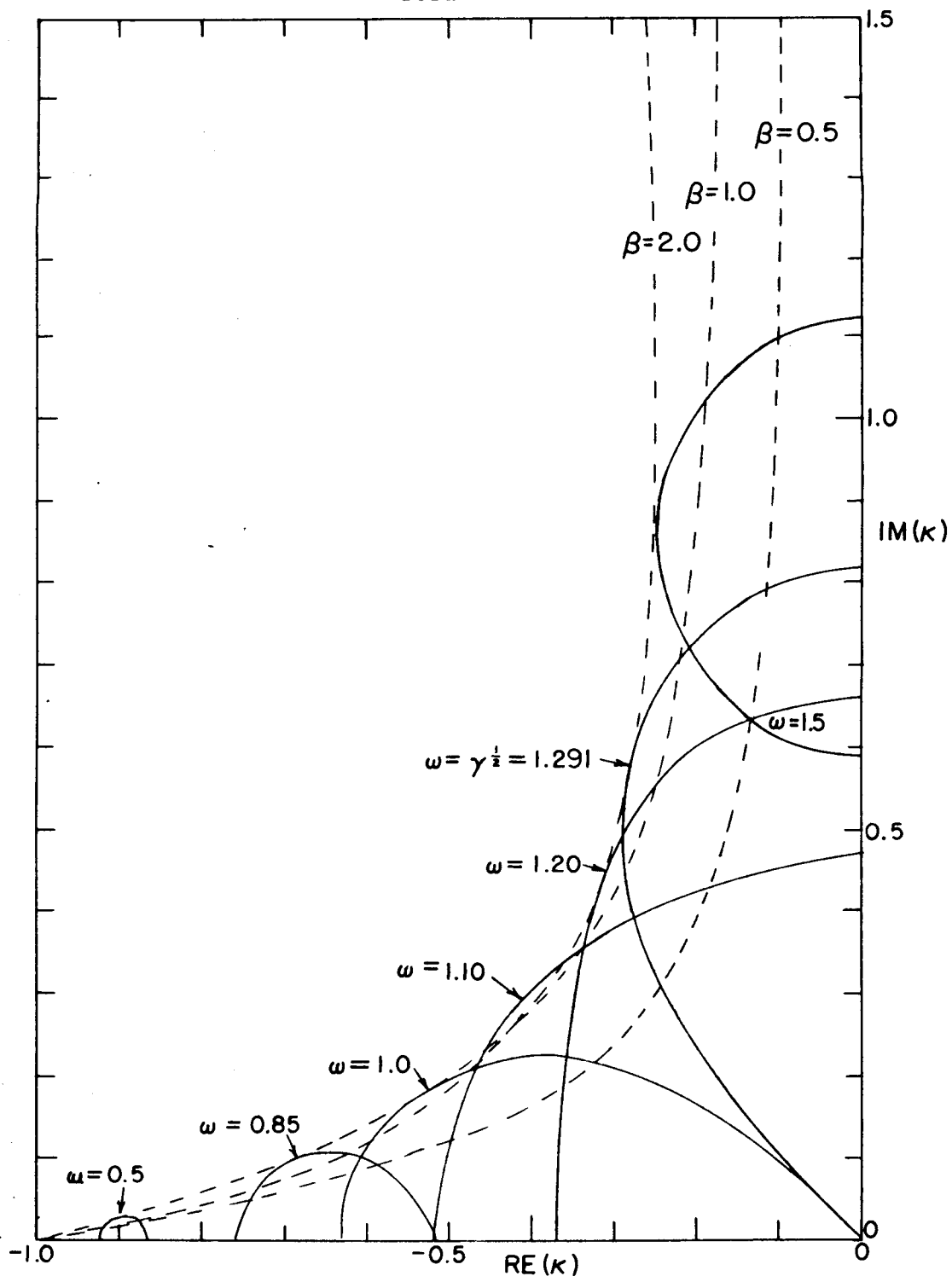


Figure 4-6. The complex wave number  $\kappa(\omega, \beta)$ , plotted for various values of  $\omega$  and  $\beta$ . Solid curves:  $\omega = \text{const}$ .  $\beta$  increases from 0 to  $\infty$  as one progresses clockwise along the curves. Dotted curves:  $\beta = \text{const}$ . The curves  $\beta = \infty$  and  $\beta = 0$  follow the real and imaginary axes, and attain the value  $\kappa = 0$  for  $\omega = 1$  and  $\omega = \gamma^{1/2}$ , respectively.

amplitude to increase with height either faster or slower than in the lossless case. This corresponds to downward or upward propagating waves, respectively. We choose the solution for upward propagating waves:

$$\xi = A e^{-i\omega t} e^{qz}, \quad q = 1 + i \sqrt{\frac{\beta - i\omega}{\beta - i\gamma\omega} \omega^2 - 1} \quad (4.40)$$

$$\theta = B e^{-i\omega t} e^{qz}, \quad B = \frac{(\gamma - 1) i\omega}{\beta - i\omega} qA \quad (4.41)$$

The complex quantity  $q - 1 \equiv \nu(\omega, \beta)$  is plotted in Figure 4-6 for various values of  $\omega$  and  $\beta$ . From Figure 4-6 we see that:

a) If  $\beta = \omega$  (isothermal oscillations) there is a critical frequency below which  $\nu$  is real and negative, i. e., below which there is attenuation but no propagation. Above the critical frequency  $\nu$  is imaginary, and there is propagation but no attenuation. The critical frequency  $\omega_c$  has the value  $\omega_c = 1$ , or in physical units,  $\omega_c = \frac{c}{2H}$ . This is the behavior we have already encountered in our earlier isothermal treatment.

b) If  $\beta = 0$  (adiabatic oscillations) the behavior is the same, except that the critical frequency has shifted to  $\omega_c = \gamma^{\frac{1}{2}}$ .

c) For intermediate values of  $\beta$ , as  $\omega$  increases from zero to infinity,  $\nu(\omega, \beta)$  follows a path in the complex plane from  $-1$  to  $i\omega - \frac{\gamma - 1}{2\gamma} \frac{\omega^2}{\beta}$ . The imaginary part of  $\nu$  is the wave number for

propagation, and the negative real part is the attenuation. This attenuation is due partly to the presence of standing wave components and partly to radiative losses.

Figure 4-7 is a plot of the total attenuation versus  $\omega$  for several values of radiative decay time  $\frac{1}{\beta}$ . The large attenuation for  $\omega$  less than the isothermal critical frequency,  $\omega_c = 1$ , is the same attenuation due to standing wave components which we have encountered in the isothermal case (cf. Fig. 4-3, p. 97). For higher frequencies the attenuation is due to radiative losses.

The fact that for each value of  $\beta$  there is a value of  $\omega$  for which the damping is a minimum might suggest that such differential damping might single out the least damped frequency from a white noise spectrum introduced at  $z = 0$ . The broadness of the minimum in damping as shown in Figure 4-7, however, precludes very sharp filtering in the distance between  $z = 0$  (the top of the convection zone, at  $\tau \sim 0.5$ ) and  $z = 1$  to  $2$  (the line formation region at  $\tau = 0.05$  to  $0.005$ ; in real units  $z = 2H$  to  $4H$ , or  $250$ - $500$  km).

We shall now examine the oscillation of temperature described by equation 4.41 (p. 105). From this equation we see that the amplitude, relative to the velocity amplitude, is

$$\alpha = \left| \frac{B}{-imA} \right| = (\gamma - 1) \left| \frac{-g}{\beta - i\omega} \right| \quad (4.42)$$

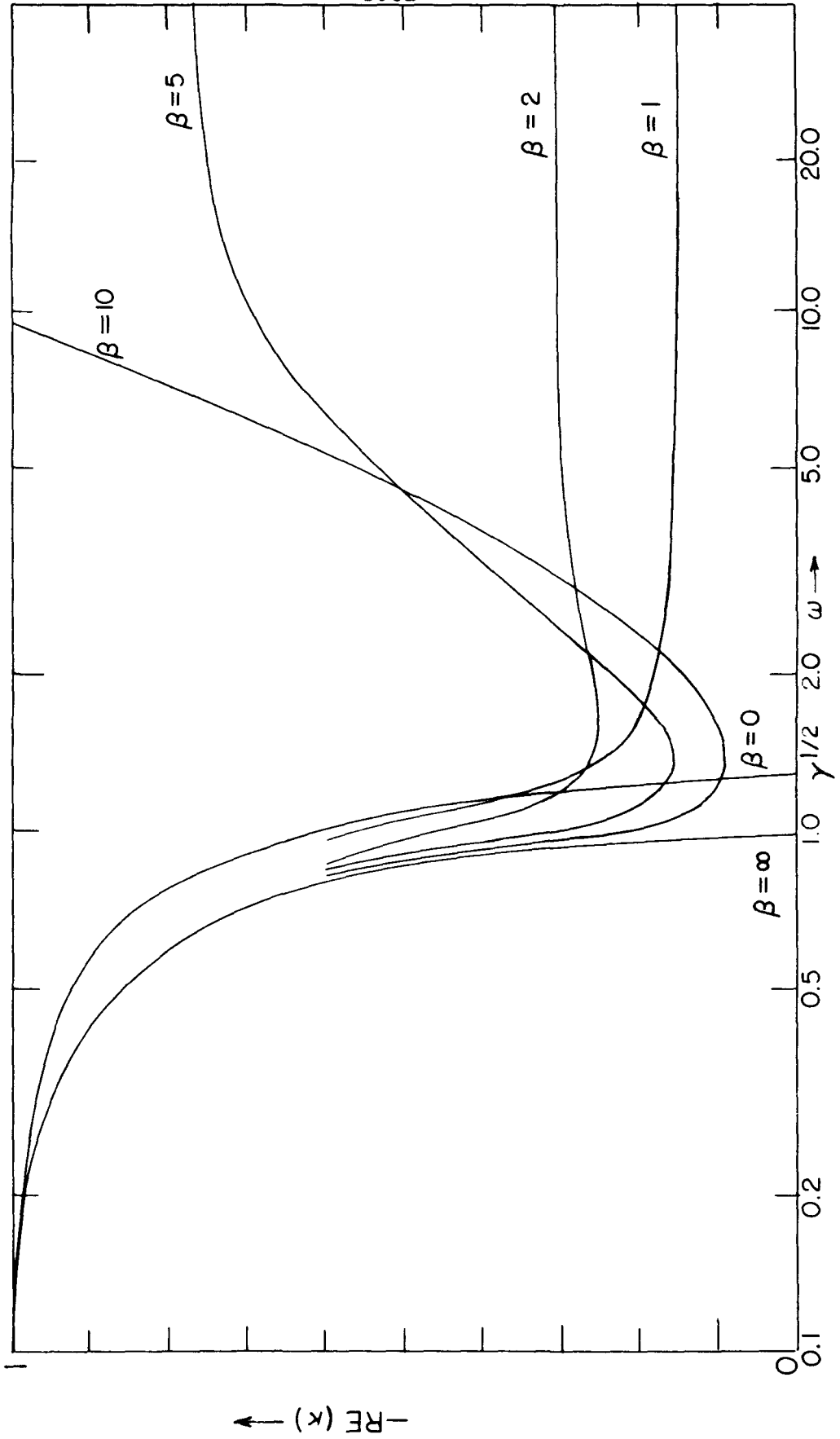


Figure 4-7. Attenuation =  $-\text{Re}(k)$ , plotted versus  $\omega$  for various values of  $\beta$ .

and that the phase by which the temperature oscillation lags the velocity oscillation is given by

$$\varphi = \pi - \delta - \psi \quad (4.43)$$

where

$$q = re^{i\delta} \quad \text{and} \quad \psi = \tan^{-1} \frac{w}{\beta} \quad (4.44)$$

The amplitude and phase of the temperature are plotted versus  $\beta$  for various values of  $w$  in Figure 4-8. For later use we have also shown on the abscissa the values of  $z$  to which the different values of  $\beta$  correspond.

We see from Figure 4-8 that the amplitude is small for low frequencies or short radiative decay times, and large for high frequencies or long radiative decay times, as we should expect. Concerning the phase, we see that: (a) for high frequencies ( $\omega \rightarrow \infty$ ,  $\omega \gg \beta$ ) the temperature and velocity are in phase. This is the usual result for an adiabatic wave propagating in an atmosphere without gravity. (b) For very low frequencies ( $\omega \ll 1$ ,  $\omega \ll \beta$ ), the temperature lags the velocity by  $180^\circ$ . For  $\omega = \omega_c = 1$ , the temperature lags the velocity by  $90^\circ$  for  $\beta \rightarrow 0$  (adiabatic) and by  $180^\circ$  for  $\beta \rightarrow \infty$  (isothermal).

#### E. The Thermal Properties of the Oscillation

In this section we shall try to apply the results of the preceding analysis to our observational data. We shall begin by briefly summarizing the data already presented in Part III concerning the

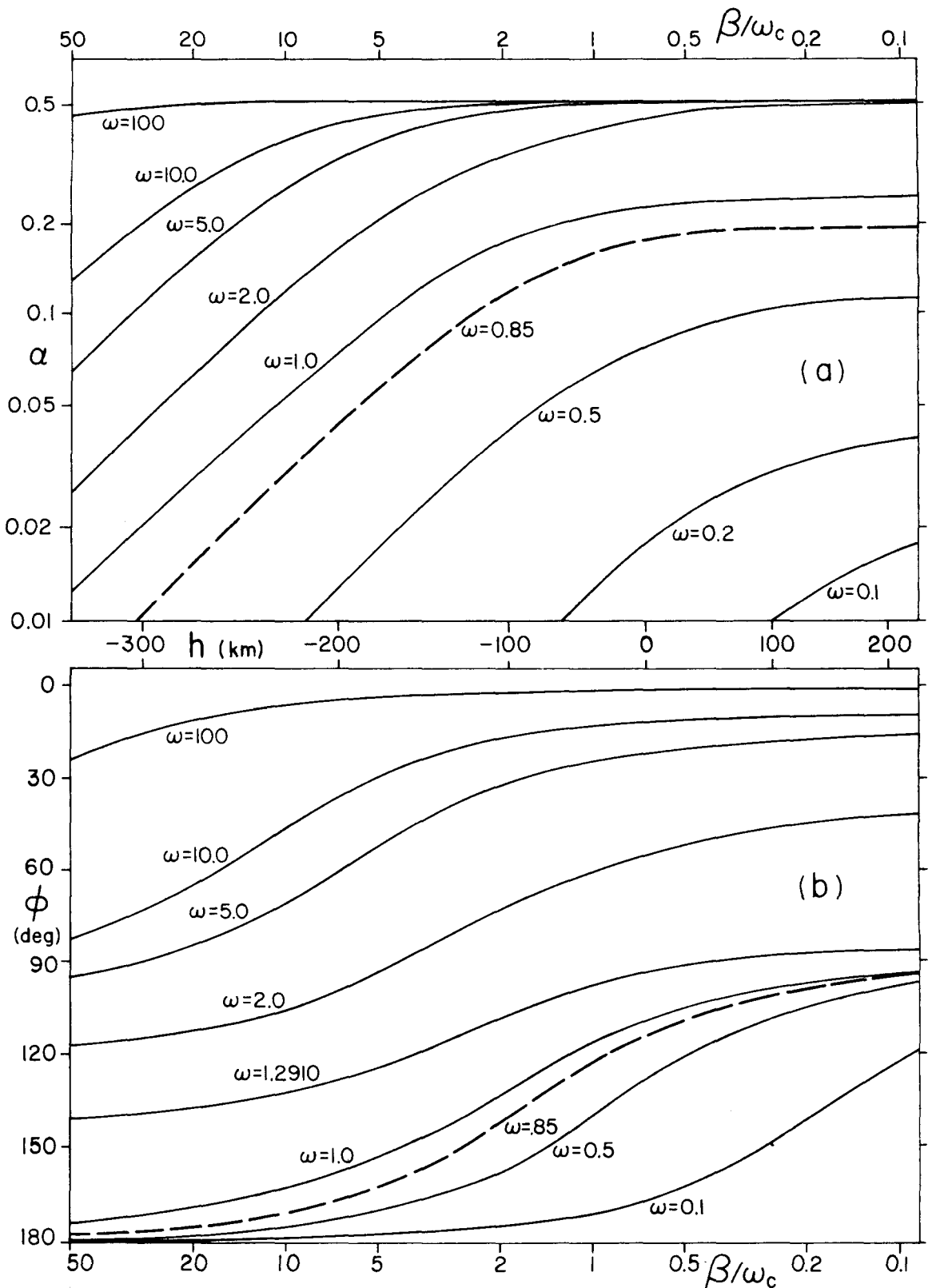


Figure 4-8. (a) Amplitude  $\alpha$  and (b) phase lag  $\phi$  of the temperature oscillation relative to the velocity oscillation, plotted vs  $\beta/\omega_c$  (axes at top and bottom), and vs height  $h$  at which these values of  $\beta/\omega_c$  exist (middle axis).

brightness-velocity correlation and the periodicity of the brightness field.

It will be recalled that a brightness-velocity correlation was observed with a correlation coefficient which decreases apparently monotonically with height from about +0.5 in the lower photosphere through zero and to about -0.2 at the highest elevation where the velocity oscillation can be detected. The reverse of sign appears to occur at an elevation spanned by the heights of formation of the outer and inner Na5896 line wing. The brightness field alone exhibits a time correlation function which decays monotonically with a "half-life" of a few minutes at lower altitudes, but which oscillates with a period of about 260 seconds at the altitude of the Na5896 line core. The oscillation of the brightness field may be followed to considerably higher altitudes, and exhibits a period which appears to decrease slowly with increasing altitude. At the altitude of the Na5896 line, the oscillation in the core appears to be roughly 180° out of phase with the velocity oscillation. Finally, the rms amplitude of the brightness fluctuations seems to increase rather slowly with altitude in the photosphere. In the chromosphere, the amplitude of the brightness oscillation (as distinct from the non-oscillatory chromospheric mottling) appears to decrease with altitude, until above the level of the Ca<sup>+</sup> 3933 core, the periodicity is no longer observed at all.

In the following discussion of the interpretation of these observations, we shall make the assumption that increased brightness in the spectral line is proportional to an increase in temperature at the altitude of observation. We emphasize again that this assumption is at most only approximately valid, for the source function in a given line may be a rather complicated function of temperature, gas and electron pressure, the excitation potential of the lower state of the transition, and the ionization potential. The last two parameters in particular vary from line to line even at the same altitude. Nevertheless, our crude assumption is probably adequate for a rough qualitative treatment. In addition, the fact that the brightness fluctuations and their correlation with the velocity vary rather smoothly with height through the atmosphere suggests that they reflect a property of the atmosphere itself rather than of the particular line being studied.

The positive brightness-velocity correlation observed at lower levels has been reported earlier by several authors (31, 32), and may be interpreted as being due to the close association of low-lying atmospheric levels with the granulation itself, i. e., with the top of the convection zone. Because the granulation transports heat by convection, the rising material is hotter, or brighter, than average, while falling material is cooler.

In actuality, the motions in the convectively stable atmosphere

even immediately above the granulation do not mimic the temperature fluctuations of the granulation exactly; we observe an oscillatory motion in the spectral lines, while there is no sign of any periodicity in the time correlation of the photospheric granulation field (11). Also, as we have reported on page 79 we see no sign of a periodicity in intensity of the spectral line at these elevations. Nevertheless, it is not hard to see how the time correlation function between a decaying velocity oscillation and a non-oscillatory decaying temperature perturbation may still be positive. For instance, the heating due to the appearance of bright granule may cause an increase of pressure which lifts the atmosphere directly above, initiating the velocity oscillation; the first motion is upward, and due to the decay with time of the oscillation amplitude, as well as granulation-induced temperature perturbation, the first motions contribute more to the time averaged correlation coefficient than subsequent motions, yielding a net positive correlative coefficient.

At higher levels, however, the heating of the atmosphere due to the granule should be lessened because of the decreased solid angle subtended by the granule, and thus the rms amplitude of granulation-induced fluctuations may be expected to decrease with height. (In addition, the heating of higher layers will be delayed by the longer relaxation time, causing the granulation-induced temperature fluctuations to be less well correlated with the velocity.) The fact that

we observe, if anything, an increase of rms temperature variation with height suggests another source of temperature fluctuation; our observation that there is an oscillatory component to the brightness field even when no oscillation has been detected in the granulation gives strength to this suggestion. In addition, the observations that this oscillation is approximately out of phase with the velocity oscillation, i. e., is negatively correlated with it, explain how this second source of brightness fluctuation, when it overrides the first, can cause the total brightness-velocity correlation coefficient to become negative.

In the previous section we determined the amplitude and phase of the temperature oscillation associated with a wave of frequency  $\omega$ , travelling vertically through an isothermal atmosphere, with a radiative decay time  $\frac{1}{\beta}$  which is independent of  $z$ . Now as we have already seen (cf. Fig. 4-5),  $\beta$  actually varies throughout the height of the solar atmosphere; indeed,  $\beta$  may change by an order of magnitude in a distance considerably less than a wavelength of the propagating wave. Nevertheless, it seems reasonable to expect as a first approximation that the amplitude and phase will be appropriate to some average radiative decay time characteristic of the height of observation.

Proceeding in this spirit, we then find that at low levels the amplitude of the temperature oscillation for frequencies of interest is extremely small due to the rapid radiative relaxation time. Only when  $\beta$  and  $\omega$  become comparable does the temperature oscillation become significant. Figure 4-9 shows the values of  $\theta = \frac{\Delta T}{T}$  predicted for the different heights of observation and for the observed frequency,  $\omega \sim 0.85$ , from the data in Figure 4-8(a). Also plotted in the figure are

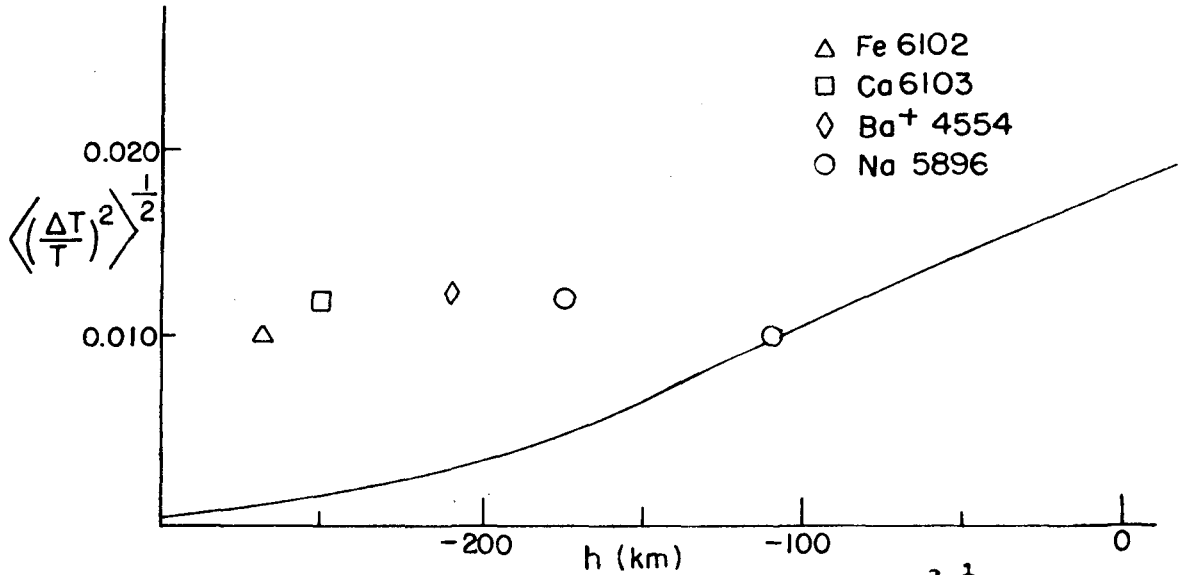


Figure 4-9. Solid line: Predicted values of  $\langle (\Delta T/T)^2 \rangle^{1/2}$  for a wave of frequency  $\omega = 0.85$ , the observed amplitude (Fig. 3-3) and a radiative decay time dependent on height (Fig. 4-5). Separate points: Observed values of  $\langle (\Delta T/T)^2 \rangle^{1/2}$ . Difference is due to heating by granulation.

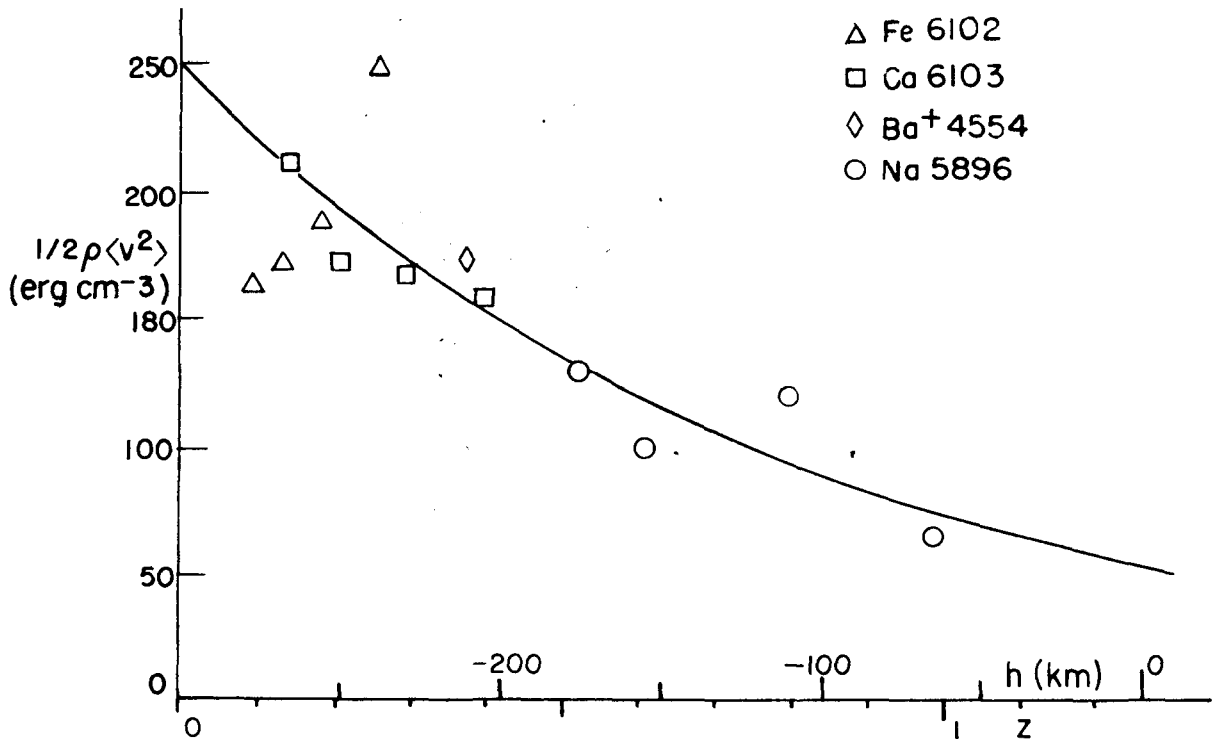


Figure 4-10. Observed values of average kinetic energy per  $\text{cm}^3$ ,  $E = \frac{1}{2} \rho \langle v^2 \rangle$ , versus height  $h$  above  $\tau = 0.003$  and versus non-dimensional height  $z$ . Solid line:  $E = 250e^{-1.25z}$ .

the observed values of  $\frac{\Delta T}{T}$ . The difference between the two curves represents the direct heating by the granulation. It is seen that at the level of the Na 5896 line wing, the difference goes to zero, i. e., all the temperature fluctuations could be supplied by the quasi-adiabatic heating of the wave.

If we examine the phase of the temperature oscillation with respect to the velocity oscillation, as portrayed in 4-8(b), we see that for our observed frequency,  $\omega \sim 0.85$ , the phase lag varies from  $\sim 180^\circ$  in the photosphere to  $\sim 110^\circ$  in the low chromosphere. At the level of the Na5896 line wing the phase lag should be about  $140^\circ$ . This is to be compared with our observed lag of about  $170^\circ$ .

One other observational point is available for comparison with the simple picture we have drawn: Evans and Michard (24) have determined the phase lag between the temperature and velocity oscillations in the low chromospheric line Fe5171 to be about  $90^\circ$ . The oscillation period which they measure for this line is about 275 sec, giving a dimensionless frequency  $\omega \sim 0.9$ . Thus from Figure 4-8(b) we would predict a phase lag of about  $115^\circ$ .

We interpret the discrepancies between the above observations and our expectations to be due to the extreme over-simplifications we have allowed in deriving this qualitative description of the thermal properties of the oscillation. We can scarcely expect such a picture to produce detailed agreement with observations. Nevertheless, it does have the appeal that it seems to explain the otherwise very puzzling reversal of the brightness-velocity correlation in the low chromosphere. We have already implied how this might come about, and now we shall

spell it out explicitly:

If the compressions associated with the velocity oscillation were the only source of heating, the brightness-velocity correlation coefficient  $C$  would be simply  $C = \cos \varphi$  where  $\varphi$  is the phase angle between the two oscillations.  $C$  would vary between  $-1.0$  and  $0.0$  as the height varies from the granulation up into the chromosphere. The combined effects of direct heating by the granulation and quasi-adiabatic heating by the oscillation will create a correlation coefficient which is positive at low-lying levels where the granulation heating predominates. As one proceeds to higher levels, the granulation heating decreases and the oscillatory compressional heating increases, causing the negatively correlated oscillatory brightness field to predominate, and therefore causing the net correlation coefficient between brightness and velocity to become negative.

Finally, we have evaluated the kinetic energy per unit volume,  $\frac{1}{2} \rho \langle v^2 \rangle$ , at various elevations, using the observed mean square velocities, and densities from Allen's model (7). Our results are graphed in Figure 4-10. If there were no losses or reflections, we should obtain a horizontal line. If there are radiative losses only, we may calculate the values of  $\alpha$  and  $\beta$  which would give rise to the observed energy loss. The graph of energy versus height shown in

Figure 4-10 can be approximately fitted by a curve

$E = \frac{1}{2} \rho \langle v^2 \rangle \sim e^{-1.25z}$ . Since  $\rho \sim e^{-2z}$  (by choice of the unit of  $z$  as  $\frac{1}{2H}$ ), we must have  $\langle v^2 \rangle^{\frac{1}{2}} \sim e^{0.375z}$ . (This, of course, agrees with our earlier graph of observed rms velocity versus height (Fig. 3-3, p. 43a).) Therefore, to match the observed decrease of kinetic energy we would need to have  $1 + \text{Re}(\kappa) = 0.375$ , or  $\text{Re}(\kappa) = -0.625$ . From Figure 4-6, we find the value of radiative decay time  $\frac{1}{\beta}$  necessary to achieve this for various values of  $\omega$  to be:

$\omega / \omega_c$	$1/\beta$ (sec)
1	125
0.9	54
0.8	17

We may conclude that if most of the energy is in a frequency interval slightly less than the critical frequency (as we seem to observe), then reasonable values of radiative decay time could indeed provide the observed losses of energy.

We now summarize our discussion by presenting the following simplified picture of the temperature fluctuations in the solar atmosphere:

The temperature field consists of a non-oscillatory and an oscillatory part. The non-oscillatory part, which predominates at lower altitudes, is just the direct heating by hot granules immediately below. Because in the initial stages of a granule life the heating is

greatest and because the first motion induced on the atmosphere is upward, this non-oscillatory brightness field exhibits a positive correlation with velocity. The correlation is especially strong in layers immediately above the granulation. At higher levels, which are not so closely coupled with the granulation, this correlation presumably decreases. Also the heating by granules decreases with increasing height due to the increased distance from the granules, and above a certain level a second source of atmospheric heating, which increases rather than decreases with height, becomes more important. The second source of heating is the quasi-adiabatic compression of the velocity waves, and depends on the ratio of the radiative relaxation time to the oscillation period. The radiative relaxation time increases with altitude, causing the amplitude of thermal oscillation to increase also. The thermal oscillation lags the velocity oscillation by between  $90^\circ$  and  $180^\circ$ , thus introducing a negative brightness-velocity correlation at high altitudes. In addition, the combination of the two intensity fields causes a net rms intensity fluctuation which increases rather than decreases with altitude. Losses and reflections, however, seem to prevent the wave from penetrating above about the level of the  $\text{Ca}^+ 3933$  line core ( $z \sim 3000$  km).

This picture, being based on a very much simplified model of the thermal properties of the atmosphere, cannot avoid being wrong in

the details. Whether it will be found to be correct even approximately will depend very much on future observations, especially of the phase and amplitude relations between the brightness and velocity oscillations. At present, it can be accepted only as a reasonable hypothesis, based on a rather limited number of observations.

### F. Conclusion

In this thesis we have reported on the first direct observation of the presence of vertical acoustic waves in the solar atmosphere. We have measured the average period of the oscillatory wave motions with some accuracy and have seen a variation of this period with altitude. In the chromosphere we found a periodic change of intensity accompanying the velocity oscillation, and we have attributed this to the quasi-adiabatic heating by the compressional wave. Also we found a correlation coefficient between intensity and velocity which varies in a regular way throughout the atmosphere. We have tried to understand the temperature variations and their correlation with velocity in terms of the thermodynamic properties of an acoustic wave propagating in an atmosphere with radiative leakage.

Much remains to be done, both observationally and theoretically. The chief observational questions suggested by the present investigation are:

- 1) What is the actual frequency spectrum at each altitude? Which frequencies represent standing waves, and which represent

travelling waves, i. e., what is the critical frequency?

2) The time lag between the effects of the wave at low altitudes and at high altitudes should be thoroughly investigated. Also the phase relations between the intensity and velocity oscillation will tell much about the propagation characteristics of the wave. A superb start on these problems has already been made by Evans and Michard at Sacramento Peak (24).

3) The amplitude of both the velocity and intensity oscillations should be more carefully determined for different altitudes, in order to clear up the problem of energy transport by the wave. Also, the "decay time" of the oscillation for separate frequencies should be measured. Following the time history of the velocity oscillation at individual points may indicate whether the motion can be represented by a decaying sine wave or whether it has a more complicated behavior. Also, such measures should determine to what extent the decay of the oscillation of the velocity time correlation function is due to actual damping, and to what extent it is due to changes of phase. Howard has already made some observations of this type with the Babcock magnetograph, set in the Doppler mode (25).

4) The three-dimensional properties of the wave should be more thoroughly investigated. What can one say about waves propagating at an angle with the vertical? What evidence can we find of horizontal as well as vertical propagation of the waves? Is the

apparent difference in size between the elements of the velocity field and of the intensity field real? How reliable is our observation that the horizontal velocity component essentially disappears at high altitudes? Can we elucidate the apparent spreading-out of the waves as they progress upward, as implied by the increase of size of the elements of the velocity field with height?

5) The oscillatory motions should be followed up into the chromosphere as far as possible, with special attention being paid to the energy transport properties of the wave. In the medium and upper chromosphere we should look for the interaction of magnetic fields with the waves. What is the relation between the acoustic wave and the solar spicules? Are the latter simply the high altitude extension of the acoustic waves, for instance? Might the most energetic spicules be generated by interaction of acoustic waves and magnetic fields? We have seen that magnetic fields in plage regions damp out the wave; what is the effect of the magnetic fields associated with the "chromospheric emission network" on the acoustic waves? What, if any, is the connection between the acoustic waves and the large-scale, rapidly-changing velocity pattern found in the H $\alpha$  line?

The observational problems attendant upon investigating such questions are manifold, but none of them seem insurmountable, given proper refinement of existing techniques, both spectrographic and spectroheliographic.

The chief theoretical questions which suggest themselves are:

1) The discussion we have just presented greatly needs refining. Ideally, of course, the full differential equation of motion, allowing for the variation of equilibrium temperature and radiative decay time with height, for the three-dimensional properties of the wave, for more realistic initial conditions, etc., should be investigated. A less ambitious line of approach might be to introduce velocity fields with various frequency spectra at  $z = 0$  and examine the time correlation function of the response at different values of  $z$ . Krasberg and Whitney (30) have idealized the atmosphere as divided into parallel slabs of different temperature and absorption coefficients, and investigated the thermal relaxation properties at different points in the atmosphere. Perhaps the propagation of a thermal-acoustic wave through such an atmosphere can be investigated in a similar fashion.

2) It would be interesting to investigate what the observations can tell us about the equilibrium structure of the solar atmosphere itself. If we could derive the critical frequency from our observations and similar ones, we could use it to determine better the scale height  $H = \frac{RT}{\mu g}$ . In turn, this will lead to a more accurate picture of the variation of temperature  $T$  and molecular weight  $\mu$  in the atmosphere. Perhaps observations of phase lags between the velocity or intensity oscillations in different lines will help to determine better the relative heights of formation of these lines. Many of the parameters we

observe--velocity amplitude, average period, brightness-velocity correlation, average size, etc. --vary in a regular way through the atmosphere; both a relative and an absolute ordering of heights of formation might be possible through the use of such data.

3) Finally, our observations may have some bearing on the very difficult problem of support and heating of the chromosphere and corona. Especially relevant are the questions of mechanical energy flux into the chromosphere and corona versus reradiation and conduction back down to lower levels, of the interaction between acoustic waves or shock waves and hydromagnetic waves, and the whole problem of the origin and life history of spicules. Much work has, of course, been done on these problems (12, 13, 23), but hopefully our observations may suggest some new approaches.

## APPENDIX I. RESOLUTION OF THE SPECTROHELIOGRAPH

In this appendix we shall discuss some observations and theoretical studies of loss of resolution in the Mt. Wilson 13-foot spectroheliograph.

A number of factors contribute to a degradation of the resolution of the solar image between the initial image formed at the entrance slit and the final monochromatic image laid down on the photographic plate above the second slit. In approximate order of decreasing importance, these are: (1) The curvature of the focal surface of the collimating lens-camera lens system, (2) the geometrical smearing of the image due to the non-zero width of the entrance and exit slits, (3) the gap between the exit slit and the plate emulsion, and (4) finite resolving power of the lenses and grating. We shall now discuss these separate factors in turn.

### (A) Curvature of the Focal Surface of the Spectroheliograph

One of the third order aberrations in the camera and collimating lens is curvature of the focal surface of the image of the second slit; the focal length is shortest for the rays making the largest angle with the axis of the system. Figure A1-1(a) represents a plot of the focal surface as measured visually and photographically at the spectroheliograph for various wavelengths. The diameter of the

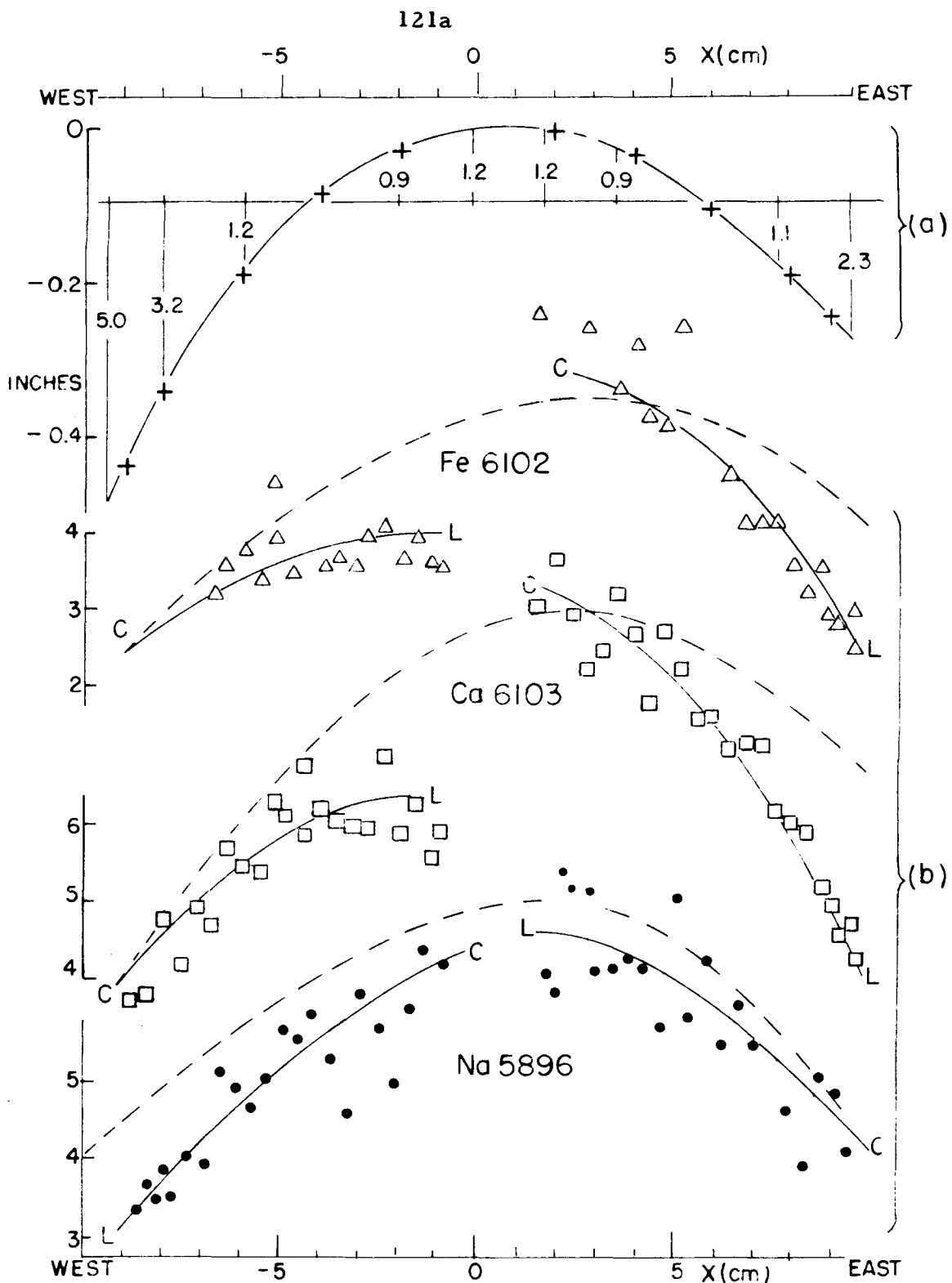


Figure A1-1. (a) Focal surface at spectroheliograph exit slit.  $X$  = coordinate along slit. Numbers give diameter of circle of confusion at the slit in sec arc. (b) Logarithmic slopes of line profiles, measured at different points on actual plates. Variation in slope is partly due to variation of intrinsic profile from center (C) to limb (L). Dashed lines indicate the approximate effect of slits alone.

resultant circle of confusion of the image at the slit is also plotted in the figure, for the case where the lenses are set to give the best focus at points midway between the ends and the center of the slit.

The curvature of the focal surface has a deleterious effect on spectral line resolution as well as the resolution of spatial detail on the image. Figure A1-1(b) is a plot of the slope  $dnT/d\lambda$  of the line profiles for Fe6102, Ca6103, and Na5896 at the offsets from the line cores usually used, versus distance from the center of the slit.

From the data presented in Figure A1-1 we see that there can be a loss of resolution of as much as several seconds or arc at the edges of an image, if the center is in focus, and also a degradation of the line profile. It should also be noted that when two images, exposed side by side on the slit, are cancelled, a portion exposed near the center of the slit is placed in register with a portion exposed near the end of the slit; one must be on guard against interpreting differences of detail at corresponding points of the image as reflecting a property of the sun before investigating the possible results of unequal resolution.

#### (B) Resolution Loss Due to Finite Slit Widths

The total energy  $E(y, z)$  received by a point  $(y, z)$  of the photographic plate when the spectroheliograph is set at a wavelength  $\lambda$  will be a "smearred-out" reproduction of the monochromatic intensity

$I(y, z, \lambda)$  striking the corresponding point of the solar image at the first slit. The geometrical smearing due to the two slits, each of width  $a$ , may be easily calculated (Fig. A1-2). If the spectroheliograph scans at velocity  $v$ , the intensity  $I(y, z, t)$  below the second slit at any time is found by integrating over the range in  $x$  occupied by the first slit at that instant:

$$I(y, z, t) = \int_{vt - \frac{a}{2}}^{vt + \frac{a}{2}} I_0(x, z, \lambda + [(y - vt) - \beta(x - vt)]D) dx \quad (A1.1)$$

$D$  is the dispersion of the spectrograph, and  $\beta = \frac{d\theta_{diff}}{d\theta_{inc}} = \frac{\cos \theta_{inc}}{\cos \theta_{diff}}$

is a factor which takes care of the magnification of the monochromatic image of the slit along the spectrum due to the grating (Fig. A1-3).

The total energy received by a point on the plate is the integral of the intensity  $I(x, z, t)$  over the time that the second slit is passing it:

$$E(y, z) = \int_{\frac{y-a/2}{v}}^{\frac{y+a/2}{v}} I(y, z, t) dt = \int_{\frac{y-a/2}{v}}^{\frac{y+a/2}{v}} \int_{vt - \frac{a}{2}}^{vt + \frac{a}{2}} I_0(x, z, \lambda + [y - vt - \beta(x - vt)]) dx dt \quad (A1.2)$$

$E(y)$  is displayed for various simple one-dimensional inputs  $I(x, \lambda)$  in Figure A1-4.

A more realistic case, representing the decomposition of the spatial intensity and velocity field into its Fourier components  $A(\underline{k})$  and  $v(\underline{k})$ , would have, if the second slit were situated on the wing of a

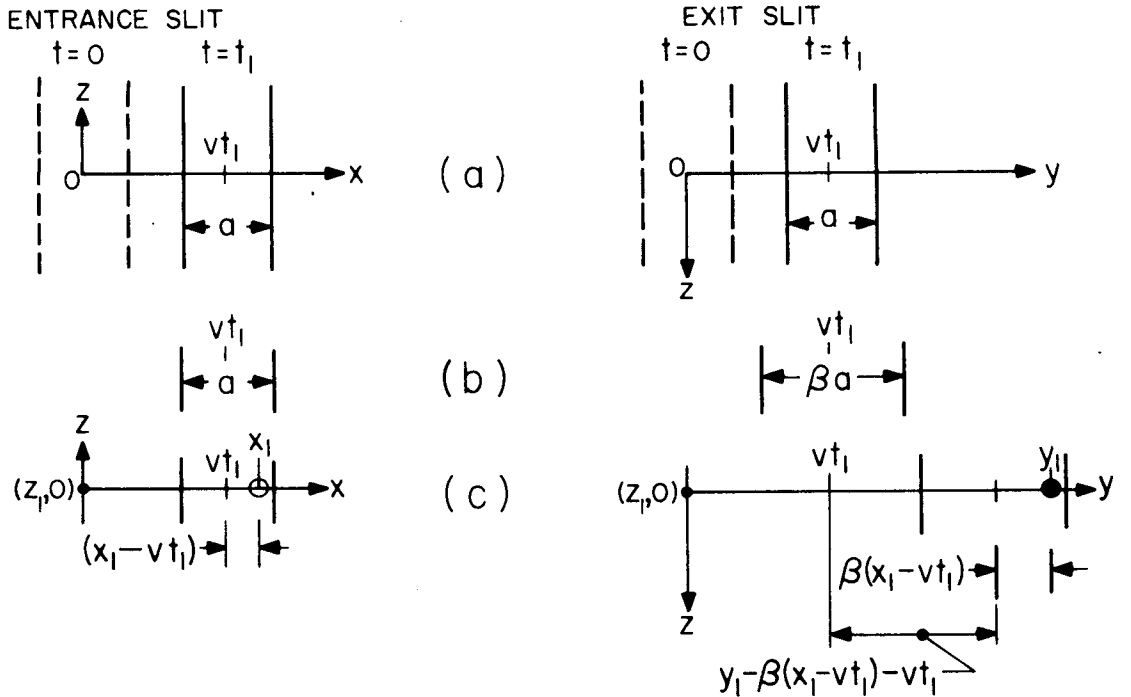


Figure A1-2. Geometry of spectroheliograph slits. (a) slit coordinates at  $t=0$  and  $t=t_1$ .  $V$  = velocity of spectroheliograph. (b) Monochromatic image at exit slit of entrance slit, at time  $t_1$  and wavelength  $\lambda_0$ . Image magnified by  $\beta$  due to grating dispersion. (c) Image (●) at  $(y_1, z_1)$  of source (○) at  $(x_1, z_1)$ , at the wavelength  $\lambda_0 + D[y_1 - \beta(x_1 - vt_1) - vt_1]$ , where  $D$  = dispersion.

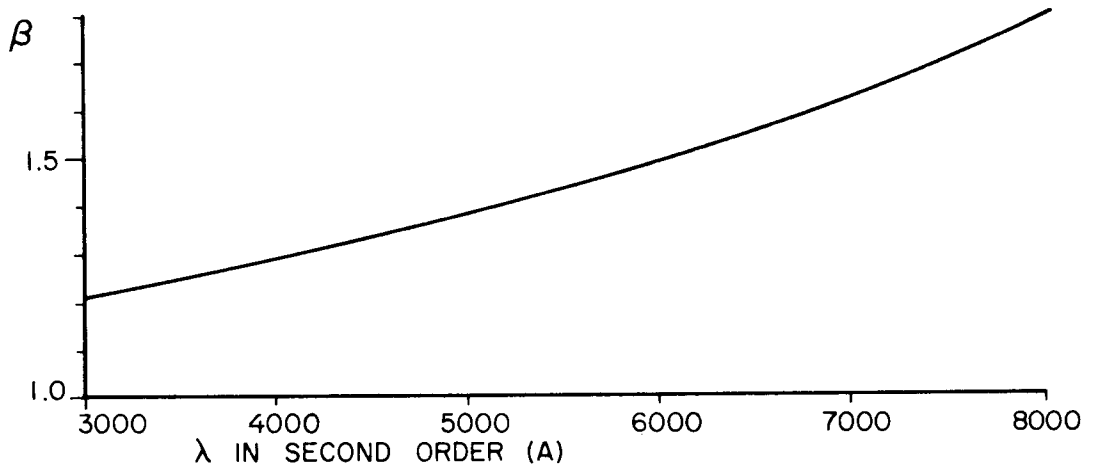


Figure A1-3. Magnification  $\beta$  at the exit slit of the monochromatic image of the entrance slit, plotted versus  $\lambda$ .

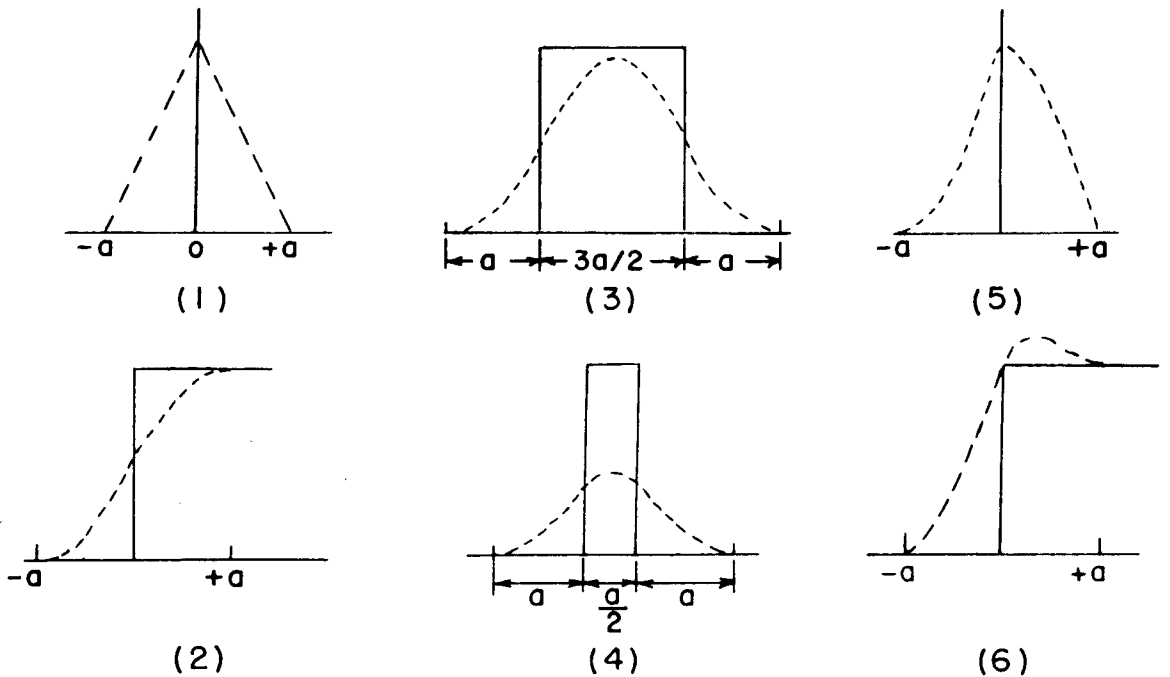


Figure A1-4. "Response" (-----) at the photographic plate to various "Input" (——) functions. (1) - (4): Second slit in continuum; inputs are  $\delta$ -function, step function, and two double-step functions. (5), (6): Second slit set on a spectral line wing with slope  $\frac{\beta+1}{2} \frac{aD}{\Delta} = 0.5$ ; inputs are  $\delta$ -function and step function.

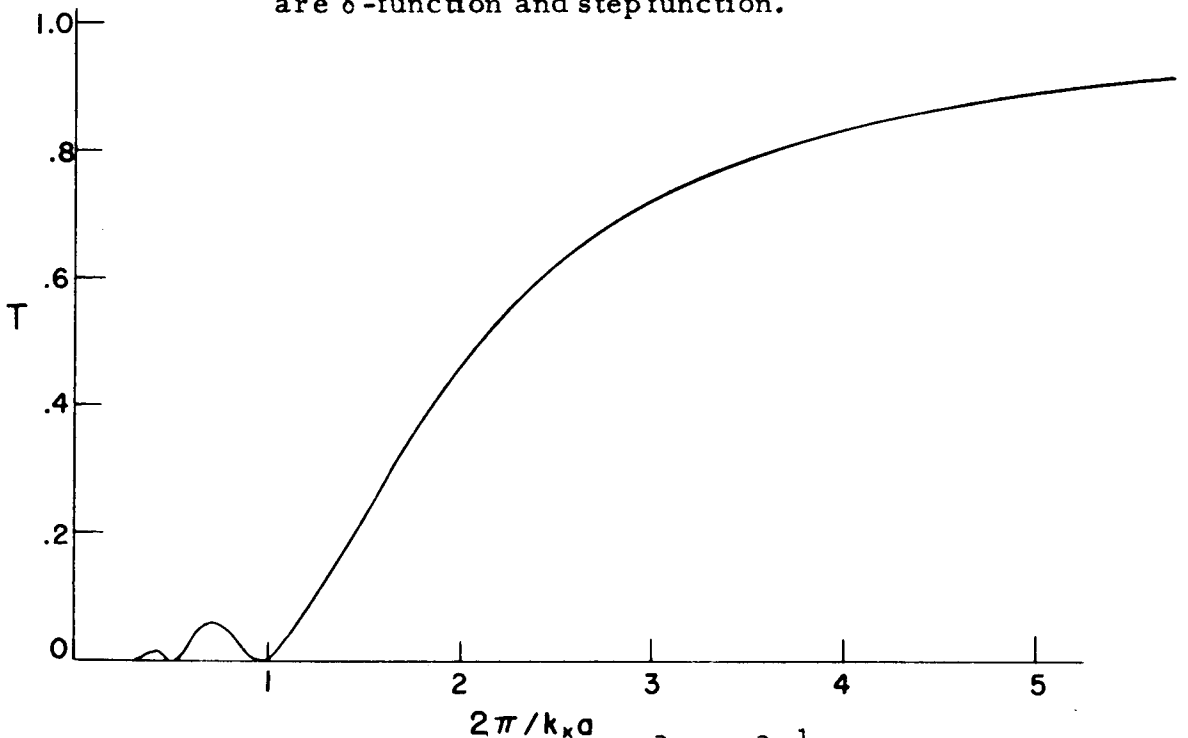


Figure A1-5. Transmittance  $T = [T_1^2 + T_2^2]^{\frac{1}{2}}$  where  $T_1$  and  $T_2$  are defined on p. 125. Abscissa is the ratio of the size of image detail to the slit width.

spectral line whose profile had the logarithmic slope  $\frac{1}{I} \frac{dI}{d\lambda} = \frac{1}{\Delta}$ ,

an "input" function

$$I(x, z, \lambda) = I_0 \left( 1 + \int A(\underline{k}) e^{i \underline{k} \cdot \underline{r}} d^2 \underline{k} \right) \left( 1 + \frac{\beta(x-vt) - (y-vt)}{\Delta} D + \frac{\lambda}{\Delta} \int \frac{v(k')}{c} e^{i \underline{k}' \cdot \underline{r}} d^2 \underline{k}' \right) \quad (A1.3)$$

Carrying out the operations involved in equation A1.2, we find the "response" to be

$$\begin{aligned} \frac{v}{a} E(y, z) = & 1 + \int \left[ A(\underline{k}) + \frac{\lambda}{\Delta} \frac{v(k)}{c} \right] \frac{\sin^2 \left[ \frac{k a}{2} \right]}{\left( \frac{k a}{2} \right)^2} e^{i \underline{k} \cdot \underline{r}} d^2 \underline{k} \\ & + \frac{(\beta+1)}{2} \frac{aD}{\Delta} \int A(\underline{k}) \frac{\sin \left[ \frac{k a}{2} \right]}{\frac{k a}{2}} e^{i \underline{k} \cdot \underline{r}} \frac{\cos \left[ \frac{k a}{2} \right] - \frac{\sin \left[ \frac{k a}{2} \right]}{\frac{k a}{2}}}{i \frac{k a}{2}} d^2 \underline{k} \\ & + \int \int A(\underline{k}) \frac{v(k')}{c} \frac{\lambda}{\Delta} e^{i(\underline{k} + \underline{k}') \cdot \underline{r}} \frac{\sin^2 \left[ \frac{k + k'}{2} \frac{x}{a} \right]}{\left[ \frac{k + k'}{2} \frac{x}{a} \right]^2} d^2 \underline{k} d^2 \underline{k}' \quad (A1.4) \end{aligned}$$

From this rather complicated result we may make the following observations:

- a) Spatial wavelengths  $\lambda = \frac{2a}{k} = \frac{a}{n}$  are not transmitted at all through the spectroheliograph.

b) If the second slit is set in the continuum ( $\Delta = \infty$ ), the input is

$1 + \int A(\underline{k}) e^{i \underline{k} \cdot \underline{r}} d^2 \underline{k}$  and the output is

$1 + \int A(\underline{k}) \frac{\sin^2 \left[ \frac{k_x a}{2} \right]}{\left( \frac{k_x a}{2} \right)} e^{i \underline{k} \cdot \underline{r}} d^2 \underline{k}$ . We define the "transmittance func-

tion" to be

$$T_1(\underline{k}) = \frac{\sin^2 \left[ \frac{k_x a}{2} \right]}{\left( \frac{k_x a}{2} \right)} \quad (\text{A 1.5})$$

c) If the spectroheliograph is set on the wing of a spectral line,

the same transmittance function operates on the velocity field, as

shown b, the second half of the second term of equation A1.4.

d) The third term of equation A1.4 gives the influence of the spectral line slope on the intensity field. We define the transmittance function

$T_2(\underline{k})$  as

$$T_2(\underline{k}) = \frac{\sin \left[ \frac{k_x a}{2} \right]}{\frac{k_x a}{2}} \frac{\cos \left[ \frac{k_x a}{2} \right] - \frac{\sin(k_x a/2)}{\frac{k_x a}{2}}}{\frac{k_x a}{2}} \cdot \frac{(\beta+1) \frac{aD}{\lambda}}{\frac{k_x a}{2}} \quad (\text{A 1.6})$$

The net transmittance of the solar intensity field  $A(\underline{k})$  is

$T = (T_1^2 + T_2^2)^{\frac{1}{2}}$ ; this is plotted in Figure A1-5, for the Na5896 line with 0.07 mm slits, for which  $\frac{\beta+1}{2} \frac{aD}{\lambda}$  assumes the value 0.8.

e) The last term gives the influence of the velocity field on the

brightness field and vice versa. Since typical maximum values for  $A(k)$  and  $\frac{v(k)}{c} \frac{\lambda}{\Delta}$  are found to be less than 0.1, this is a second order effect and may be neglected.

It should be noted that for small spatial wavelengths a Doppler cancellation does not fully cancel out the brightness field. In the discussion on photographic reduction in Part II (p. 26), we find that the transmission of a Doppler cancellation is  $T = \left[ \frac{E(+\Delta)}{E(-\Delta)} \right]^\Gamma$  where  $\Gamma$  is the contrast of the original plate. (Since the second slit is set equidistantly on either wing of a spectral line,  $\Delta$  is opposite for the two images.) From equation A1.4 we see that this is approximately

$$T \approx 1 + \frac{2\Gamma\lambda}{\Delta} \int \frac{v(k)}{c} \frac{\sin^2 \left[ \frac{kx}{2} \right]}{\left( \frac{kx}{2} \right)^2} e^{i k \cdot r} d^2 k \quad (A1.7)$$

$$+ 2\Gamma \frac{\beta+1}{2} \frac{aD}{\Delta} \int A(k) \frac{\sin \left[ \frac{kx}{2} \right]}{\frac{kx}{2}} \frac{\cos \left[ \frac{kx}{2} \right] - \frac{\sin \left[ \frac{kx}{2} \right]}{\frac{kx}{2}}}{i \frac{kx}{2}} e^{i k \cdot r} d^2 k$$

For low-lying lines, as we see in Part III (p. 68 ff), the intensity contribution  $A(k)$  is larger than the velocity contribution  $\frac{v(k)}{c} \frac{\lambda}{\Delta}$ . Whenever the "seeing" is sufficiently good that elements of the order of the slit widths are resolved, the second term can become comparable to the first and could cause considerable error. Actually, for almost all the plates analyzed in this thesis, the resolution loss due to "seeing" and third-order aberrations made this effect negligible.

The finite slit widths will, of course, have a great effect on wavelength resolution as well as spatial resolution. Actual measurements of the line profile of the line Hg 4358 were made at Mt. Wilson to examine experimentally the effect of slit width on spectral line resolution. A low pressure Hg emission tube, which produces for all practical purposes infinitely sharp spectral lines, was used in the third order. The results of photometric profile measurements are shown in Figure A1-6. The observed halfwidth of each profile is very close to  $\beta a_1 + a_2$ , where  $a_1$  and  $a_2$  are the slit widths. We shall see immediately why this is so.

Figure A1-7 shows the slopes of expanded line profiles of the Ca6103 line, recorded in the same way as for an actual observation (Part II, p. 16 f). These slopes are a measure of the wavelength resolution of the instrument. We see that the resolution gets progressively better with decreasing slit width until a width (about 0.05 mm) is reached beyond which the resolution actually worsens. (We shall discuss this behavior more thoroughly in the next section.) Also, it appears that the resolution is somewhat better if the first slit has width 0.04 mm and the second 0.06 mm, rather than if both have width 0.05 mm, although both combinations pass about the same amount of light. (The effect is actually not very pronounced in Figure A1-7, due to the loss of resolution we have just mentioned when the first slit becomes less than 0.05 mm.

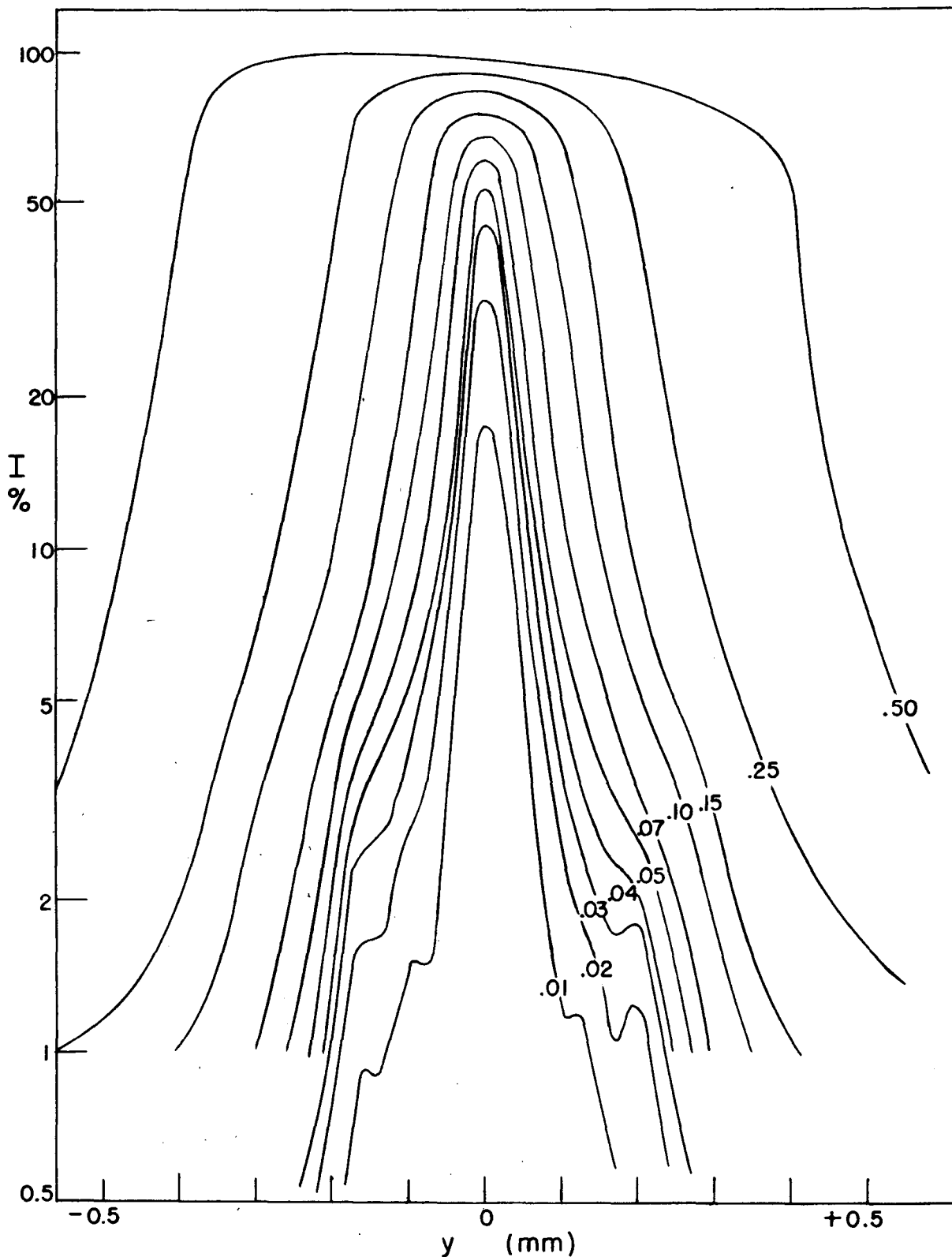


Figure A1-6. Profile of Hg4358 emission line in 3rd order. Second slit width  $a_2 = 0.01$  mm, first slit width  $a_1$  varies as shown. The half-width is approximately  $\beta a_1 + a_2 \sim \beta a_1$  for large first slit widths. Dispersion  $D = 0.90$  A/mm.

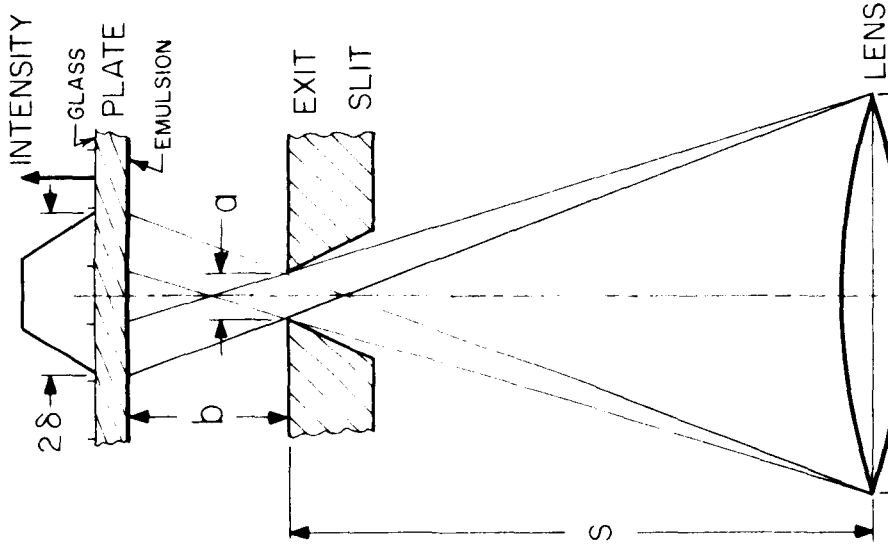


Figure A1-9. Geometry of the gap between exit slit and emulsion, which causes the intensity to be smeared over a width  $2\delta = \frac{bA}{S} + a$ .

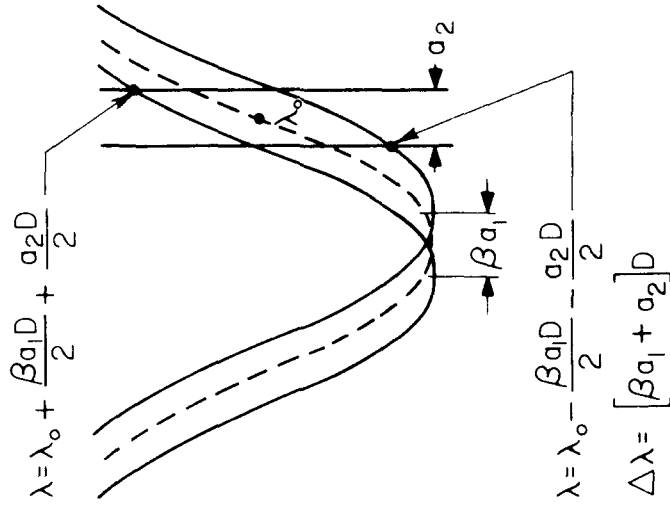


Figure A1-8. Illustrating that the wavelength interval passed by the second slit is  $\Delta\lambda = (\beta a_1 + a_2) D$ .

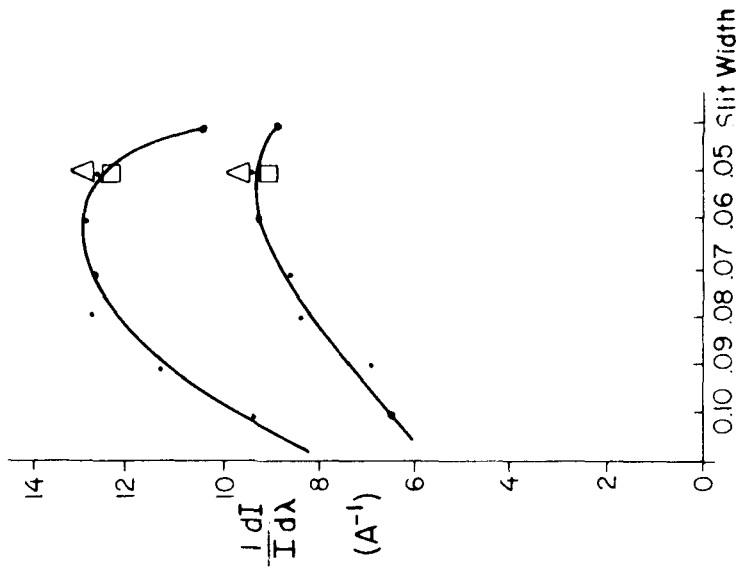


Figure A1-7. Profile slopes for Fe6102 (lower curve) and Ca6103 (upper curve) for various slit widths.  $\Delta$ :  $a_1 = .04$  mm,  $a_2 = .06$  mm.  $\square$ :  $a_1 = .06$  mm,  $a_2 = .04$  mm.

We may calculate the values  $a_1$  and  $a_2$  for the first and second slit widths which give the best resolution, subject to the condition that all combinations pass the same amount of light; i. e.,  $a_1 a_2 = \text{const.}$  Referring to Figure A1-8 and remembering that the monochromatic image of the first slit is expanded by the ratio  $\beta$  at the second slit, we see that  $\frac{\Delta\lambda}{\lambda} = \frac{(\beta a_1 + a_2)}{\lambda} D$ . Thus we wish to minimize  $\beta a_1 + a_2$ , subject to the condition  $a_1 a_2 = \text{constant}$ . This leads to  $\frac{a_2}{a_1} = \beta$ . Then the resolution  $\frac{\lambda}{\Delta\lambda} = \frac{\lambda}{2D\beta a_1} \sim 20000$  for 0.07 mm slits.

We shall see in the next section that if  $a_1 < \sim 0.05$  mm, loss of wavelength and spatial resolution occurs for other reasons. This is probably why the increased resolution for 0.04 mm and 0.06 mm slits is not more marked in Figure A1-7; the effect is, however, very easy to observe visually at the spectroheliograph.

(C) Loss of Resolution Due to the Gap between the Exit Slit of the Spectroheliograph and the Plate

The gap between the second slit and the photographic plate is about 3 mm, which is large compared to typical slit widths of 0.07 mm. Thus the width of the intensity distribution which strikes the plate may be considerably greater than the slit width. As is seen from Figure A1-9, the width  $2\delta$  of the distribution is given by  $2\delta = b \frac{A}{S} + a$ , where  $a$  is the slit width,  $b$  is the gap between slit and plate,  $A$  is the width of the light beam at the camera lens, and  $S$  is

the lens-to-image distance. When the spectroheliograph scans across the plate, the integrated intensity at a point is  $E = \int_{-\delta}^{\delta} I(x + \delta, \lambda(\delta)) d\delta$ ; spatial detail is smeared over an interval  $2\delta$ . Similarly, wavelength detail is smeared through a window  $\Delta\lambda = \frac{2\delta}{D}$ , where  $D$  is the dispersion. Inserting the values  $\frac{S}{A} = 60$  (the focal ratio of the 12 inch telescope lens, which determines the aperture stop for the 7 inch image)  $b = 0.3$  cm, and  $a = 0.007$  cm, we find  $2\delta = .12$  mm, i. e., nearly twice the slit aperture. (In 1960, when the plate was mounted 1.0 cm above the slits, the width  $2\delta$  for 0.07 mm slits was 0.24 mm, more than three times the slit width! The increase in resolution on 1961 plates consequent to decreasing the slit-to-plate gap was quite noticeable.)

The presence of a slit-to-plate gap explains another puzzling phenomenon. As the slits are narrowed, the resolution gets progressively better until a critical slit width is reached, beyond which the resolution worsens (Fig. A1-7). The explanation is that at this critical slit width the diffraction pattern of the first slit has broadened out until the central maximum fills the entire aperture of the five-inch collimating lens. Then the focal ratio of the telescope lens no longer defines the effective aperture of the camera lens, which instead becomes the full five-inch aperture. If we use the value  $S = 12.5$  ft and  $A = 5$  in., we find  $\frac{S}{A} = 30$  and the resolution window  $2\delta$  becomes (again for a 0.07 mm second slit) 0.17 mm. The slit width at which

the central maximum of the diffraction pattern occupies the entire 5-inch collimating lens may be calculated (and observed at the tower) to be about 0.04 mm. This agrees well with the experimental data on the effect of slit width on resolution (Fig. A1-7).

(D) Resolution of the Lenses and Grating

The theoretical resolution of the spectroheliograph lenses is about 1 sec arc, or 0.02 mm at the slits. The effective grating resolution is  $\frac{\lambda}{\Delta\lambda} \sim 75000$ . Therefore, the loss of resolution by these elements is far less than that due to the finite slit widths, the curvature of field of the spectrograph, or the gap between exit slit and plate. We need not consider it further.

## APPENDIX II. GHOSTS AND SCATTERED LIGHT

In this appendix we report on several measurements made at the 13-ft. spectroheliograph at Mt. Wilson in order to determine ghost and scattered light intensities.

### (A) Ghosts

Figure A2-1 illustrates the profile of the Hg4358 line in the third order, with its two strongest Rowland ghosts. This was measured photometrically at the spectroheliograph, using a low pressure mercury vapor tube as a source. It is seen that the ghost intensity is about 3.1 percent. Thus the third order contribution of the ghosts to the scattered light is about 6 percent. Since the ghost intensity varies as to the square of the order, it is about 3 percent in the second order and 0.7 percent in the first order.

There is also an indication of the presence of a weak Lyman ghost, situated about  $170 \text{ \AA}$  to the red of the spectral line, with relative strength .01 percent in second order and .02 percent in third order (Fig. A2-2).

### (B) Light Scattered Parallel to the Spectrum

Figure A2-2 illustrates a scan through the visible range of the emission spectrum of a low pressure Hg lamp. In Figure A2-3

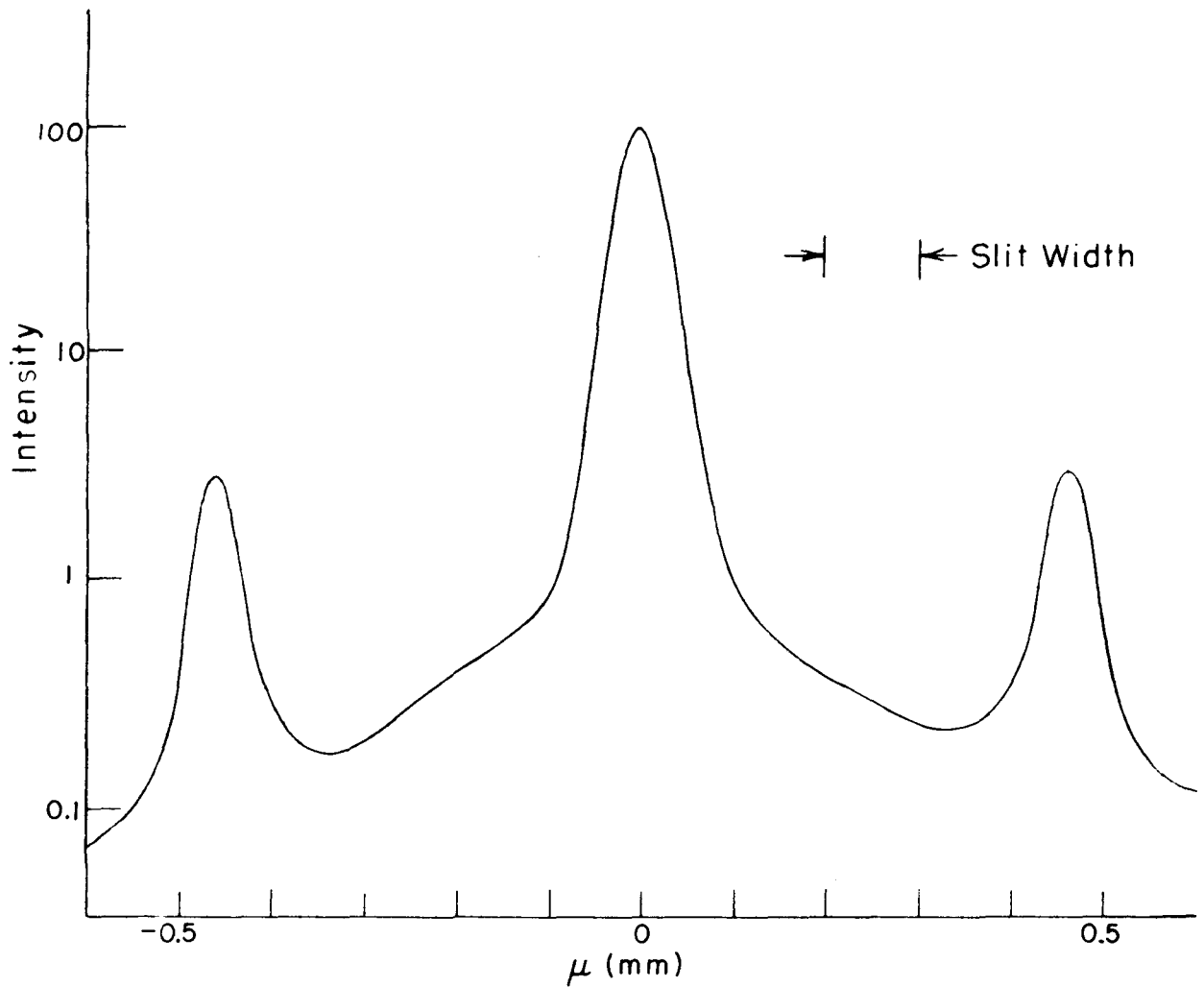


Figure A2-1. Profile of Hg4358 in the third order, with its two strongest Rowland ghosts. The ghost intensity is about 3.1% of the intensity of the principal line.  $\mu$  is the displacement along the spectrum at the exit slit.  $\Delta\lambda = D\mu$ , where  $D = \text{dispersion} = 0.94 \text{ \AA/mm}$ .

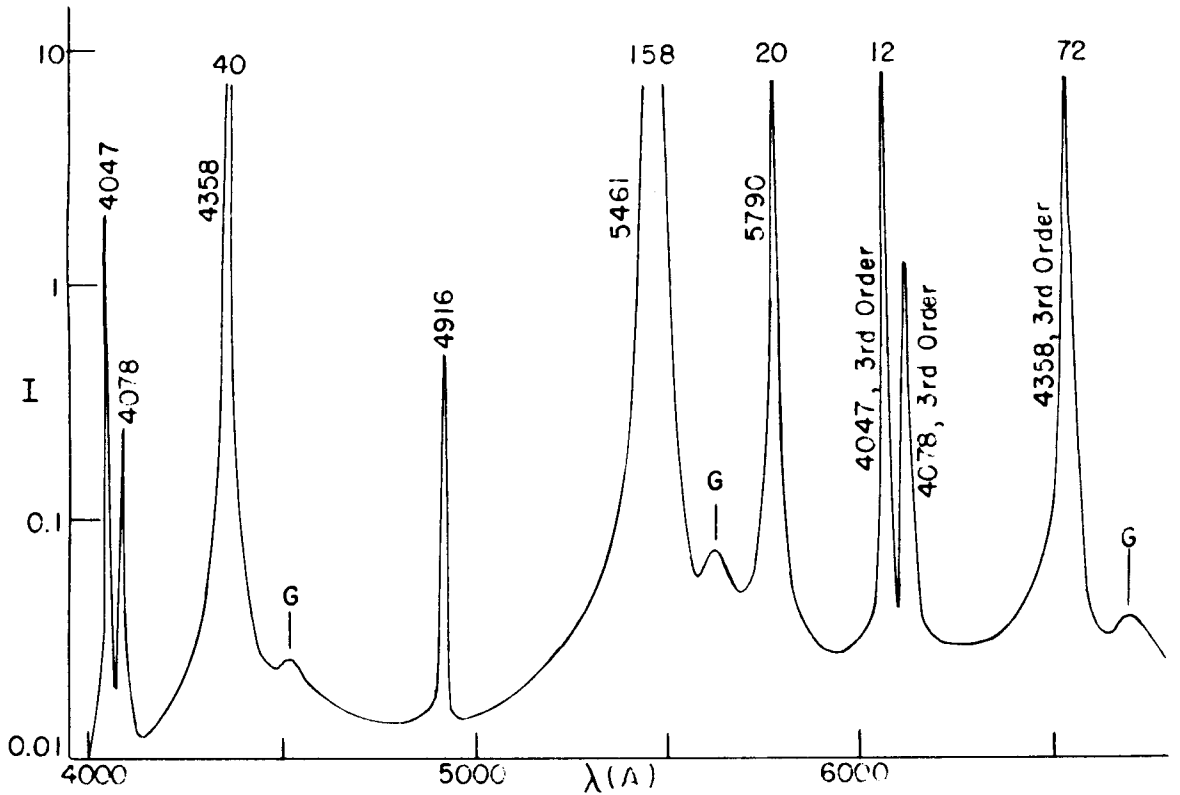


Figure A2-2. Hg spectrum as measured at the 60 ft. tower. Note the Lyman ghosts (G) about 170 Å to the red of the strongest lines.

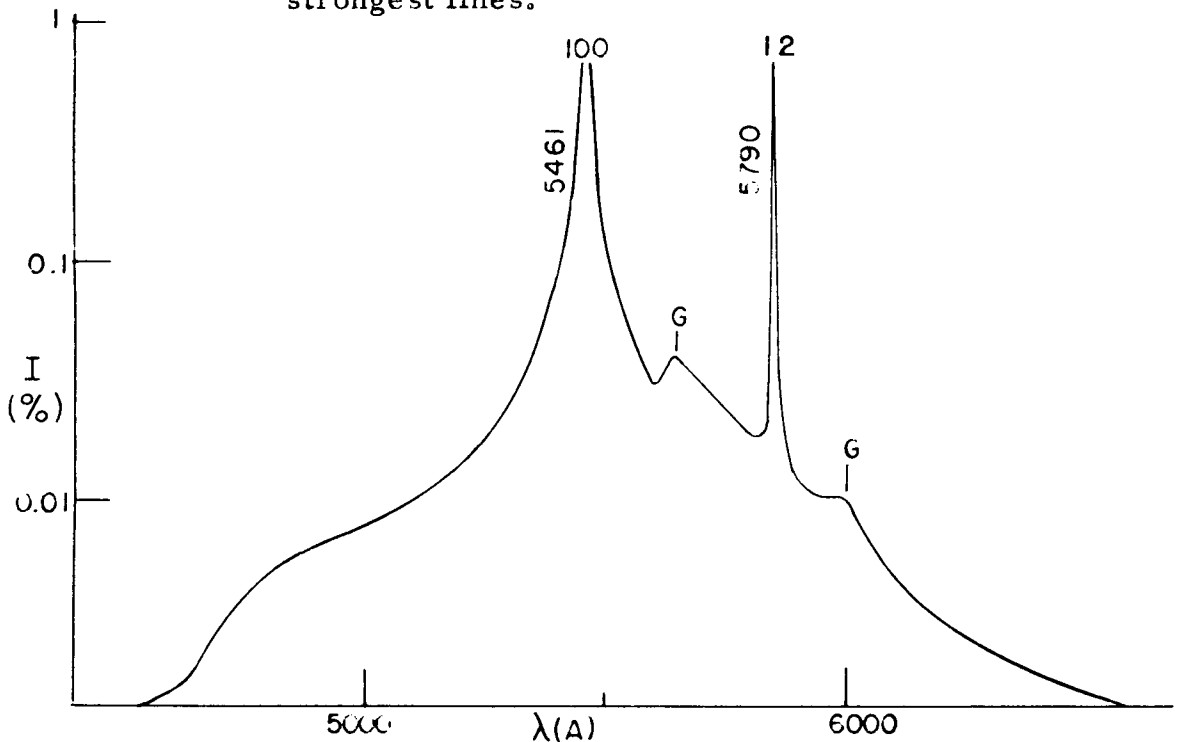


Figure A2-3. Scattered light from Hg5461, expressed as percent of the central intensity. Note ghosts (G).

the light from the  $\lambda$  5461 Hg line was isolated from the others by a filter; the ratio of scattered light to non-scattered light was found by integrating the intensity over the wavelength interval not covered by the imaged spectral line itself and comparing this with the integrated intensity of the spectral line. The ratio was found to be about 8 percent. This scattered light is exclusive of the ghosts already mentioned. If the scattering function is roughly independent of  $\lambda$ , the contribution to any wavelength of light scattered along the spectrum would be expected to be about 8 percent.

### (C) Light Scattered Perpendicular to the Spectrum

Light which is scattered perpendicular to the spectrum will be non-imaged and thus will create a rather uniform background brightness. The ratio of the light scattered to any point on the slit from all other points on the slit (except those within  $\pm 1.0$  mm of the point of interest) to the direct, non-scattered intensity, is plotted versus position on the slit in Figure A2-4. Figure A2-5 shows how the scattered intensity for a point of the center of the slit is made up of contributions from all other points on the slit. The magnitude of the light scattered perpendicular to the spectrum is surprisingly high. Since it is white light, however, it is cut down very much by the order separation filters customarily used.

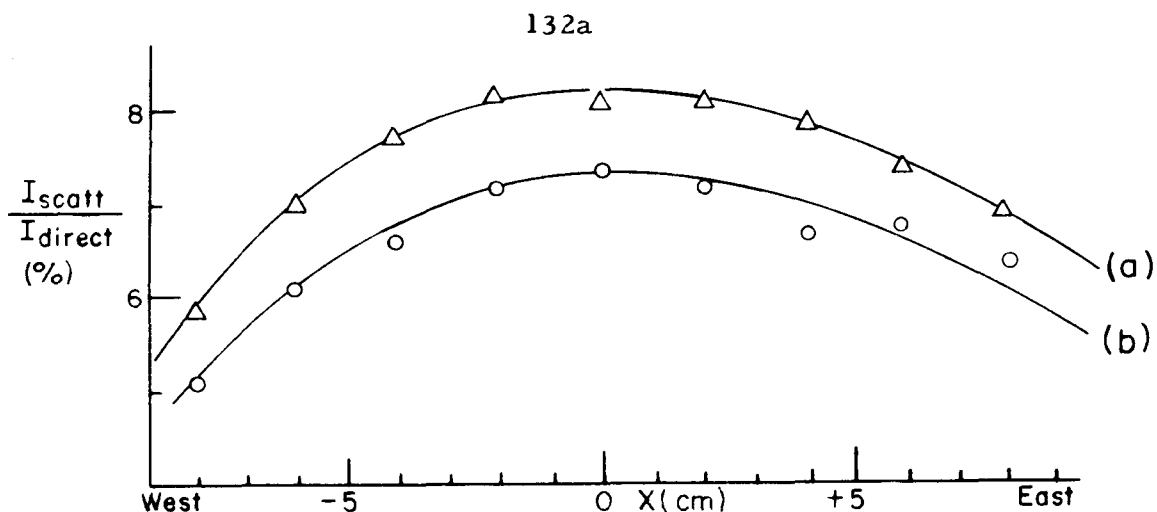


Figure A2-4. Light scattered perpendicular to the spectrum to various points on the slit. (a) unimaged sunlight on entrance slit; (b) 17 cm solar image centered at position X on slit.

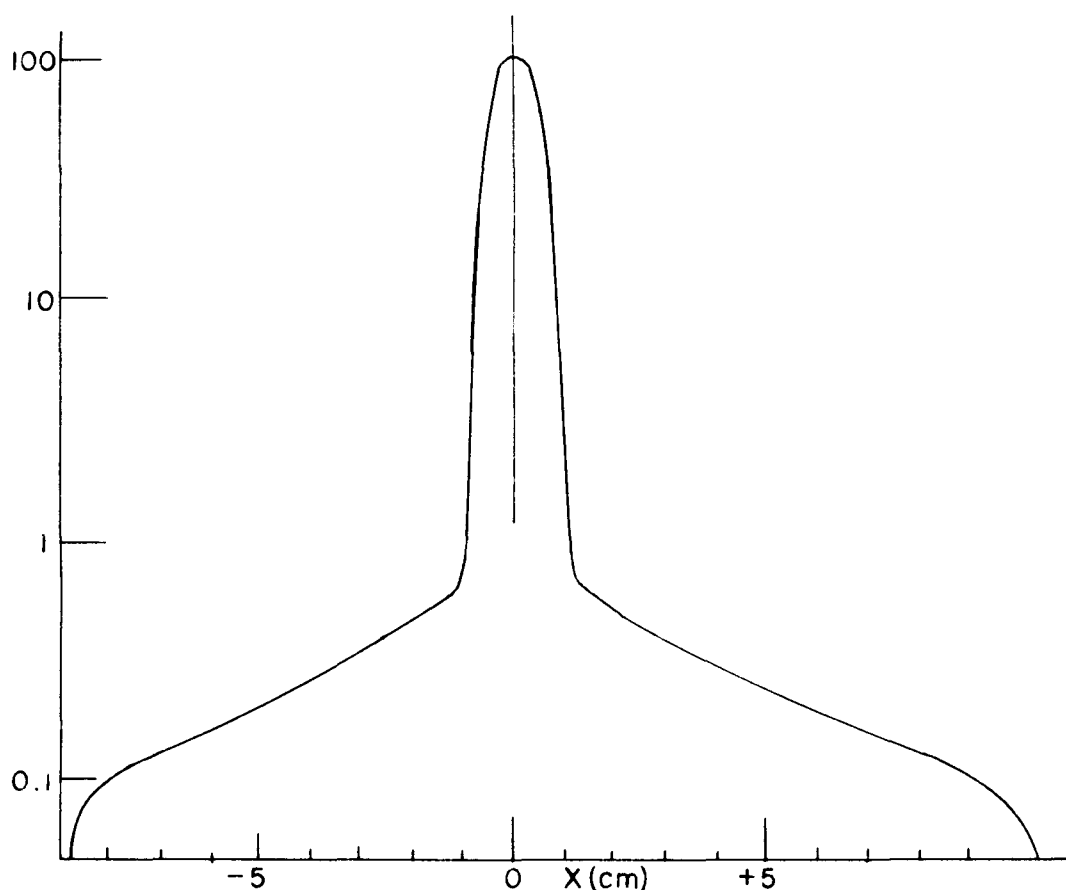


Figure A2-5. Light scattered perpendicular to the spectrum from an aperture 1.0 cm long at various positions X on the entrance slit into an aperture 1.0 cm long centered at X = 0 on the exit slit. Ordinate: Percent of direct intensity.

We conclude that the total imaged extraneous light in the second order is in the neighborhood of 11 percent, of which 3 percent is due to Rowland ghosts and the rest to scattering. Further, a component of several percent is scattered perpendicular to the spectrum. These observations are useful only for order-of-magnitude estimates; if it becomes necessary to have more quantitative information, a sodium absorption tube might be used to create an intrinsically black line at the second slit.

### APPENDIX III. ERROR ANALYSIS

In this appendix we shall first try to list all the significant sources of "error," i. e., deviations of the measured A-C and C-C functions from the "true" functions defined on p. 32. Secondly, we shall also obtain a quantitative estimate of the limits of error of the measured functions, based on measurements of several of the separate contributions to errors, on standard deviations of sets of observations of the same quantity, and on internal inconsistencies in the relation between A-C and C-C functions of original and cancelled plates.

#### (A) Sources of Error

In the following discussion we shall group the various sources of error by the stage of the observation and data reduction in which they appear.

##### 1. Errors Introduced into the Initial Spectroheliogram Pairs

- a) Imperfect telescope and spectroheliograph resolution and loss of resolution due to atmospheric turbulence

The above effects contribute to a smearing out of the small-scale details of the photographic field in all stages of cancellation; all features below a critical size, dependent on spectroheliograph settings and the seeing at the time of observation, are effectively unresolved. Therefore, one should specify a "cut-off" spatial

frequency, i. e., the observed limits of resolution. This may be only estimated by an examination of the plates for the smallest detail visible. (The best resolution yet attained, with fine seeing conditions and accurate adjustment of the spectroheliograph, is perhaps one second of arc.) In some cases in connection with this thesis, where direct comparison of heights of A-C functions from different types of observations was made, the observations were staggered in such a fashion that each type of observation immediately preceded and followed each other type, in an effort to mitigate the effects of slow changes in the seeing.

A particular hazard may be encountered when one compares A-C curves of plates taken on either half of the spectroheliograph slit, and purporting to be identical except that they were taken on opposite wings of the spectral line. In fact, there may be another difference between them which must also be considered: because corresponding points on the two images are at different distances from the center of the slit, the distance of the emulsion from the curved focal surface of the spectrograph is in general different for corresponding points on the two images. Thus at a point on one image the focus will be better than at the corresponding point of the other image (see p. 120f). Furthermore, the distance between the heights of the focal surface for corresponding points on the images varies along the slit, so the difference in quality of focus is dependent on position along the

slit. Since both the height and halfwidth of A-C and C-C functions are sensitive to changes in focus, any comparison of these quantities between plates taken on either side of a spectral line must be carefully analyzed for errors of this sort.

b) Plate grain

If no precautions are taken to minimize the effect, plate grain can contribute considerable error in the height of an A-C function, although, of course, it has no effect on C-C functions between different plates. Figure A3-1(a) illustrates the A-C function of the grain on a uniformly fogged 2-F plate of the type used for most of our observations. The plates used in the A-C machine to trace this curve were made from a fogged 2-F plate, with the grain in the sharpest possible focus. The height of the peak, 1.5 percent, is comparable to typical heights of A-C functions of original non-cancelled images, and thus could introduce significant errors. In addition, it should be noted that additional plate grain is added at each stage of the cancellation, so that the errors could thereby be compounded.

Therefore, during the projection printing of the first cancellation and of all right-left pairs, the image is very slightly defocused, just enough to wash out the grain but not destroy the detail. (From Figure A3-1(a) we see that the grain size is about 400 km on the solar image, while significant detail is usually several thousands of km in size.) Figure A3-1(b) is the same as A3-1(a), but with the grain

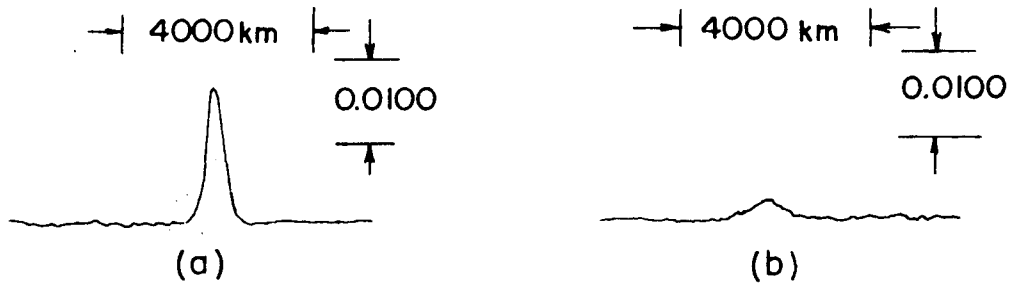


Figure A3-1. (a) Plate grain on a fogged II-F plate, in sharp focus.  
(b) Same, but slightly defocused during the printing of the right-left pair. This is the normal procedure for actual observations.

thrown out of focus in this manner. We see that if such precautions are taken, errors due to plate grain are essentially eliminated.

c) **Small-scale nonuniformities: defects in the emulsion, streaks due to dust on the slits, sunspots, etc**

The above all represent sources of error in the A-C function which can be eliminated by proper masking of the plate. (Since an A-C function is independent of the shape of the area over which it is integrated, the area is simply chosen not to include regions which contain defects.)

d) **Large-scale nonuniformities**

These include nonuniform development or drying of the plate, shadows of the compensating filter, and effects of nonuniform slit width. Generally these imperfections are on a scale many times that of the solar detail, and do not affect the shape of the central peak of the A-C or C-C function. Large-scale variations may produce a tilt in the function near the central peak, but this can be removed with the gradient-compensating filter (Fig. 2-1).

e) **Incorrect setting on the spectral line**

Imperfect setting of the second slit on the spectral line may lead to the superposition of spectroheliograms taken at different heights of line formation into a singly cancelled Doppler plate. However, the photometric techniques of setting on the line usually prevent errors in positioning of more than about 0.01 mm, i. e., 15 percent of the

slit width for 0.07 slits, so such effects are negligible in the majority of plates; therefore, by judicious selection of plates to be analysed, this source of error can be effectively eliminated.

## 2. Further Sources of Error Introduced at the First Cancellation

### a) Imperfect registration of detail on the two images being cancelled

The effect of imperfect registration is to broaden the peak of an A-C function and reduce its height in regions where the transmission fluctuations at corresponding points on the two images are positively correlated; in regions of negative correlation the (negative) height will be increased (i. e., the anti-correlation will decrease) and the peak broadened. Imperfect registration may arise from inaccuracies of alignment of the two images in the rather delicate cancellation operation; even if perfect alignment were achieved at one point in the image, other points might be out of alignment due to third order distortion in the spectroheliograph (especially the case for 1960 plates, before corrections were introduced into the curvature and tilt lenses which essentially eliminated this problem).

### b) Non-unity gamma in the photographic reduction procedure

If  $\Gamma$  for the contact print used in a Doppler cancellation is not exactly unity, a fraction of that part of the intensity field which is not due to Doppler shifts will survive the cancellation (see p. 18). If  $\Gamma = 1 + \epsilon$ , it can be shown that the transmission of the cancelled print is

$$T = T_0 (1 - 2\delta + \epsilon(\beta + \delta)), \quad (\text{A3.1})$$

through terms of first order in  $\delta$  and  $\beta$ .  $\delta$  is the (small) variation of transmission on each original plate due to Doppler shifts, and is opposite in sign on each plate;  $\beta$  is the (small) variation of transmission due to all other effects, and is the same on each plate. The height of an A-C curve of the cancelled plate described by equation A3.1 may be calculated (see p. 22) to be

$$H = 4 \langle \delta^2 \rangle + 2 \epsilon (\langle \delta^2 \rangle - \langle \beta \delta \rangle) \quad (\text{A3.2})$$

through terms of second order. Thus, if  $\langle \beta \delta \rangle$  is small (We have seen (p. 69) that for some lines  $\langle \beta \delta \rangle$  is as small as  $-0.2 \langle \delta^2 \rangle$ ) and if  $\epsilon$  is not small compared to 1, errors can result from neglecting the term in  $\epsilon$ .

The gamma of the cancellation prints is controlled by exposure and development times; and it may be checked by superposition of the contact print on its own original. The prints are redone if there is significant departure from a uniform gray field in such a superposition. The superposition of the print of the stepwedge (p. 18) on itself indicates the range over which the gamma is essentially unity. It is felt that for most of the plates reduced, the value of gamma lies between about 0.95 and 1.05, i. e.,  $|\epsilon| \lesssim 0.05$ ; however, for some of the more contrasty second cancellations (especially the Na5896 line and Ba<sup>+</sup>4554), the contrast is so great that the range of density is

exceeded over which gamma is essentially unity. In these plates, significant errors might be introduced through the above process.

### 3. Additional Errors Introduced at the Second Cancellation

When a second cancellation is made between Doppler plates taken at different times, more errors of the kind already described can enter. Non-unity gamma will have effects similar to those mentioned in the last section; in addition, as we have just mentioned in the last paragraph, it is somewhat more difficult to achieve unity gamma over the required density range in a second cancellation because of the greater contrast of Doppler plates over original spectroheliogram pairs. Finally, two new effects contribute to imperfect registration of the two Doppler plates at this stage. These are: (a) Drifts in the guider (usually caused by an increase of image brightness with a concomitant change in the guider's null position during the course of an exposure) cause the entire image to be displaced by amounts which vary with time; in addition, the guider may not be operating sensitively enough to keep the image stationary to the required accuracy during the exposure. (b) Even if the guider were to hold the west and south limbs of the sun stationary, distortions of the image from imperfect seeing would cause relative displacement of points on the disk.

#### 4. Errors in Preparing Right-Left Pairs, and in Tracing A-C and C-C Curves

The usual requirements that slight defocussing of the image occur and that  $\Gamma = 1$  hold at this final photographic stage also. In the actual tracing of curves there are three main hazards:

a) Improper registration of the images in the autocorrelation device.

The one-dimensional A-C or C-C function  $C(s)$  is essentially a "slice" out of the two-dimensional function  $C(s, t)$ , where  $t = 0$ .  $t$  is zero only if the plates come into registration at one point during the traverse; if this does not happen, the slice will miss the center of the central peak, and since the gradient of  $C(s, t)$  is generally very steep near  $(0, 0)$ , a large decrease in the height of the curve will result.

b) Improper masking of blemishes, sunspots, etc. This has already been discussed on page 137.

c) Boundary effects. The averages involved in an A-C or C-C function are meaningful only if the area of integration is essentially the same for all displacements  $s$ . This requires that the dimension of the field in the direction of the displacement be many times the maximum displacement. This is not always possible, because the maximum displacement of interest, namely that for which the two plates are uncorrelated, and which determines the normalizing function  $C(\infty)$ , may be a significant fraction of the area on the image being studied.

Further, large-scale nonuniformities, e.g., darkening at the edge of the image due to vignetting, limb darkening, or nonuniform development, contribute a spurious normalization when they enter as end effects, which is different from the normalization over most of the image. Therefore, it is often impossible to trace an A-C or C-C curve out to the point where it becomes essentially flat and where  $C(\infty)$  can be unambiguously evaluated. The normalization is then ill-defined, and it may be rather difficult to find a satisfactory scheme for normalizing all curves in the same way. The procedure most often used in cases where the normalization is ambiguous is to arbitrarily define  $C(\infty)$  to be that height where the curve intersects the ends of a baseline of predetermined length, centered at  $s = 0$ . The length of the baseline is ideally chosen to be very small compared to the length of the area integrated over in the direction of displacement, so that end effects are negligible, yet long compared to the size of detail of interest on the plate. Thus the main contribution to the peak lies above the baseline.

## 5. Calibration Errors

### a) Non-linearity of the line profile

We assume in our analysis of Doppler plates that the velocity-induced transmission fluctuations are directly proportional to the velocity. This requires both that the fluctuations be small and that no Doppler shift be over a wavelength interval greater than the linear

range of the line profile. If the slope of the expanded profile as traced on the microphotometer is constant over a range  $R$  from the position at which the slit was set, then the maximum velocity which may be observed without error is given by  $\frac{V_{\max}}{C} = \frac{R}{\lambda}$ . Using the measured line profiles to determine the maximum range  $R$  of constancy of the profile slope, we find the value of  $V_{\max}$  for the commonly used lines to be as follows:

<u>Line</u>	<u>Offset (A)</u>	<u>R(A)</u>	<u><math>V_{\max}</math> (km/sec)</u>
Fe 6102	0.10	0.04	2.0
Ca 6103	.10	.04	2.0
Na 5896	.11	.06	3.0
Ba 4554	.07	.03	2.0
Mg 5173	.11	.04	2.5
H $\alpha$ 6563	.45	.10	5.0
Ca 8542	0.23	0.12	4.2

We see from comparison of these velocities with the observational data presented in Part III that non-linearities in the profile contribute negligible errors. For Doppler shifts near the limit of the range of linearity of the profile, more serious errors would probably result from the different depths in the solar atmosphere of contribution to the intensity of the two images, due to the different offsets from the core.

#### b) Errors in measuring line profile slopes

Because a certain amount of solar intensity detail survives

the smearing by the long microphotometer aperture, the measured profile is somewhat dependent upon the part of the sun scanned by the microphotometer. In addition, the irregularities introduced into the line profile by solar spatial detail cause the slope of the recorded profile to be not perfectly defined. From experience with measuring the same profile several times, and measuring different microphotometer traces of the profile on one plate, we conclude that errors due to the above sources may sometimes be as great as 10 percent.

#### (B) Limits of Error

We shall complete this appendix by attempting a quantitative estimate of the influence of the various sources of error mentioned above. Empirical estimates have been made by the following two methods:

##### a) "Noise plates."

Doppler plates were exposed in the usual fashion, except that the slit was on the same wing of the spectral line for each of the two images. (This is accomplished by setting the line shifter to zero and displacing the slit by the required distance from the line core.) Thus, in a first cancellation, the Doppler signal, being the same on the two plates, should cancel out, leaving only "noise" due to errors in registration, non-unity gamma in the reduction process, plate grain, and development and emulsion nonuniformities. Right-left pairs were made in the usual manner, and the A-C curves traced.

In addition, a second cancellation between two such "noise" plates was made in order to bring out some of the errors involved in a Doppler sum or difference. Unfortunately, since most of the errors in the second cancellation are dependent on the contrast of the first, which is nearly zero for noise plates, this is not a very reliable method for estimating noise in second cancellations. Figure A3-2 illustrates an A-C curve for a singly cancelled Ca 6103 noise plate, and for comparison a normal singly-cancelled Ca 6103 Doppler plate. The height of the A-C curve for the noise plate corresponds to a velocity of about 0.11 km/sec. This velocity is therefore about the limit of sensitivity of the procedure. Since the height of the A-C curve of noise is about 13 percent of the height of the A-C curve of the Doppler plate, the ratio of "signal to noise" in  $\langle v^2 \rangle$  is about 8 to 1, or about 16 to 1 in  $\langle v^2 \rangle^{\frac{1}{2}}$ . Since the noise plate was reduced in precisely the fashion used for Doppler plate, the noise we have measured is a combination of that due to plate grain, errors in setting on the spectral line, imperfect registration of detail in the cancellation, non-unity gamma in the cancellation, non-constant gamma of the original plate, and A-C procedure errors.

#### b) Self-Consistency of A-C and C-C Functions

We have already indicated in Part II (p. 29 ) that there are two different ways of determining rms velocity: from an A-C function of a Doppler plate, and from the A-C functions of each original image

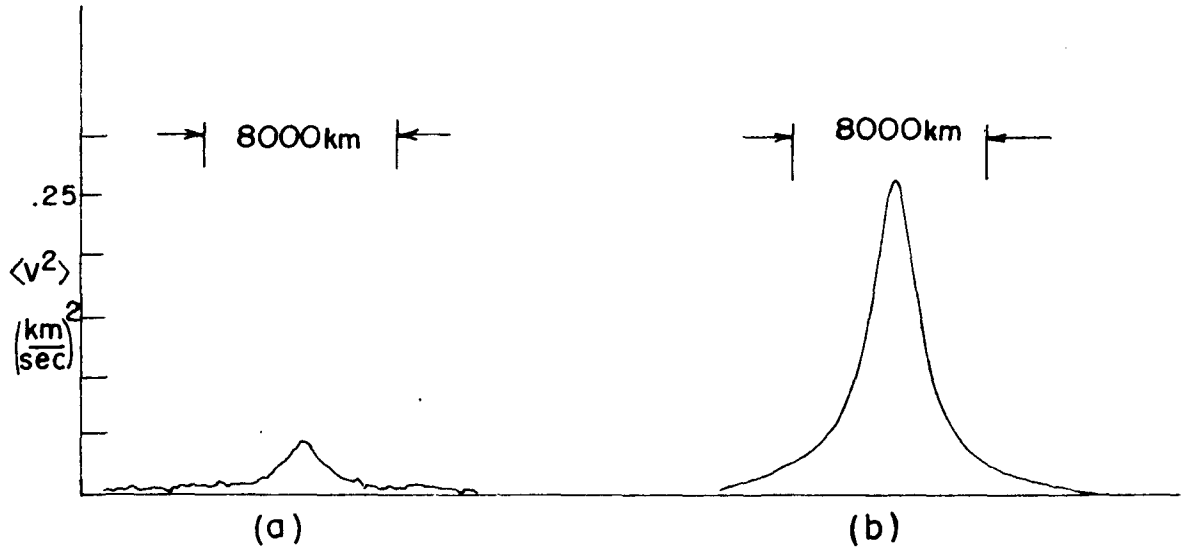


Figure A3-2. (a) A-C curve of "noise" plate for Ca6103, in which the velocity signal was suppressed by exposing both images on the same wing of the line.

(b) Normal Ca6103 Doppler plate for comparison. "Signal to noise" ratio is 8 to 1 in the A-C curve heights, or 16 to 1 in the rms velocities.

pair, in conjunction with the C-C function of the two members of the pair. The two methods should agree, if our assumptions listed on page 21 are valid. The amount of disagreement will provide us with an estimate of the errors in the reduction and A-C measurement procedures.

In order to make a quantitative self-consistency check, A-C and C-C curves were made from all possible combinations of the image from the red wing of a line, the corresponding one from the violet wing, and their Doppler cancellation. If we refer to these three images by the letters, r, v, and c, respectively, and to the heights of the A-C and C-C curves between two images i and j as  $H_{ij}$ , we may arrange these heights in a 3X3 matrix:

$$H = \begin{matrix} & \begin{matrix} H_{rr} & H_{rv} & H_{rc} \end{matrix} \\ \begin{matrix} H_{vr} & H_{vv} & H_{vc} \end{matrix} & \\ \begin{matrix} H_{cr} & H_{cv} & H_{cc} \end{matrix} & \end{matrix}$$

The diagonal members of the matrix are the A-C heights of the red, violet, and cancelled images. The off-diagonal members, which are the C-C heights, are symmetric;  $C_{rv} = C_{vr}$ , etc. Now we may write the transmission of red and violet images as

$$T_r = T_{r_0} (1 + \beta' + \delta') \text{ and} \tag{A3.3}$$

$$T_v = T_{v_0} (1 + \beta' - \delta') \tag{A3.4}$$

This is perfectly general; any two functions may be broken up into a symmetric and anti-symmetric part. (For the solar Doppler plates, we would have  $\beta' = \Gamma\beta$ ,  $\delta' = \Gamma\delta$ , where  $\beta$ ,  $\delta$ , and  $\Gamma$  are defined on page 25 .) The cancelled plate has the transmission

$$T_c = \frac{T_r}{T_v} = (1 + \beta' + \delta')(1 + \beta' - \delta'), \text{ or}$$

$$T_c = 1 + 2\beta' + 2\delta'^2 - 2\beta'\delta' + O(\beta'^3, \delta'^3) \quad (\text{A3.5})$$

From equations A3.3, A3.4, and A3.5, we find, keeping terms through the second order in  $\beta'$  and  $\delta'$  and labelling r, v, c, as 1, 2, 3,

$$\begin{aligned} H_{11} &= \langle (\beta' + \delta')^2 \rangle & H_{12} &= \langle \beta'^2 - \delta'^2 \rangle & H_{13} &= 2[\langle \beta'\delta' \rangle + \langle \delta'^2 \rangle] \\ H_{21} &= H_{12} & H_{22} &= \langle (\beta' - \delta')^2 \rangle & H_{23} &= 2[\langle \beta'\delta' \rangle - \langle \delta'^2 \rangle] \\ H_{31} &= H_{13} & H_{32} &= H_{23} & H_{33} &= 4 \langle \delta'^2 \rangle \end{aligned}$$

We see that the third row of the matrix is the difference between the first two rows. Also,

$$H_{33} = H_{11} + H_{22} - 2H_{12} = 4 \langle \delta'^2 \rangle . \quad (\text{A3.6})$$

Measured values of the matrix H, listed in percent, for various spectral lines, are as follows:

a)	Fe 6102, 6-14-61	b)	Ca 6103, 6-17-61
	1.86 0.64 0.82		3.63 0.33 2.47
	0.64 1.35 -0.41		0.33 1.58 -1.04
	0.82 -0.41 1.30		2.47 -1.04 3.20

c)	Ba <sup>+</sup> 4554, 7-1-61	d)	Na 5896, 8-1-61
	5.65 -0.53 5.15		2.77 -1.55 -
	-0.53 3.05 -3.40		-1.55 4.74 -
	5.15 -3.40 7.35		- - 12.75

Examination of the values listed above reveals that they do not satisfy the self-consistency requirements just discussed. If the A-C values  $H_{11}$ ,  $H_{22}$ , and  $H_{33}$  are taken to be correct, then the measured C-C curve heights are in general too low by from 10 percent to 50 percent. This could be due to the presence of residual noise, uncorrelated on the red and violet images, and therefore not contributing to  $H_{12}$ , but contributing to the A-C functions. Alternatively, the values  $H_{11}$ ,  $H_{12}$ , and  $H_{22}$  might be correct, in which case  $H_{33}$  is usually 10 percent to 40 percent too high. We note that the uncertainties appear to be systematic, i. e., there is a trend toward the same type of inconsistencies on the different sets of plates.

From this study we conclude that the reduction and measurement process may introduce systematic errors of perhaps as much as 20 percent in the root mean square velocities (40 percent in A-C function heights).

The numbers just quoted, along with our previous estimates of 10 percent uncertainty due to calibration errors and perhaps 10 percent uncertainty due to cancellation noise, imply that the final value for the velocities may be uncertain by as much as 30 to 40 percent.

This is actually somewhat larger than the spread of observed values for velocity in the same line from different plates, which is usually less than about 25 percent.

Therefore, we conclude this appendix by adopting 30 to 40 percent as a rather conservative estimate of the "limits of error" of the velocity measured on a Doppler plate.

## REFERENCES

1. Leighton, R. B., Astrophys. J., 130, 366-380 (1959).
2. Leighton, R. B., Noyes, R. W., and Simon, G. W.,  
Astrophys. J., 135, 474-499 (1962).
3. Blackman, R. B., and Tukey, J. W., The Measurement of Power Spectra, 7 (New York: Dover Publications, Inc., 1959).
4. Unno, W., Astrophys. J., 129, 375-400 (1959).
5. Jager, C. de, Hdbch. d. Physik., vol. 52, 97, 105 (Berlin, Springer Verlag, 1959).
6. Evans, J. W., and Michard, R., Astrophys. J., 135, 812-821 (1962).
7. Allen, C. W., Astrophysical Quantities, 133 (Univ. of London Athlone Press, 1955).
8. Evans, J. S., and Michard, R., Astrophys. J. (Paper III, in press).
9. Parratt, L. G., Probability and Experimental Errors in Science, 118 (New York, Wiley, 1961).
10. Jager, C. de, op. cit., 125.
11. Bahng, J., and Schwarzschild, M., Astrophys. J., 134, 312-322 (1961).
12. Osterbrook, D. E., Astrophys. J., 134, 347-388 (1961).
13. Unsold, A., Zeitschrift für Astrophysik, 50, 57-68 (1960).
14. Biermann, L., Naturwissenschaften, 33, 118-119 (1946).
15. Schwarzschild, M., Astrophys. J., 107, 1-5 (1948).

16. Laplace, P. S., Mecanique Celeste, vol. 4, Chap. 5 (1845).
17. Rayleigh, Lord, Phil. Mag., 29, 173 (1890).
18. Lamb, H., Hydrodynamics, 541-545 (New York, Dover, 1945).
19. Pekeris, C. L., Phys. Rev., 73, 145-154 (1948).
20. Donn, W. L., and Ewing, M., J. Geophys. Res., 67, 1855-1866 (1962).
21. Schatzmann, E., Annales d'astrophysique, 12, 203-218 (1949).
22. Whitney, C., Smiths. Contr. of Astrophys., 2, 365-376 (1958).
23. Jager, C. de, and Kuperus, M., B.A.N., 16, 71-82 (1961).
24. Evans, J. W., Main, P., Michard, R., and Servajean, R., private communication (to be published).
25. Howard, R., Astrophys. J., in press.
26. Deubner, F. L., private communication (1962).
27. Erdelyi, Ed., Tables of Integral Transforms, vol. I, 26 (McGraw Hill, 1954).
28. Kuiper, G.P., ed., The Sun, 127 (Univ. of Chicago Press, 1953).
29. Spiegel, E. A., Astrophys. J., 126, 202-207 (1957).
30. Krasberg, A., and Whitney, C., Smithsonian Astrophysical Observatory (in press).
31. Stuart, F. E., and Rush, J. H., Astrophys. J., 120, 245-250 (1954).
32. Plaskett, H. H., Mon. Not. Roy. Ast. Soc., 114, 251-270 (1954).